The Pennsylvania State University

The Graduate School

Department of Electrical Engineering

INVESTIGATION OF AEROSOL AND CLOUD PROPERTIES USING MULTIWAVELENGTH RAMAN LIDAR MEASUREMENTS

A Thesis in

Electrical Engineering

by

Sachin John Verghese

Submitted in Partial Fulfillment
of the Requirements
for the Degree of

Doctor of Philosophy

April 2008

The thesis of Sachin John Verghese was reviewed and approved* by the following:

C. Russell Philbrick
Professor of Electrical Engineering
Thesis Advisor
Chair of Committee

Zhiwen Liu
Associate Professor of Electrical Engineering

Ruyan Guo
Professor of Electrical Engineering

Dennis Lamb
Professor of Meteorology

Richard Clark
Professor of Meteorology
Special Member
Millersville University
Millersville, PA

W. Kenneth Jenkins
Professor of Electrical Engineering
Head of the Department of Electrical Engineering

*Signatures are on file in the Graduate School

ABSTRACT

Lidar measurements obtained during several field campaigns have provided an extensive dataset for investigating aerosol characteristics and cloud properties. In this thesis we use measurements of multi-wavelength optical extinction measured with a Raman lidar to infer aerosol and cloud particle size variations. Aerosol extinction depends on both size and number density of the scatterers. The optical extinction at different wavelengths depends on the sixth power of the size parameter for aerosols much smaller than the scattering wavelength, and on the second power of the size parameter for aerosols much larger than the wavelength. Changes in the density of a particular size aerosol lead to a proportional response. The extinction profiles at several wavelengths are simultaneously examined to study changes in the aerosol size distribution over an interesting range of sizes corresponding to accumulation-mode particles. Model calculations based on Mie scattering theory are compared with extinction profiles at different wavelengths, water vapor profiles, and other simultaneous measurements, to investigate the formation and dissipation of cloud structures. The optical scattering measurements from aerosols and cloud particles demonstrate that various characteristics of aerosols and visibility can be determined.

We demonstrate the capability of the new technique using the multi-wavelength extinction ratios to profile information about changes in CCN particle size in the range of 50 nm to 0.5 μm. Examples taken from three different field campaigns demonstrate that changes in the size of the cloud particles during the different stages of growth and dissipation are observed in the multi-wavelength aerosol extinction using this technique. We also show the relationship that exists between particle size increase or decrease in cloud regions, based on the extinction coefficients and changes in relative humidity.

The deliquescence relative humidity (DRH) is found to exert a strong control on the optical extinction and visibility. Our results show that relative humidity values above 85% accompany drastic drops in visibility in the U.S. north-east regions. Increase in the relative humidity values beyond the DRH results in rapid growth of particle size, which in turn causes a simultaneous increase in the optical extinction and a drop in visibility.

Comparison of data from the eastern and western regions of the United States show that different sources control the changes in optical extinction values in the lower boundary layer. During the Southern California Ozone Study (SCOS) campaign an increase of optical extinction was observed after sunset in the nocturnal boundary layer due to the growth of particles caused by the increasing relative humidity. On the other hand, the optical extinction during the North-East Particle and Oxidant Study (NEOPS) campaigns was controlled more by pollutant concentrations and showed an increase in values after sunrise and decreased values after sunset; opposite from that observed at Hesperia, Ca.

We used theoretical simulations along with field measurements of multi-wavelength extinction coefficients to investigate the differences that particle growth and pollutant concentration have on the extinction coefficient as well as on the extinction coefficient ratios (visible/ultraviolet). Our results show that the increase in the extinction coefficient in a region of pollutants, typically composed of smaller size particles, depends on the number density of the scatterers, which has the same effect at all wavelengths.

We additionally demonstrate the capability of the Raman lidar to measure atmospheric visibility conditions and transmission properties using the optical extinction measurements.

TABLE OF CONTENTS

LIST OF FIGURES

LIST OF TABLES

ACKNOWLEDGEMENTS

I would like to thank all those who contributed to this work. Primarily, sincere appreciation is extended to my thesis advisor, Dr. C. R. Philbrick, for his professional guidance and patience. I would also like to thank him for giving me the opportunity to work in his lab and for teaching me valuable lessons in research and in life. I would not have been able to complete this work without his constant support and encouragement.

I would like to thank my committee members, Dr. Dennis Lamb, Dr. Richard Clark, Dr. Ruyan Guo, and Dr. Zhiwen Liu for supporting my effort and for their valuable feedback.

Thanks are due to Adam Willitsford, Dave Brown and Jin Park for their encouragement and friendship.

I would also like to thank my parents and wife because I would not have achieved all that I have without their constant support, encouragement, and love.

I acknowledge the support of my graduate research by the United States Environmental Protection Agency, grant # R826373, by the Pennsylvania Department of Environmental Protection, and by the City of Philadelphia Air Management Services Laboratory.

This study would not have been possible without the dedicated efforts of many individuals. The data used in this thesis was available due to the hard work of many students and research scientists. Special appreciation goes out to all the engineers and technicians at the PSU Applied Research Laboratory and the graduate students of the Department of Electrical Engineering who made this work possible. Special thanks also goes out to the students and research scientists from other universities and research labs who took part during the different campaigns.

I would like to thank C. Russell Philbrick, D.B. Lysak, T.M. Petach, F. Balsiger, T.D. Stevens, P.A.T. Haris, M. O’Brien, and Savy Mathur for their outstanding work during the USNS SUMNER campaign in 1996.

I would like to thank C. Russell Philbrick, D.B. Lysak, T.M. Petach, T.D. Stevens, P.A.T. Haris, M. O’Brien, S.T. Esposito, and H. Li for their outstanding work during the Southern California Ozone Study (SCOS) in 1997.

I would like to thank C. Russell Philbrick, D.B. Lysak, T.M. Petach, S.T. Esposito, Karoline R. Mulik, and Mike Zugger for their outstanding work during the Atmospheric Radiation Measurements (ARM) Program in 1998.

I would like to thank all the students, research scientists, and investigators from all the universities and research labs who took part during the NARSTO-NEOPS and the NEOPS-DEP program. A list of all the participants during the NEOPS campaigns is provided in Appendix D. Special thanks goes to C. Russell Philbrick and the students of PSU, Steven Esposito, Karoline Mulik, Ginnipal Chadha, Alex Achey, Corey Slick, Ed Novitsky, Gregg O’Marr, Sriram Kizhakkemadam, and Guangkun Li for their dedicated efforts during the NARSTO-NEOPS campaigns. Special thanks also go to C. Russell Philbrick

and the students of PSU, Jason Collier, Adam Willitsford, Sameer Unni, and Mike Wyland for their dedicated efforts during the NEOPS-DEP campaigns.

Chapter 1
Introduction

1.1 Introduction

Over the past few decades, the scientific challenges to develop better techniques to monitor and model our atmosphere have gained increased priority due to the growing number of questions concerning our changing environment and its impact on human life. Perhaps the greatest stimulus to the current general interest in global climate research stems from the increasing temperature, inter-annual climate variability, and global warming issues [*IPCC, 2007*]. In order to minimize the consequences, it is imperative that we study the atmosphere not only to understand the structure and processes within it, but also to evaluate the effects of man's activity on it. To study and understand the large number of feedback processes that are changing our atmosphere, we require development of simulations using sophisticated numerical models, along with detailed investigations of processes on a small scale and global observations of key parameters.

Aerosols play vital roles in cloud formation that act to balance the Earth's radiation budget. Aerosols limit optical propagation, incoming solar radiation, and impact human health because they provide a way of concentrating the chemical species resulting from air pollution in the lungs. Recent assessments conclude that the largest uncertainties in the impact of human activity on global mean radiative forcing are due to the lack of understanding of how pollution influences cloud patterns and the attributes of individual clouds [*Houghton et al., 2001*]. Cloud droplet number concentrations rise with increasing aerosol loading [*Pueschel et al., 1986*], but neither the specific microphysical processes that control this behavior nor its implications are well understood. The aerosol contributions, both positive and negative, result in the largest uncertainty in calculation of the energy budget of the Earth's atmosphere [*IPCC, 2001*].

Atmospheric aerosols are generated from various natural and anthropogenic sources and include all liquid and solid particles, except pure water, that exist in the atmosphere under normal conditions [*Arya, 1999*]. The largest anthropogenic increases in aerosol concentrations are due to the direct emission of elemental carbon and organic aerosol from incomplete combustion of carbonaceous fuels, and the nucleation of primary emissions of sulfate, ammonia, nitrate, and condensable organic species from industrial activities, power generation, transportation, biomass burning, and fertilizers [*IPCC, 2001*].

The distribution of aerosols in the atmosphere influences Earth's climate because of scattering and absorption of radiation by particles. Aerosols and clouds play a major role in determining what fraction of the solar radiation incident at the top of the atmosphere reaches the Earth's surface and also influences the transfer of infrared radiation back to space. The propagation of shortwave and longwave electromagnetic radiation through the atmosphere is strongly influenced by the presence of aerosol and cloud layers and hence a detailed understanding of these layers has become important. Aerosols assert a *direct effect* by absorbing and scattering radiation. They also assert an *indirect effect* by influencing the formation, microphysical properties, and lifetime of cloud structures. The potential alteration of cloud behavior due to increasing levels of particulate pollution has vast and complex implications for the global climate. Two primary cloud-altering indirect effects of aerosols on climate have been observed: clouds that form in polluted environments are optically thicker and reflect more sunlight back to space before it can warm the lower atmosphere and surface; and clouds that form in polluted environments are less likely to precipitate, which increases the lifetime of individual clouds and shifts rainfall patterns [*Menon, 2004*]. The increased lifetime of clouds is due to the fact that the larger numbers of activated aerosols compete for the available water thus limiting their size and delaying their growth, thereby inhibiting the initiation of the collision-coalescence process. The indirect effect, resulting from changes to cloud albedo, microphysical properties, and increased lifetimes, is not yet fully understood, but is thought to exert a negative radiative forcing on the climate system [*Twomey, 1977; Albrecht, 1989; Wielicki, 1995*]. The fundamental concern for models that try to capture the indirect effects of aerosols is the relationship between sub-cloud aerosol populations and the processes of cloud droplet formation upon them. The detailed representation of clouds in general circulation models has thus become a major problem for scientists as it is obviously impossible to simulate and predict Earth's climate accurately without such knowledge.

Increases in the concentrations of tropospheric aerosols have also been seen to be directly related to a myriad of health problems [*Hidy et al., 1998*]. Particles having a diameter less than 2.5 microns, referred to as $PM_{2.5}$, are considered to be of greater risk to human health because of the deep penetration of small particles into the lungs, and due to the large number of these particles generated in the emission from combustion products that carry carcinogenic materials. Also, the propagation of light through the atmosphere is strongly affected by the presence of aerosols, which reduces the visual range, degrades the performance of electro-optic sensors, and lowers the aesthetic beauty of the outdoors. In order to understand the effects of aerosols, current research efforts are focused on identifying and predicting production and transport mechanisms, as well as ascertaining number densities and composition.

A significant challenge is faced in accurately measuring the various formation processes of atmospheric aerosols because of the influence of various minor species on the growth rate, hygroscopic properties, and nucleation processes. In-situ methods of atmospheric sensing, such as those using aircraft and balloons, require constant human involvement, can only operate for several hours at a time, are expensive to maintain, and frequently need to be replaced. Satellite remote sensing provides an important platform for describing large-scale features distributed over global scales, but these systems are extremely expensive, and are too limited in vertical and temporal resolution to study the processes governing aerosol formation. Ground-based lidar techniques have been used to measure aerosol optical parameters and offer several advantages over other measurement techniques. Lidar instruments have the ability to provide good spatial resolution and high temporal resolution at a specific location. Lidar determination of aerosol size distributions and other properties have been investigated by several research groups, but results have been mostly limited to theory and simulations. Experimental data to demonstrate the retrieval of size distributions are limited because of the difficulty in analyzing data using inversion techniques, and the range of wavelengths needed to perform an adequate inversion analysis [*Gillespie et al., 2002*]. Advanced techniques using multi-wavelength lidars have become extremely important because they provide a key to overcoming these data analysis difficulties [*Philbrick et al., 2001; Mattis et al., 2004; Ansmann et al., 2005; Novitsky et al., 2005*].

For this investigation, the measurements obtained by the PSU Lidar Atmospheric Profile Sensor (LAPS) Raman lidar, over the past decade, provided an extensive dataset to characterize cloud properties and aerosol distributions. The LAPS system measures the profiles of molecular nitrogen, molecular oxygen, water vapor, temperature and optical extinction at both visible and ultraviolet wavelengths. These measurements are then used to determine density profiles of water vapor and ozone, and to generate vertical aerosol extinction profiles from the measured incremental extinction. Since the optical extinction at different wavelengths is strongly dependent on the size distribution of aerosols, the differences in extinction profiles for separated wavelengths is used to infer changes in the aerosol size distribution over the range corresponding to accumulation-mode particles, 50 nm to 500 nm. Model simulations are used along with the field data to interpret and understand the various relationships that exist.

1.2 Goals and Thesis Outline

This research effort is focused on investigating properties of aerosol and cloud particles in the lower atmosphere using the extensive dataset obtained with PSU's Raman lidar. The data were collected during several campaigns in different regions and provide a comprehensive database of field measurements for this and for future studies.

The primary objective of my study is to infer particle size variations using the optical extinction measurements obtained at three different wavelengths measured by the LAPS Raman lidar. The ratio of the extinction at the different wavelengths contains important information regarding the size variation of particles in the range of sizes referred to as the accumulation-mode. We use the multi-wavelength extinction ratios, along with calculations that simulate the extinction ratios using Mie theory to investigate particle size variations in this important range. Accumulation-mode particles are particularly interesting as they correspond to the size range for cloud condensation nuclei and because they effectively scatter solar radiation [*Ramanathan et al, 2001*]. Our laser employs radiation of wavelengths in the visible and ultraviolet and so provides signals that contain information on changes in the relative size for particles sizes corresponding to those wavelengths. The analysis is also used with the water vapor, temperature, and relative humidity values measured simultaneously by the Raman lidar to study the growth and dissipation of cloud structures.

The second major objective was to examine the particle size variations in air pollution plumes and in cloud structures using data from the Raman lidar, and from other instruments obtained during the several campaigns. The variations in extinction coefficients within the boundary layer are compared between the eastern (NEOPS campaigns) and western United States (SCOS campaign) both during the daytime and nighttime.

A third major objective was to use the optical extinction measurements made using the Raman Lidar to describe the visibility and transmission properties of the atmosphere. The Raman lidar aerosol extinction provides us with the capability to determine the visual range along a path through the atmosphere because our ability to see distant objects depends on the integrated aerosol density and particle size along the path.

This thesis is organized into sections that provide the reader with a general overview of the background on aerosols and how they affect the energy budget, and on the optical scattering processes used to obtain measurements and in model calculations. I then introduce the instrumentation before showing the results. Chapter 2 provides a brief introduction on aerosols, clouds, and an overview of scattering from molecules and particles. Chapter 3 describes the LAPS instrument and the data processing and analysis aspects of the Raman Lidar. The work presented in this thesis is based on data obtained during several campaigns, and Chapter 3 provides a brief introduction to each campaign.

The results and analysis are presented in Chapter 4. Chapter 5 summarizes my conclusions and provides suggestions for future work.

Chapter 2

Background: Aerosols, Clouds and Scattering

2.1 Aerosols

Atmospheric aerosols are the tiny liquid and solid particles that are suspended in our atmosphere. They are generated from various natural, industrial, mechanical, and combustion sources. They have size ranges that span over four orders of magnitude. The variety of particles found in air and their typical size ranges are shown in Figure 2-1. Aerosols found in the atmosphere include tiny grains of mineral dust stirred up from the ground, salt particles from the evaporation of sea spray droplets, bacteria, pollen grains, mold spores, photo-chemically produced droplets of sulfuric and nitric acid and other pollutants, soot particles produced in fires and vehicle exhaust, and many other materials.

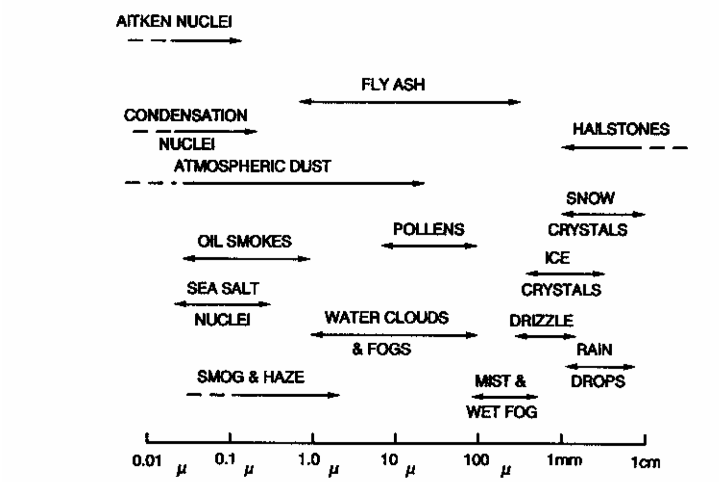

Figure 2-1: Variety of particles found in the atmosphere, and their corresponding size range [*Johnson, 1969*].

Many aerosols occur naturally, but the total amount of aerosols has been seen to increase from direct particulate emissions and from chemical reactions involving gaseous precursors. This increase in their population is important, as they play a critical role in determining the optical properties of our environment and consequently the global energy budget. Figure 2-2 shows some of the typical aerosol generation and removal processes in our atmosphere.

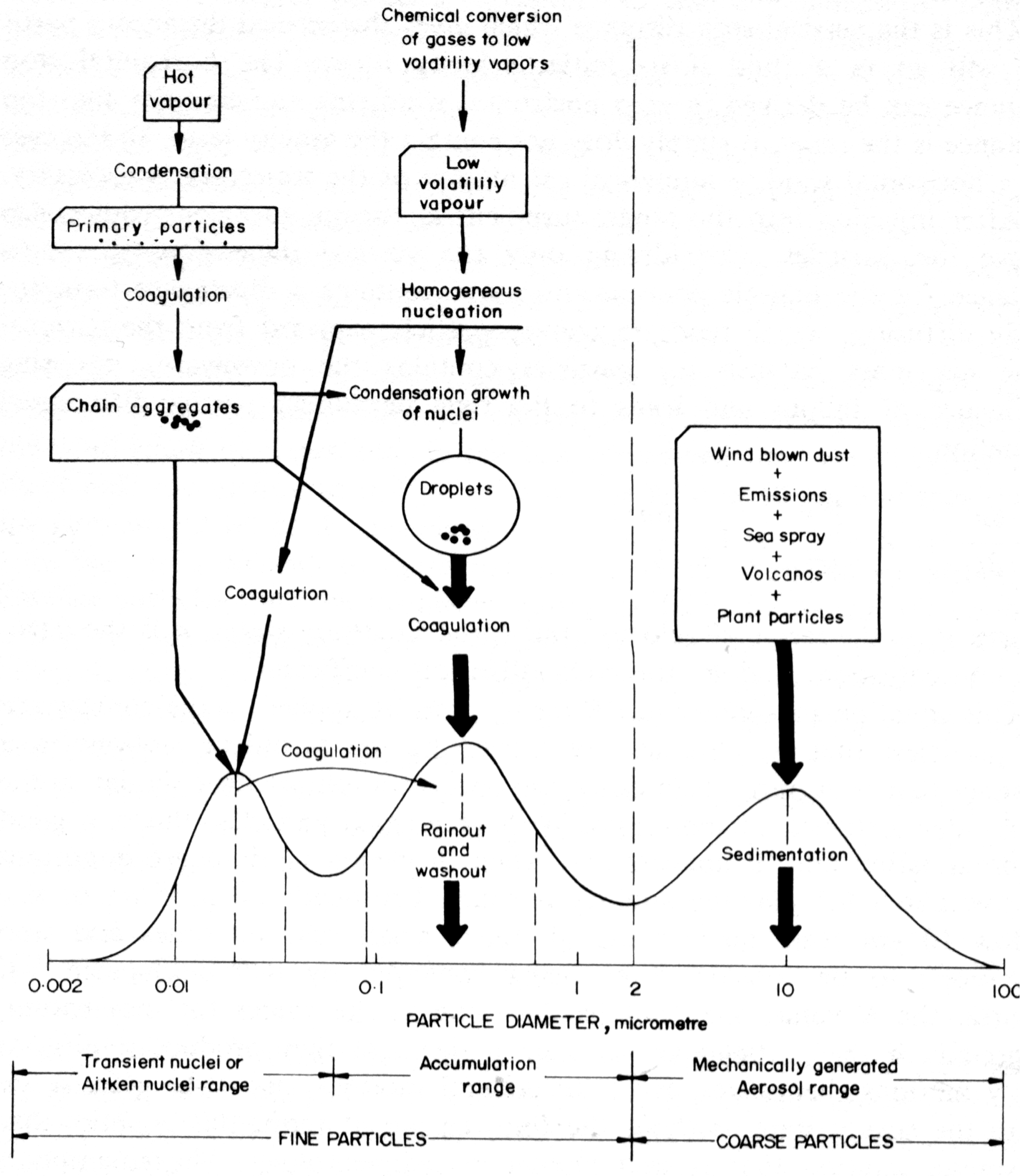

Figure 2-2: Aerosol generation and removal processes in our atmosphere [*Whitby, 1975*]

Airborne particulate matter is typically approximated by three log-normal modes, which are used to classify the characteristics of particles based on their size: nucleation mode, accumulation mode, and coarse mode. The largest number of particles by far, referred to as fine particles, are found at smaller sizes in the nucleation and accumulation mode. The smallest aerosols are the Aitken nuclei, which range from the size of large molecules to particles of size about 0.1 μm. Cloud condensation nuclei (CCN) are also very small and they range in size up to about 1.0 μm. These smaller size aerosols are important for several reasons, one being that they serve as seeds for cloud formation and as nuclei on which atmospheric gases can condense and grow to larger aerosols [*Kyle, 1991*]. Particles having a diameter less that 2.5 microns, referred to as $PM_{2.5}$, are considered to be of greater risk to human health because a large number of these particles are associated with the emissions from combustion products and carry carcinogenic chemicals; these smaller particles are inhaled more deeply into the lungs. Table 2-1 provides an overview of the size range of aerosol particles found in our atmosphere.

Aerosols play an important role in climate change, stratospheric ozone depletion, and air quality issues. Three types of aerosols have been found to have a significant influence on the Earth’s climate. They are volcanic, desert, and man-made aerosols, and these are classified based on their generation source. Those volcanic aerosols with significant atmospheric lifetime are the smaller particles resulting from volcanic eruptions and may result in ejections as high as the stratosphere. Erupting volcanoes introduce large quantities of solid and gaseous materials into the atmosphere with large particles that settle out quickly. The smallest volcanic aerosols are formed when sulfur dioxide gas is converted to droplets of sulfuric acid in the stratosphere over the course of days to several months following an eruption. They may have lifetimes as long as two years and spread over much of the globe [*Salby, 1996*]. They tend to cool the Earth’s surface by reflecting sunlight. Volcanic aerosols generally increase the global albedo and cool the troposphere, but they have been associated with a winter warming pattern of surface air temperature over Northern Hemisphere continents [*Kirchner et al., 1999]*. The relative coolness of 1993 is explained as a response to the stratospheric aerosol layer that was produced by the Mt. Pinatubo eruption [*Stenchikov et al., 1998]*.

Table 2-1: Summary of typical dimensions and description of various constituents of the atmosphere.

		Dimensions	
Fine Particles	**Aitken Nuclei**	0.1 nm	Typical dimension of small molecules or atom.
		1 nm	Smallest particle sizes detected by cloud condensation nuclei techniques.
		10 nm	Stable and permanent size with reasonable storage times, coagulation at atmospheric concentrations is not excessively fast.
	Accumulation Mode	100 nm	Considered to be large atmospheric aerosols. Particles of this size have the longest survival, as diffusive and inertial coagulative processes are inefficient.
		1 µm	Larger end of the cloud condensation nuclei. Have falling speeds, under gravity, of about 0.0003 m/s.
Coarse Particles		10 µm	Size of cloud droplets. Particles can be observed with the naked eye on suitable surfaces. Fall speed of about 0.03 m/s.
		100 µm	Size of fine drizzle drops. Produced by sea spray, but fall out quickly. Fall speeds about 0.27 m/s.
		1 mm	Typical size of raindrops.
		1 cm	Hail, graupel and snow produced in the atmosphere attain this size.

The second type of aerosol that has a significant effect on climate is desert dust. One of the largest sources of aerosols is dust picked up from desert surfaces. The surface materials picked up by the wind include organic materials, silicon and geological materials, which absorb as well as scatter sunlight. Dust particles warm the layer of the atmosphere by direct absorption of sunlight incident in regions of the atmosphere where they reside. However, these aerosols also cool the Earth’s surface by reflecting a portion of the incoming radiation back to space. The two major sources of desert dust aerosols are the Sahara desert of Africa and the Gobi desert of Asia.

The third type of aerosol, and the source of most concern, comes from human activities. While a significant fraction of human-made aerosols result from smoke from burning tropical forests, the major component comes in the form of sulfate aerosols created by the burning of coal and oil. Industrial activities such as electrical power plants, oil refineries and factories contribute heavily to the aerosol content in the atmosphere. The largest anthropogenic increases in aerosol concentrations are due to the direct emission of elemental carbon and organic aerosol from incomplete combustion of carbonaceous fuels, and the nucleation of primary emissions of ammonia, nitrate, sulfate, and condensable organic species from power generation plants, industrial activity, transportation, biomass burning, and land cultivation [*Arya, 1999*]. The mechanical activities also act in repopulating the atmosphere with the previously settled aerosols, resulting in a new population of coarse and fine particles.

Aerosols evolve following their initial formation, and observations reveal that aerosol populations are frequently inhomogeneous mixtures of a complex multi-component population. Typical aerosol concentrations are found to be smallest over oceans (10^3 cm^{-3}), and greatest over industrial areas (10^5 cm^{-3}) [*Salby, 1996*]. The anthropogenic component of sulfate exceeds 60% of the total sulfate production over urban areas, and it plays a key role in cloud formation [*Menon, 2001*]. The sulfate aerosols influence the climatic cycle as they reduce the amount of sunlight reaching the Earth's surface due to increases in the planetary albedo. Since the sulfate aerosols are relatively small, they have long residence times in the atmosphere and can act as nucleation centers for the formation of cloud particles [*Menon et al., 2002*]. The fact that sulfate aerosols are hygroscopic means that their size can grow rapidly in high humidity regions, such as the U.S. east coast. Their increased size results in the increase of optical extinction as the population of these larger aerosols increases. This process can both act to enhance or retard the formation of cloud particles, depending on the other simultaneously acting atmospheric processes. The net effect results in cloud particles reflecting more sunlight than they would without the presence of the sulfate aerosols by increasing the aerosol size. Examination of the lifetime of clouds containing air pollution chemicals indicates that they exist longer, and that they reflect more sunlight than unpolluted clouds [*Kaufman et al., 2005; Kaufamn and Yoren, 2006; Teller and Levin, 2006*]

The smaller sized CCN, which often contain sulfates and nitrates, have become a central issue in climate change because they affect the radiation budget in two ways [*Charlson and Heintzenberg, 1995; Hobbs and Huebert, 1996*]. They directly affect the Earth's climate as they cool the Earth by reflecting a portion of incoming solar radiation back to space, and/or warm the Earth by absorbing and reemitting (both upward and downward) radiant energy that is being transmitted back into space. The magnitude of their effect depends on the size and the composition of the aerosol particles, as well as on the reflective properties of the underlying surface [*Twomey, 1977; Hobbs, 1993; Vong et al., 1998*]. They also assert an indirect effect on the climate by modifying the microphysical properties of clouds. If there were no aerosols in the atmosphere, it would be more difficult to form cloud droplets since they act as effective seeds for the formation and growth of clouds. Although CCN are only a fraction of the total aerosol particles, they play an important role in cloud formation and stability [*Hobbs et al., 1974; Fitzgerald et al., 1973*]. CCN strongly modulate cloud microstructure and hence the radiative properties, lifetime and spatial extent of clouds [*Charlson et al., 1987; Yum and Hudson, 2002*]. With the increase in aerosol concentrations, most scientists expect increased cloud droplet formation. However, the increased aerosol concentrations often results in the formation of a larger number of smaller droplets as the total amount of condensed water in the cloud stays relatively constant. These smaller droplets maintain longer residence times while reducing rainout rates and result in more sunlight being reflected back to space over longer periods. Thus, measurements of CCN concentrations provide us with information on the relationship between aerosols and clouds. This information is essential to improve estimates and obtain a better understanding of the indirect effect of aerosols on climate.

Minute amounts of particulate matter in the stratosphere, combined with increased levels of chlorine from the use of chlorofluorocarbons, have been held responsible for the aerosol chemical cycle that causes the Antarctic ozone hole [*WMO, 1995*]. Emission of aerosols by industrial activity and biomass burning are believed to be responsible for partially masking the expected increase in surface temperature associated with greenhouse gas radiative forcing [*IPCC, 1995; NRC, 1996A*].

As aerosol particles absorb or scatter radiation they play an essential role in the radiative transfer through the atmosphere. Aerosols affect optical sensor performance because of scattering along the line-of-sight of passive or active remote sensing observations, and they also affect the aesthetic viewing of natural settings. They also contain chemicals which have serious impacts on human health [*American Thoracic Society, 1996a, b*]. In order to fully comprehend the impact of aerosols in the future, important questions involving the effects of atmospheric aerosols on climate, atmospheric chemistry, and human health must be addressed [*NRC, 1998*]. One of the key strategies stated, to obtain a better understanding of the processes, is the development of remote sensing techniques to obtain aerosol parameters in clouds, such as composition and size distribution. The essential elements of the research strategy, proposed by the NRC, to answer the questions can be found in the report entitled Atmospheric Sciences Entering the Twenty-First Century [*NRC, 1998*].

2.2 Clouds

The World Meteorological Organization (WMO) defines a cloud to be an aggregate of minute, suspended particles of water or ice, or both, above the Earth's surface that are in sufficient concentrations to be visible. Clouds are an integral component of the Earth's atmosphere and cover between 60% and 70% of the Earth's surface area [*Quante, 2004*]. Their presence plays an important role in shaping the global climate since they have a strong impact on transmission of incoming solar radiation and trapping terrestrial radiation, as well as affecting the rate of precipitation. Table 2-2 lists some of the different cloud types which have an influence on Earth's climate. Any attempt by us to predict future changes in the climate system require us to observe and improve our understanding of the global distribution of clouds, their microphysical properties, and their impact on regional and global climate. Studying cloud structures and relating them to future predictions is complicated by two factors. First, clouds form and change rapidly over short time and space intervals and hence constitute one of nature's most variable components. Secondly, human-induced processes increasingly affect

Earth's climate and hence we also need to gain a precise understanding on how climate variations alter the physical and chemical processes that govern cloud formation and dissipation.

Table 2-2: Classification of cloud types [*Quante, 2004*]. Simplified classification based on [*Flossmann and Laj, 1998; WMO, 1975*]

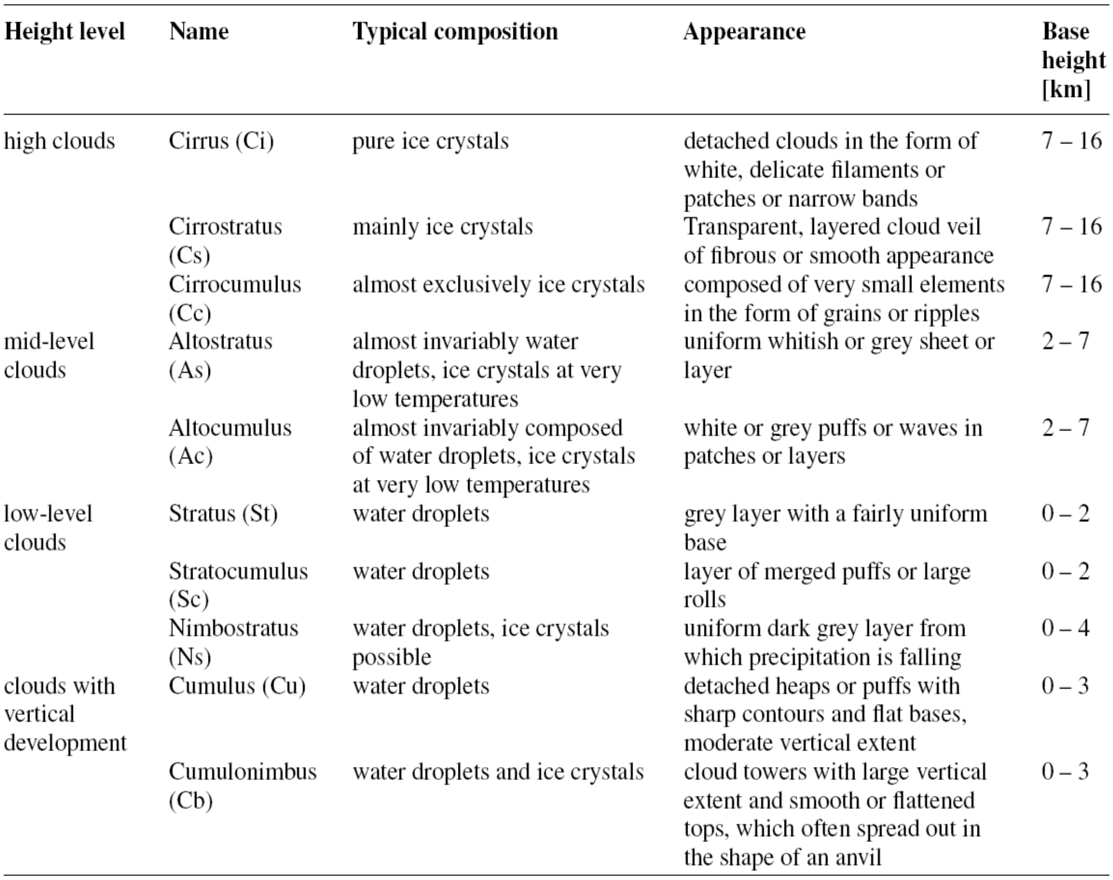

Height level	**Name**	**Typical composition**	**Appearance**	**Base height [km]**
high clouds	Cirrus (Ci)	pure ice crystals	detached clouds in the form of white, delicate filaments or patches or narrow bands	7 – 16
	Cirrostratus (Cs)	mainly ice crystals	Transparent, layered cloud veil of fibrous or smooth appearance	7 – 16
	Cirrocumulus (Cc)	almost exclusively ice crystals	composed of very small elements in the form of grains or ripples	7 – 16
mid-level clouds	Altostratus (As)	almost invariably water droplets, ice crystals at very low temperatures	uniform whitish or grey sheet or layer	2 – 7
	Altocumulus (Ac)	almost invariably composed of water droplets, ice crystals at very low temperatures	white or grey puffs or waves in patches or layers	2 – 7
low-level clouds	Stratus (St)	water droplets	grey layer with a fairly uniform base	0 – 2
	Stratocumulus (Sc)	water droplets	layer of merged puffs or large rolls	0 – 2
	Nimbostratus (Ns)	water droplets, ice crystals possible	uniform dark grey layer from which precipitation is falling	0 – 4
clouds with vertical development	Cumulus (Cu)	water droplets	detached heaps or puffs with sharp contours and flat bases, moderate vertical extent	0 – 3
	Cumulonimbus (Cb)	water droplets and ice crystals	cloud towers with large vertical extent and smooth or flattened tops, which often spread out in the shape of an anvil	0 – 3

Clouds form in response to changes in atmospheric conditions that vary on scales much larger than the cloud itself [*Lamb, 2003*]. Most clouds form by the buoyant lifting of moist air, which cools adiabatically by expansion under decreasing pressure, resulting in an increase in relative humidity. The upward vertical motion exposes the water vapor to cooler temperatures and allows mixing and condensation on CCN particles available in the atmosphere. Clouds begin to form as the water vapor condenses into water droplets. In the case of high clouds, such as cirrus clouds, the small droplets freeze so that the cloud is composed of small ice crystals.

Cloud formation is explained through heterogeneous nucleation. Heterogeneous nucleation requires the presence of water vapor and cloud condensation nuclei (CCN – aerosol particles up to ~1µm in size). Cloud condensation nuclei (CCN) are the atmospheric aerosol particles on which cloud droplets form when the supersaturation in a cloud reaches a value high enough that the particles begin to grow by water condensation [*Pruppacher et al, 1997; Lamb, 2003*]. Such particles support condensation at supersaturation levels well below those required for homogenous nucleation. CCN are hygroscopic in nature and act as seeds to accelerate the condensation process for converting water vapor into liquid water drops. Hygroscopic particles such as sodium chloride and ammonium sulfate absorb vapor and readily dissolve, resulting in a solution that has a saturation vapor pressure below that of pure water. The presence of CCN is critical for the formation of clouds, as they allow the droplets to form without high supersaturations due to the interaction of the water with the material of the nuclei [*Kyle, 1991*]. Hence, almost all cloud droplets in the atmosphere have their origin in heterogeneous nucleation processes, which involves atmospheric particles.

CCN found in the atmosphere typically consist of sulfates, sea salts, organic materials, black carbon, and minerals, in varying proportions depending on their geographic locations. The amount of water molecules CCN can take up depends on their chemical composition, size and the ambient relative humidity.

Not all aerosol particles which take up water grow into cloud droplets. Only those passing the critical radius are able to continue to grow and form cloud droplets. Their growth behavior is described by the Köhler theory [*Young, 1993; Seinfeld and Pandis, 1998*].

Dissipation of cloud structures occurs through evaporation when air subsides or when unsaturated environmental air is entrained into and mixed with saturated air. Entrainment of unsaturated environmental air decreases the positive buoyancy, kinetic energy and excess water vapor, which are essential elements for a cloud to sustain itself. Clouds are also dissipated by precipitation or sedimentation, when the particles grow large enough that they no longer can be supported by the buoyancy force. Radiative heating can also dissipate a cloud by increasing its temperature to values above the dewpoint temperature. For a detailed description of cloud formation, growth and microphysical properties the reader is directed towards Pruppacher et al., (1997), Young (1993) and Mason (1971). In the latter half of the next section we will briefly discuss the role that clouds play in the affecting Earth's climate.

2.3 Earth's Energy Budget

Energy transfer in the atmosphere is balanced in two distinctive bands, with the difference in the emission spectra of the two sources being due to their temperatures as given by Planck's law. Shortwave (SW) radiation, emitted by the sun, is concentrated in the visible wavelength spectrum, and longwave (LW) radiation, emitted by the Earth's surface and atmosphere, is concentrated in the IR spectrum. Figure 2-3 shows normalized black body emission spectra for temperatures of 6000K and 288K, which correspond to the equivalent blackbody temperatures of the sun and mean surface temperature of the Earth, respectively.

Now, if we assume the sun to represent a black body at 5800° K, the total flux emitted by it is obtained by integrating over the electromagnetic spectrum, which from Stephan-Boltzmann's law yield's,

$$F = \sigma T^4 , \qquad [2.1]$$

where

F is the flux emitted by the sun
σ is the Stephan-Boltzmann's constant, and,
T is the mean-temperature of the sun.

The Earth, with radius *R*, intercepts solar or shortwave radiation of cross-sectional area πR^2. At the Earth's distance from the sun, the solar radiation flux, or solar constant, is 1372 Wm^{-2} at the top of the atmosphere. A fraction, *A*, of the intercepted shortwave radiation, is reflected back by Earth's atmosphere and surface. This fraction is known as the Earth's albedo, and it play's a pivotal role in determining the Earth's temperature. If we assume the Earth to have a temperature T_e, then to maintain thermal equilibrium, the Earth and its atmosphere must radiate back at the same rate that it absorbs radiation. The Earth's outgoing longwave radiation maintains thermal equilibrium when

$$(1-A)\pi a^2 F = 4\pi a^2 \sigma T_e^4 \; . \qquad [2.2]$$

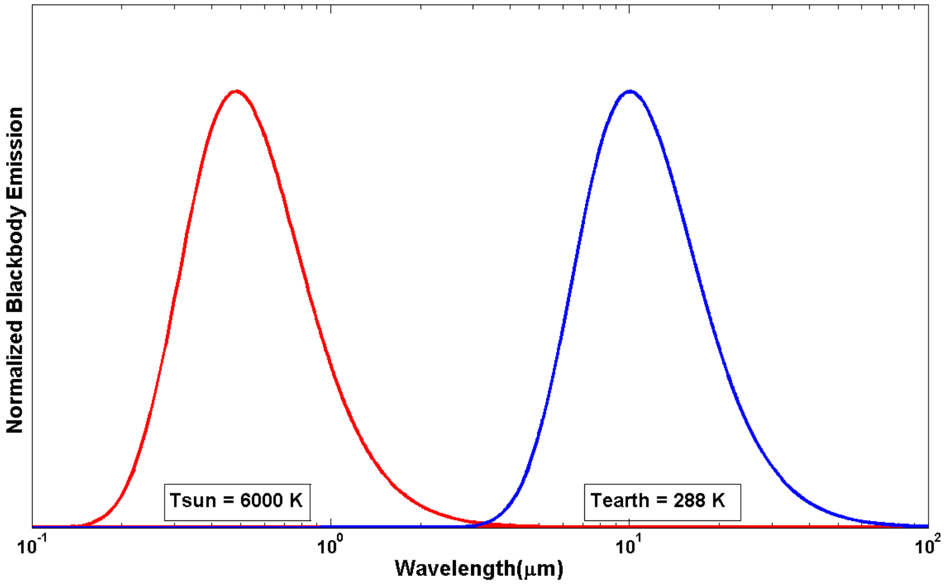

Figure 2-3: Blackbody emission spectra of the sun and Earth's surface based on Planck's law. The red curve represents the normalized black body emission spectra of the Sun (SW radiation) and the blue curve represents the normalized black body emission spectra of the Earth (LW radiation).

The terms on the left of Eq. 2.2 represent the incoming SW radiation and the terms on the right represent the outgoing LW radiation, assuming that the Earth radiates equally in all directions. Using Eq. 2.2, we can estimate the Earth's equivalent blackbody temperature, assuming an average of ~30% reflection of the incoming SW radiation, to be ~255° K. The difference between this calculated temperature and that of the global mean surface temperature (~288° K) is due to the absorption and radiation mechanisms that occur in the atmosphere and a small heat flux from deep in the Earth. The clear cloudless atmosphere is nearly transparent to SW radiation, which passes through the atmosphere and is absorbed by the surface. The LW radiation re-emitted by the Earth's surface is strongly absorbed in different overlaying layers in the atmosphere and is re-emitted, downward and upward from these layers as the radiation transfer migrates the long wave flux towards space. Reradiation of the LW radiation by the atmosphere is responsible for the higher equilibrium in the surface temperature over what it would be if the atmospheric window transmitted the infrared outgoing radiation as well as for the incoming solar SW radiation. Figure 2-4 shows the atmospheric absorption and shows the transmission windows for SW and LW radiation passing through the atmosphere between space and ground.

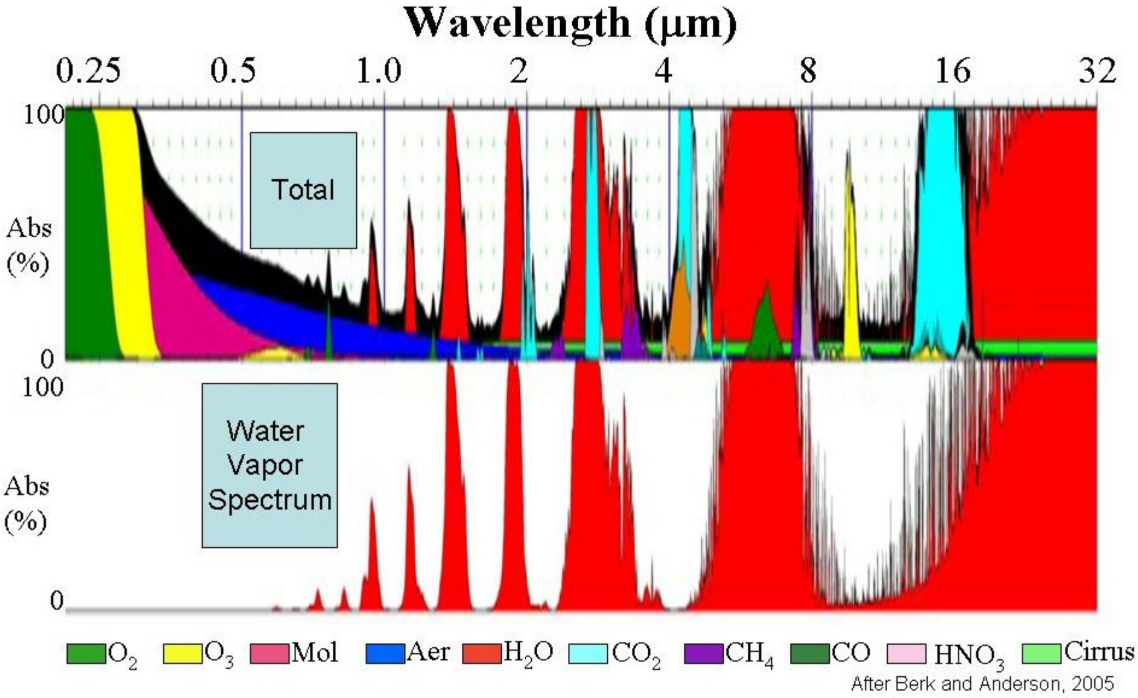

Figure 2-4: Fractional absorption of LW and SW radiation passing through the atmosphere (based on *Anderson et al., 2006*).

From Figure 2-4 we see that the UV wavelengths are absorbed due to photo-dissociation and photo-ionization of O_2 and O_3. However the visible portion of the solar radiation transmits nearly 85% of that spectrum to the surface under clear conditions. Most of the absorption of the returning LW radiation occurs in the troposphere. The LW radiation emitted by the Earth's surface is strongly absorbed by H_2O, CO_2, clouds, and variety of other trace constituents present in the atmosphere. Most of the energy is transferred between the surface and the atmosphere through the outgoing longwave radiation. Energy is also transferred through thermal conduction and convection, known as sensible heat and latent heat, as warm buoyant air rises upward and convects heat from the ground to the air.

The energy budget of the Earth takes into account all of the forcings that contribute to the transfer of energy between the surface and the atmosphere and vice-versa, and also the absorption and emission of radiation to and from space. An accurate estimate of the components of the incoming solar radiation and the outgoing infrared radiation provides a means of determining the Earth's present and future climate. Many attempts have been made to construct accurate global models to describe the mean energy budget for the Earth, following the first energy budget that was proposed by Dines (1917). However most of these early studies were severely limited by the lack of knowledge regarding the planetary albedo. Early estimates of the planetary albedo ranged from 40% - 50% [e.g., *Hunt et al. 1986*]. Over the past decade satellite measurements have provided improvements in estimating the global annual mean energy budget by narrowing the uncertainty in the planetary albedo and the transmission spectrum for outgoing longwave radiation. Satellite measurements from Nimbus-7 and the Earth Radiation Budget Experiment indicate that the planetary albedo is close to 30%, while results from the International Satellite Cloud Climatology Project [ISCCP, *Rossow and Zhang 1995*] indicate an albedo of 33%. Kiehl and Trenberth (1997), using detailed radiation models of the shortwave and longwave spectral regions, showed the role that various absorbers played in determining the radiative balance of the Earth's system and their dependence on the presence or absence of cloud's. Figure 2-5 shows the estimate of the annual global energy budget from the Kiehl and Trenberth model. The values put forth are not definitive, but give a sense of the various factors affecting the energy budget and the uncertainties and issues that need to be resolved to obtain a numerically accurate estimate.

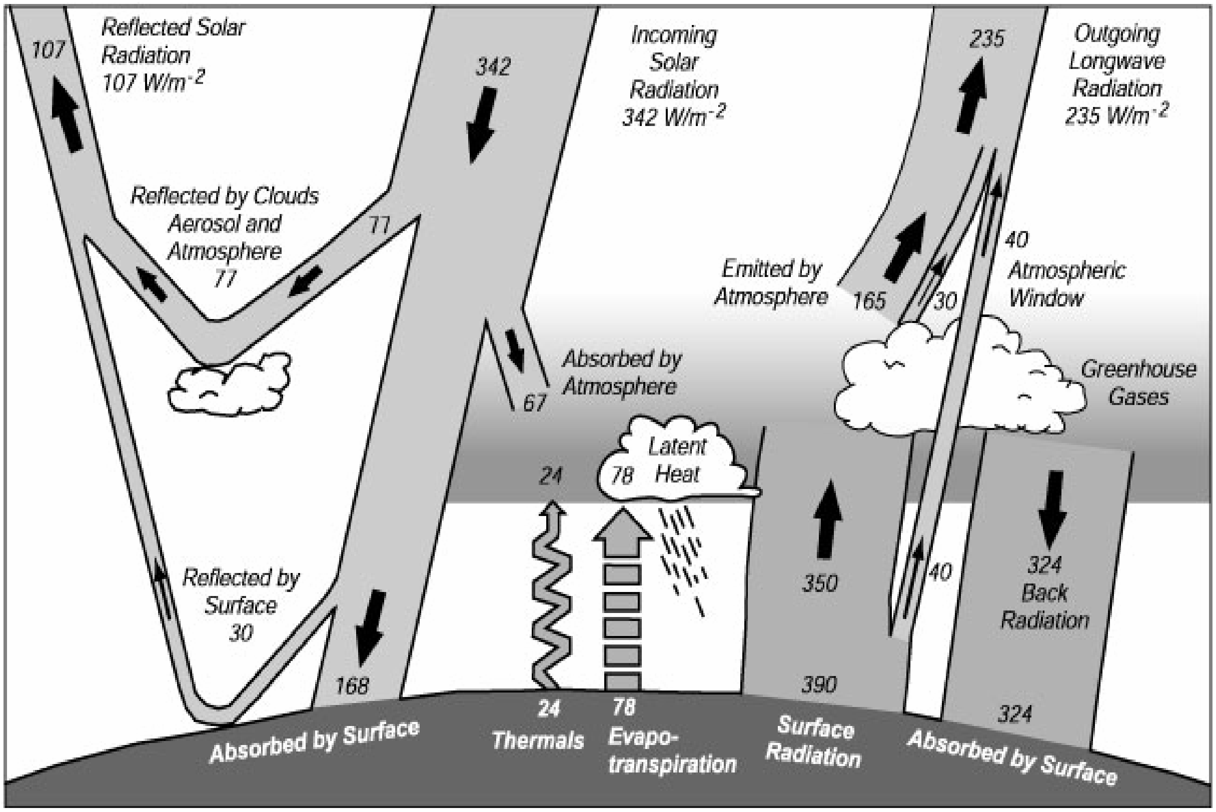

Figure 2-5: The Earth’s annual global energy budget based on Kiehl and Trenberth (1997).

With atmospheric and surface climate properties varying greatly over our planet it is important to be able to develop models that can predict Earth’s climate system on both regional and global scales. For example, the IPCC (1996, 2001) predicted an overall increase in global-mean atmospheric temperatures to occur in response to human-induced increases in atmospheric concentrations of heat-trapping "greenhouse gases" and aerosols. This fact is evident in the surface temperature data for the past few decades. Figure 2-6 shows the global surface temperature obtained since 1880, relative to 1951-1980 mean. We see a steady increase in the average surface temperature over the past few decades.

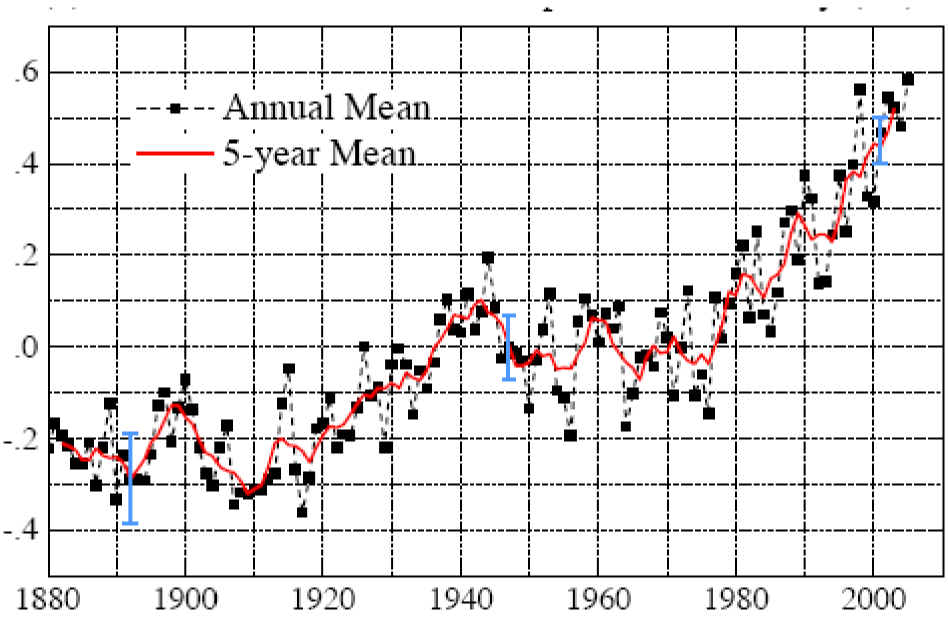

Figure 2-6: Global annual surface temperature relative to 1951-1980 mean based on surface air measurements at meteorological stations and ship and satellite measurements for sea surface temperature [*NASA Goddard Datasets & Images http://data.giss.nasa.gov/gistemp/2005*]. Temperatures show expected increase in response to elevated quantities of greenhouse gases being present.

Some, however, are puzzled by the fact that satellite temperature measurements indicate little, if any, warming of the lower to mid-troposphere. The NRC (2000) report on global temperature change points out that the temperature variations at the surface and aloft, over the past decades, have not tracked each other perfectly because they respond differently to natural and/or human-induced climate forcing during the past few decades. This brings up questions of whether observed changes agree with the predicted response due to the buildup of greenhouse gases in the atmosphere based on model simulations, and whether existing atmospheric observing systems and models are adequate for the purposes of monitoring the global climate system. To develop better models that can reproduce the variability in the data obtained, it is important that we reduce the uncertainties of how the climate responds to various forcings. In a report by the U.S Climate Change Science Program and the Subcommittee on Global Change Research (2006) several complex and unresolved issues related to the inadequacies in our climate were stated. Table 2-3 lists some of the important global-scale climate forcing factors and their likely individual effects on global-, annual-average temperatures based on the study. The top two rows are the primary natural forcing factors, while the other rows are the main human-induced forcing factors.

Table 2-3: Summary of the important global-scale climate forcing factors and their likely individual effects on global-, annual-average temperatures based on the report by the U.S Climate Change Science Program and the Subcommittee on Global Change Research (2006)

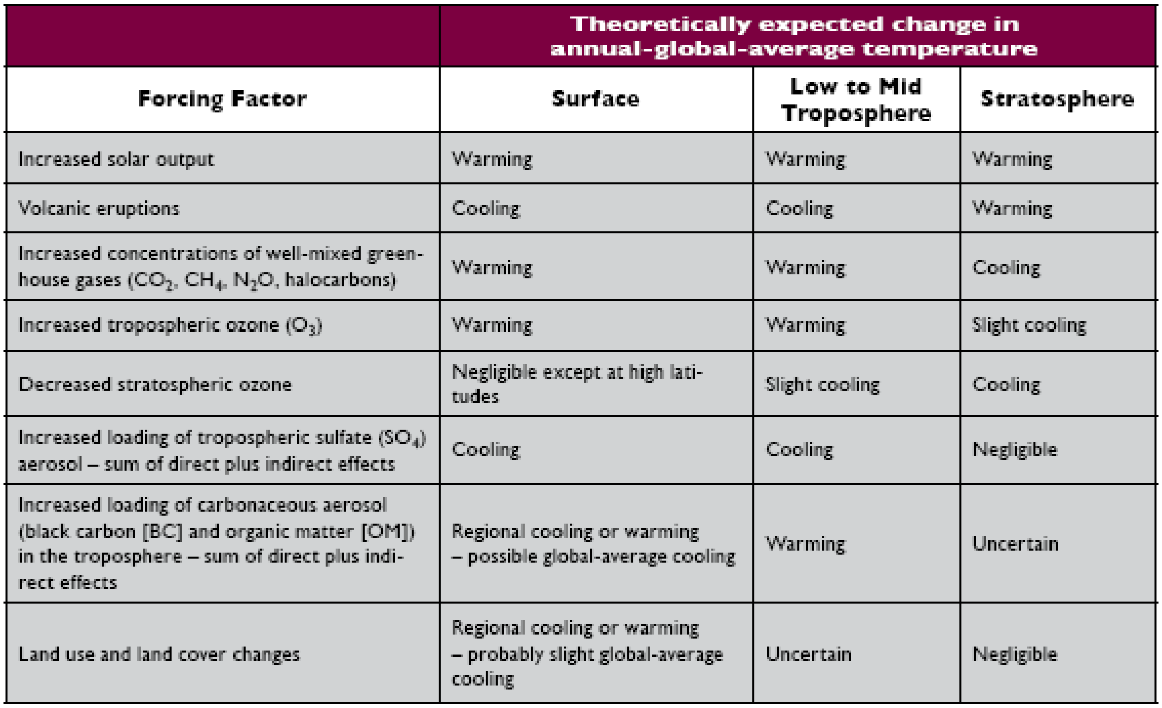

	Theoretically expected change in annual-global-average temperature		
Forcing Factor	**Surface**	**Low to Mid Troposphere**	**Stratosphere**
Increased solar output	Warming	Warming	Warming
Volcanic eruptions	Cooling	Cooling	Warming
Increased concentrations of well-mixed greenhouse gases (CO_2, CH_4, N_2O, halocarbons)	Warming	Warming	Cooling
Increased tropospheric ozone (O_3)	Warming	Warming	Slight cooling
Decreased stratospheric ozone	Negligible except at high latitudes	Slight cooling	Cooling
Increased loading of tropospheric sulfate (SO_4) aerosol – sum of direct plus indirect effects	Cooling	Cooling	Negligible
Increased loading of carbonaceous aerosol (black carbon [BC] and organic matter [OM]) in the troposphere – sum of direct plus indirect effects	Regional cooling or warming – possible global-average cooling	Warming	Uncertain
Land use and land cover changes	Regional cooling or warming – probably slight global-average cooling	Uncertain	Negligible

Despite improvements in our understanding of the various components of the energy budget, a number of key items remain uncertain. Further complicating the response of the different atmospheric levels to increases in greenhouse gases are other processes, such as those associated with changes in the concentration and distribution of atmospheric water vapor and clouds. Scientists predict that as temperatures in the atmosphere increase, the amount of water vapor will also increase, thereby acting as a positive feedback loop, which would serve to further increase global warming [*CCSP, 2006*]. Figure 2-7 shows the global annual-mean radiative forcing, their estimated magnitudes, and levels of scientific understanding, from 1750 to 2000, due to several factors. The rectangular bars indicate the central estimate of the forcing from each effect, and the lines show an estimated range of uncertainty. The quantitative estimates of the forcing due to the well-mixed greenhouse gases are known with a higher degree of scientific confidence than for other factors. It is evident that to be able to predict how the climate system will respond to the various forcings we will have to develop a better understanding, in particular, on the effect that clouds and aerosols have on changing Earth's climate.

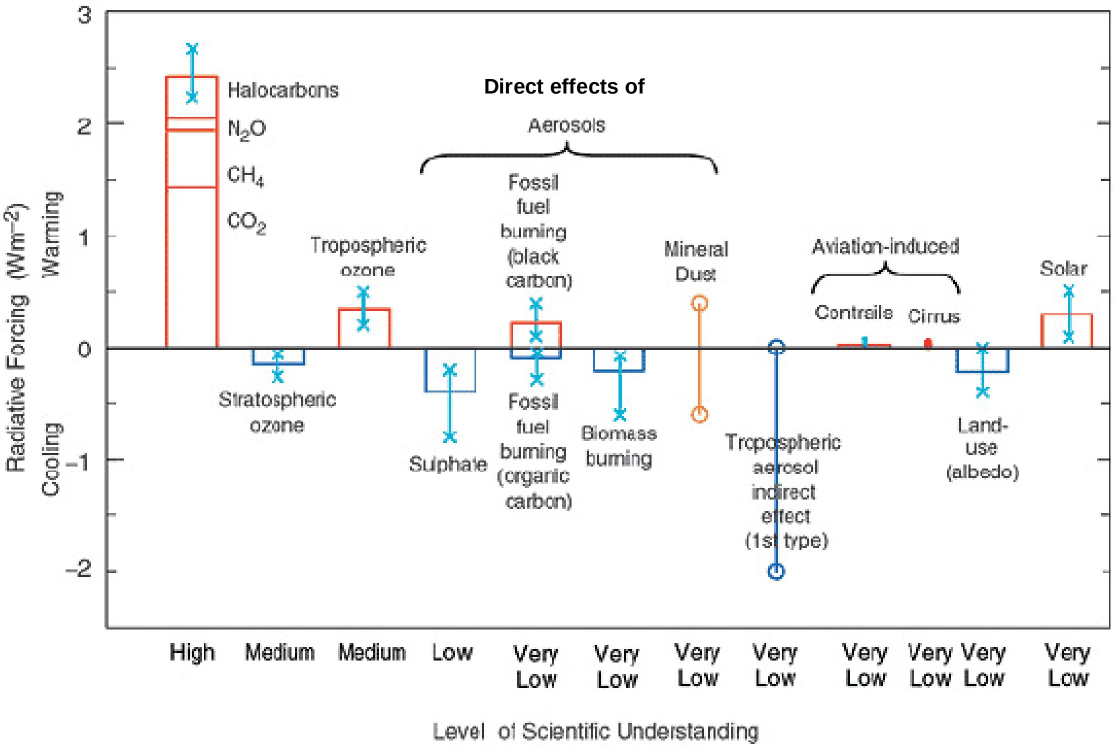

Figure 2-7: Estimates of the radiative forcing of various climate-altering effects, shown as a differential between the radiative forcing in 1750 and 2000; rectangular bars indicate best estimates while lines indicate the range of uncertainty; no rectangular bars are shown for effects for which the uncertainty is so large that no best estimate is possible; the qualitatively evaluated level of scientific understanding is shown beneath the horizontal axis (from *Houghton et al.*, 2001).

Aerosol effects on climate, as we discussed in section 2.1, are an important component of the Earth's radiation budget. They affect the radiative balance by,

1.) scattering and absorbing incoming solar SW radiation
2.) scattering and absorbing the SW radiation reflected from the surface
3.) scattering and absorbing outgoing LW radiation
4.) by acting as nucleation centers for the formation of clouds, which then scatter and absorb the shortwave and infrared radiations.

The first three effects described above affect the radiation budget directly and are known as the “direct effects”. The last described effect is known as the “indirect effect” because it influences the radiation budget by modifying the microphysical properties and the formation of cloud structures. The aerosol effects in the atmosphere are illustrated in Figure 2-8.

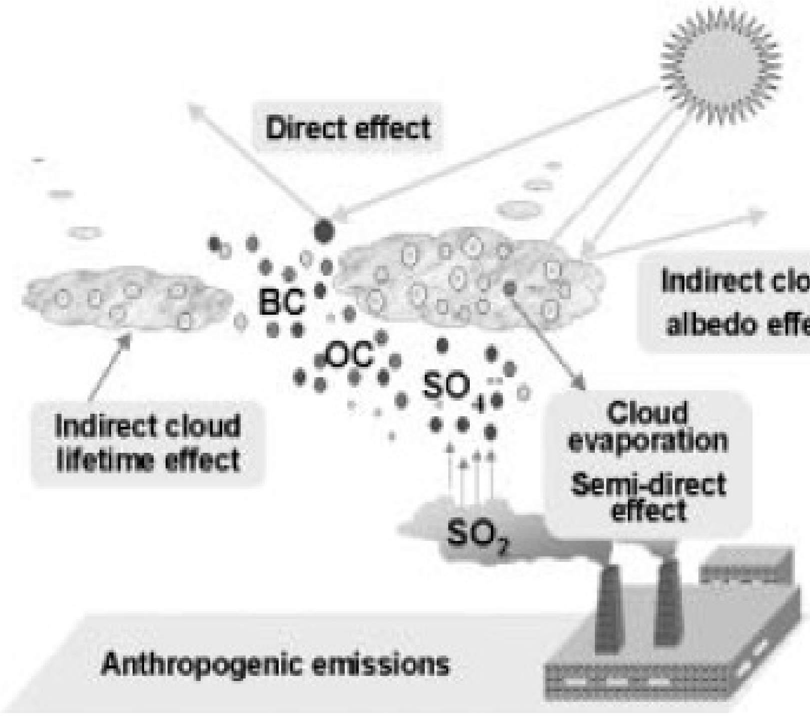

Figure 2-8: The direct and indirect effects of aerosols, and the importance of chemicals, indicated by black carbon, organic carbon, sulfate, and sulfur di-oxide. The direct effect is understood to enhance cooling of our atmosphere, while the potential of the indirect effect is still not thoroughly understood, though researchers claim the effect to assert a cooling influence. [*Quante, 2004*]

The influence of most aerosols on the radiation budget results in either warming or cooling effects. Most aerosols consist primarily of non-absorbing materials, such as sulfates and nitrates, and scatter the incoming radiation, resulting in a cooling influence because of the reflection back into space. However, absorption of SW or LW radiation by some aerosols particles, such as black carbon from burning of biomass and fossil fuels, results in a warming influence. The warming effect causes the temperature of the air to increase, thereby reducing the relative humidity and inhibiting aerosol growth. Inhibition of aerosol growth causes some of the cooling, due to the scattered radiation, to be offset due to the decrease in the cloud cover and the associated cooling. The reduction of cloud cover resulting from the warming influence of absorbing aerosols is known as the semi-direct effect [*Hansen et al., 1997; Ramanathan et al., 2001*]. Anthropogenic aerosols also influence the climate indirectly by changing the optical properties and precipitation from liquid-water clouds [*Lohmann, 2002*].

Although CCN are only a fraction of the total aerosol particles, they play an important role in cloud stability [*Hobbs et al., 1974*]. High CCN concentrations result in the increase of the number of cloud droplets, and decrease their mean size. CCN particles not only act as necessary precursors for cloud formation, but they also modulate the microstructure of clouds [*Charlson et al., 1987; Yu, 1996*]. The gravitational settling and precipitation rate also decreases as the cloud droplet size reduces and its microstructure changes [Young, 1993]. When precipitation is suppressed, water that would have been removed from the atmosphere remains aloft and can be transported to other locations before it is deposited to the surface. The effects of aerosols on cloud albedo due to an increase in aerosol concentration [*Twomey, 1977; Hobbs, 1993; Vong and Covert, 1998*] and the modification of cloud microphysics are known as the indirect effects and lead to increased lifetimes and thereby increased planetary albedo [*Hudson and Yum, 2001; Yum and Hudson, 2002*]. Aerosol effects arising from aerosol-cloud interactions can lead to potentially significant changes in cloud characteristics, such as cloud lifetimes, frequencies of occurrence, microphysical properties, and albedo [*Lohmann et al., 2000; Sherwood, 2002; Lohmann and Feichter, 2005*]. Clouds are important components in both solar thermal input and longwave radiative loss processes, and hence significantly influence the planetary radiation budget [*Ramanathan et al., 1989; Wielicki et al., 1995*], thus any effect caused by aerosols in perturbing cloud properties is bound to exert a significant effect on the radiation balance. With reference to Figure 2-7, note that the direct effect of aerosols, which includes the four categories bracketed under "Aerosols," are generally cooling effects that primarily occur in the regions withr aerosol concentrations. Direct forcing by sulfate aerosols is the simplest of the various aerosol effects to be included in global models. However, this forcing estimate is still relatively uncertain and requires a more focused effort in order to pin it down. The difficulty in this case emphasizes the problem of modeling aerosol-related forcings on the global scale. The first indirect effect of aerosols, which causes clouds to reflect more incoming radiation back into space, is shown to be a cooling effect that may either completely counteract greenhouse warming or may have no effect at all, depending on where the true forcing falls within the range of uncertainty. The second indirect effect of aerosols, due to increased cloud lifetimes, is not shown in this figure but is mentioned by the IPCC's report as being potentially important, but it is so uncertain as to prevent the panel from defining even a qualitative range of uncertainty. This effect is thought to result in cooling of comparable magnitude to the first indirect effect [*Rotstayn and Penner, 2001*], but it is not included in Figure 2-7 because it is even less well understood than the first indirect effect. The semi-direct effect, caused due to the evaporation of clouds through solar heating of the boundary layer by absorbing aerosols such as BC and a process termed as indirect soot forcing, which refers to the change in snow albedo due to BC aerosols, is so poorly understood that it is mentioned nowhere in the IPCC's discussion. The dependence of the indirect effects of aerosols on environmental parameters, on aerosol size, and on aerosol composition is poorly constrained, and often altogether ignored in global modeling efforts [*Seinfeld and Flagan, 1999*].

The presence of clouds is another prominent feature of our atmosphere that impacts the energy budget. Knowledge of the effects of clouds on the Earth's radiation budget is important both for accurate weather forecasting and for studying possible climate change. The Intergovernmental Panel on Climate Change (IPCC) points to clouds and related feedbacks as one of the main uncertainties in the prediction of future climate [*Houghton et al., 2001*]. The process and interactions are however not fully understood. Clouds and water vapor are essential stages in the cycling of water between the Earth and its atmosphere. Water vapor is the fundamental ingredient in the formation of clouds, and clouds act as sources and sinks of water vapor. Clouds influence climate by reflecting solar radiation, which asserts a cooling effect, but they also warm the planet by absorbing the infrared radiation, and reemitting it back downwards. Stephens (2005) states that "The "thermal absorbent" character of water is greatly enhanced when in a condensed phase. On a molecule by molecule basis, water in either solid or liquid form in the atmosphere absorbs more than 1000 times more strongly than in gaseous form." This enhanced absorption is inferred from the relationships between the broadband clear-sky emissivity and water vapor path and the equivalent broadband cloud emissivity and cloud liquid (or ice) water path, and is important because the presence of clouds plays a major role in absorption of LW radiation. Clouds affect Earth's climate in a number of additional ways, such as by distributing the effects of the latent heat of condensation from transporting heat, moisture and atmospheric trace constituents over large distances, and by precipitating water to the surface [*Fouquart et al., 1990; Arking, 1991; Chahine, 1992; Kiehl, 1994*]. They also play a key role in the atmospheric branch of the hydrological cycle, which is closely associated with the climate system.

The difficulty in associating the influence of clouds on the Earth's radiation budget arises because of two competing effects;

1) Albedo effect – the increase of the reflected SW radiation with increase in cloud cover,
2) Greenhouse effect – the decrease of emitted LW infrared radiation with an increase in cloud cover.

To be able to understand how they affect the radiative transfer, the radiative properties of clouds need to be known. Both effects depend not only on the amount of cloud cover, but also on their geometrical and microphysical properties. However, this information is not available for clouds even in crude approximation. The location of the cloud in the atmosphere also plays an important role in determining if it will assert a warming or cooling effect. Clouds that lie low in the atmosphere, such as cumulus and stratocumulus clouds, are typically thick and opaque. They tend to cause a cooling effect as they reflect most of the solar SW radiation back to space, allowing only a fraction of the radiation to reach the surface. Being near the surface and at almost the same temperature as the surface they radiate at nearly the same intensity as the surface and do not greatly affect the infrared radiation emitted to space. The LW radiation emitted downward from the base of low clouds does tend to warm the surface, but the cooling effect of these clouds dominates over the warming effect. The high clouds in the Earth’s atmosphere are highly transparent to shortwave radiation, but absorb the infrared radiation emitted by the Earth’s surface. They then emit the LW infrared radiation both out to space and back to the Earth’s surface. Because of their height in the atmosphere they exist at very low temperatures and consequently the energy radiated upwards into space is lower than it would be without the cloud. The additional energy radiated towards the surface causes a warming of the surface and atmosphere and these high clouds tend to promote a warming effect. Figure 2-9 illustrates the atmospheric influence of clouds depending on their location in the atmosphere.

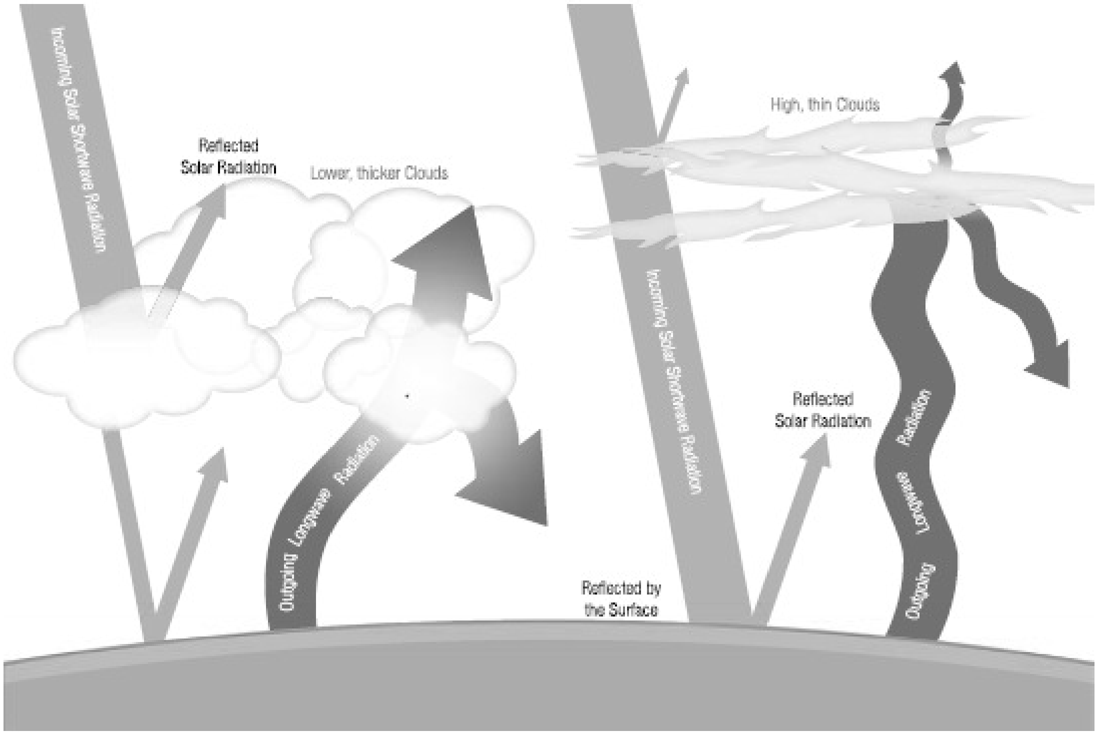

Figure 2-9: Low clouds effectively reflect SW solar radiation thus asserting a cooling effect on the planet. The higher clouds in allow most of the solar energy to pass through, but trap a large portion of the infrared radiation asserting a net warming effect on the planet [*NASA Facts, 2005*].

Because of the differences in how clouds affect the radiation balance, predicting the impact of any particular cloud on the temperature on Earth's climate system is difficult. Since information on the microphysical and radiative properties of clouds is not available on a global scale or for long time periods, the concept of cloud radiative forcing (CRF) is used to assess the radiative effects of clouds [*Charlock and Ramanathan, 1985; Ramanathan 1989; Harrison et al., 1990; Hartmann et al., 1993*]. The cloud radiative forcing calculates the amount by which the presence of clouds alters the top-of-the-atmosphere energy budget. The data used to calculate the CRF is taken from models and satellite observation. The net radiation at the top of the atmosphere is given by,

$$R = S(1-\alpha) - F = Q - F \qquad [2.3]$$

where

S	is the insolation
α	is the planetary albedo
F	is the outgoing LW radiation
Q	is the absorbed solar radiation

The net cloud radiative forcing, NCRF, is given by

$$NCRF = C - C_{clear} \qquad [2.4]$$

$$NCRF = SWCF + LWCF = (Q - Q_{clear}) - (F - F_{clear}) \qquad [2.5]$$

Typically, the short-wave cloud forcing (SWCF) is negative because of the albedo effect and the long-wave cloud forcing (LWCF) is positive due to the greenhouse effect. The net of the two effects depends on the cloudiness, and the geometrical and microphysical properties of cloud structures. Results obtained from the Earth Radiation Budget Experiment, in Table 2-4, show that clouds double the albedo of the Earth from a value of 0.15 to 0.3 [*Harrison et al., 1990*]. About 50 W/m^2 of SW radiation is reflected by clouds

Table 2-4: Estimates of the effects of clouds on the radiation budget at the top of the atmosphere. Data obtained from the Earth Radiation Budget Experiment. Global averages for years 1985 – 1989 [*Harrison et al., 1990*]

Quantities at the top of the atmosphere	**Global mean**	**Clear sky**	**Effect of clouds**
Outgoing terrestrial radiation	-234 (W/m^2)	-266 (W/m^2)	**32 (W/m^2)**
Absorbed solar radiation	239 (W/m^2)	288 (W/m^2)	**49 (W/m^2)**
Net radiation	5 (W/m^2)	22 (W/m^2)	**-17 (W/m^2)**
Albedo	30%	15%	**+15%**

and the LWCF due to clouds is 32 W/m^2. The net effect of the cloud population adds up to -17 W/m^2. Based on this study and the ISCCP data [*Rossow and Schiffer, 1999*], the results point to that fact that, at present, clouds assert a cooling effect on our planet. The Third Assessment Report (TAR) published by the Intergovernmental Panel on Climate Change (IPCC) in 2001 [*Houghton, 2001*] stated, that the Earth will warm by between 1.4 °C and 5.8 °C by the end of the twenty-first century. These estimates are based on modeling studies with global atmospheric circulation models. The human-induced effect on the planet, the uncertainty in the understanding of the physical processes involved, and the inability to describe the effects in the models are factors responsible for the range in the estimate of temperature change. Cloud processes and related feedbacks are explicitly mentioned in among the physical processes leading to large uncertainties, a fact that is confirmed by a recent quantification study of modeling uncertainties by Murphy et al. (2004).

The effects of clouds on LW and SW radiation compensate each other producing a much smaller net effect. Any process that affects one of the components without a reciprocal change in the other has a great potential for altering the Earth's radiation budget and thus climate. Therefore it is important that we understand how clouds will respond to changes in climate, which might be induced by an enhanced greenhouse effect or some other factor. Developing models to predict future climate changes without better understanding cloud dynamics and microphysics will lead to results with very low confidence. Anthropogenic impacts on clouds, such as the indirect aerosol effects and the semi-direct aerosol effect also need careful consideration to determine effects on cloud dynamics and its coupling to cloud microphysics.

2.4 Optical Scattering

Most of the light that reaches our eyes suffers some sort of scattering by the molecules and particles in atmosphere. Scattering is the interaction of electromagnetic waves with matter and occurs at all wavelengths in the electromagnetic spectrum. Scattering can be divided into two broad types, elastic scattering and inelastic scattering. Elastic scattering involves negligible loss or gain of energy by the radiation field (the volume scatter may be Doppler shifted by wind or by random thermal broadening), hence energy is conserved and the scattered frequency is nearly the same as the incident frequency. Inelastic scattering involves change in the energy of the radiation, as the internal energy levels of atoms and molecules are excited, and the scattered frequency is different from the incident frequency. In this section we discuss briefly the principle of two types of elastic scattering, Rayleigh scattering and Mie scattering. Inelastic scattering, particularly Raman scattering, will be discussed in the next chapter.

When a particle is placed in a radiation field, the charges within the particle respond to the electric field of the photon. As the EM wave interacts with a discrete particle, the electron orbits within the particle’s constituent molecules are perturbed periodically with the same frequency as the electric field of the incident wave. The charge distribution is stretched in the direction of the field, resulting in an induced electric dipole moment. The positive charges move in the direction of the force exerted on them by the field and the negative charges in the opposite direction. In the case of an electromagnetic wave at the frequency of light, where the electric field is rapidly oscillating (10^{14}-10^{15} Hz), the electrons respond according to the incident field intensity and direction, and the inertia of the positive charges limits their response. The changing field causes the charges to oscillate at the frequency of the incident radiation, and the moving charges in turn radiate an electromagnetic wave, i.e. the scattered field. In the process of elastic scattering, the scattered field from many scatterers results in a new wave front that has nearly the same frequency (only different by the Doppler shift experienced due to the random velocity of the scatterers and/or the ensemble motion due to transport of the volume by wind), propagation direction, and polarization as the incident radiation.

The scattering of light or other electromagnetic radiation in the atmosphere involves molecules and particles both larger and smaller than the wavelength of the incident radiation. Based on the size of the molecules and particles that scatter we divide elastic scattering into Rayleigh scattering and Mie scattering. The smallest particles that we consider as scattering light radiation are atoms and molecules, which are much smaller than the wavelength of visible light. Rayleigh scattering describes light scattering from molecules at all wavelengths. Basically any particle, which is small compared to the wavelength of the radiation ($<\sim 0.1\lambda$), scatters radiation very much the same way molecules do, and this type of scattering is known as Rayleigh scattering. The theory was explained by Lord Rayleigh in 1871 and explains the blue of the sky [*McCartney, 1976; Young, 1982; Van de Hulst, 1981*]. Rayleigh scattering is applicable to small, dielectric (non-absorbing), spherical particles. When the size of the particle is not negligible compared to the wavelength, a more complicated scattering pattern is known as the solution of Maxwell's equations for the case of Mie scattering [*McCartney, 1976*; *Bohren and Huffman, 1983; Bohren, 1992*]. The theory of Mie scattering (after Gustav Mie) encompasses the general spherical scattering solution [*Mie, 1908*] (absorbing or non-absorbing) without a particular bound on particle size, and can be used to describe scattering by large aerosol scatterers such as clouds particles, rain and hailstones. Mie scattering theory has no size limitations and converges to the limit of geometric optics for large particles, and to the Rayleigh scattering solution for small particles. The Mie scattering theory assumes the scatterers to be spheres, and due to the lack of any other easily applied method for calculating scattering by non-spherical particles, is most frequently used for approximating complex shaped aerosols as a distribution of spheres.

2.4.1 Rayleigh Theory

As described previously, Rayleigh scattering is applicable to particles whose size is small in comparison to the wavelength of radiation. Consider the case of an EM wave passing a small scatterer as shown in Figure 2-10. The interaction of the electromagnetic wave with the scattering molecule or particle gives rise to a dipole moment, induced by the incident field. The dipole is induced in the same direction as the incident electrical field vector, and its moment is proportional to the field with the same phase as that of the incident field. The oscillating dipole moment, which is driven by the incident wave, generates a secondary wave. The oscillatory motion of electronic charge in the molecule can be considered to be analogous to small-scale current in a Hertzian dipole antenna of microscopic dimensions. The following derivations are based on the work by McCartney (1976). For a particle of radius *r*, maximum value of the incident field E_o, and refractive index *n*, the dipole moment p_o is expressed as,

$$p_o = 4\pi\varepsilon_o r^3 \left(\frac{n^2 - 1}{n^2 + 2} \right) E_O \,. \qquad [2.6]$$

The average power of the secondary wave, *S*, is related to the power in the primary wave by the maximum value in the dipole moment p_o induced by the incident wave,

$$S = \frac{\omega^4 {p_o}^2 \sin^2 \phi}{32\pi^2 \varepsilon_o c^3 R^2} \qquad [2.7]$$

where ω is the electromagnetic angular frequency, ϕ is the angle between the dipole axis and any direction of interest and *R* is the distance along this direction. If we use Eq. 2.7, $\omega = 2\pi c/\lambda$ and apply the relationship in Eq. 2.6, we obtain the scattered intensity, $I(\phi)$, from a single particle.

$$E = \frac{d\Phi}{R^2 d\omega} = \frac{I}{R^2} \,. \qquad [2.8]$$

In Eq. 2.8 the irradiance E, which is the flux per unit wavelength per unit area, produced at a distance R, is related to the intensity I.

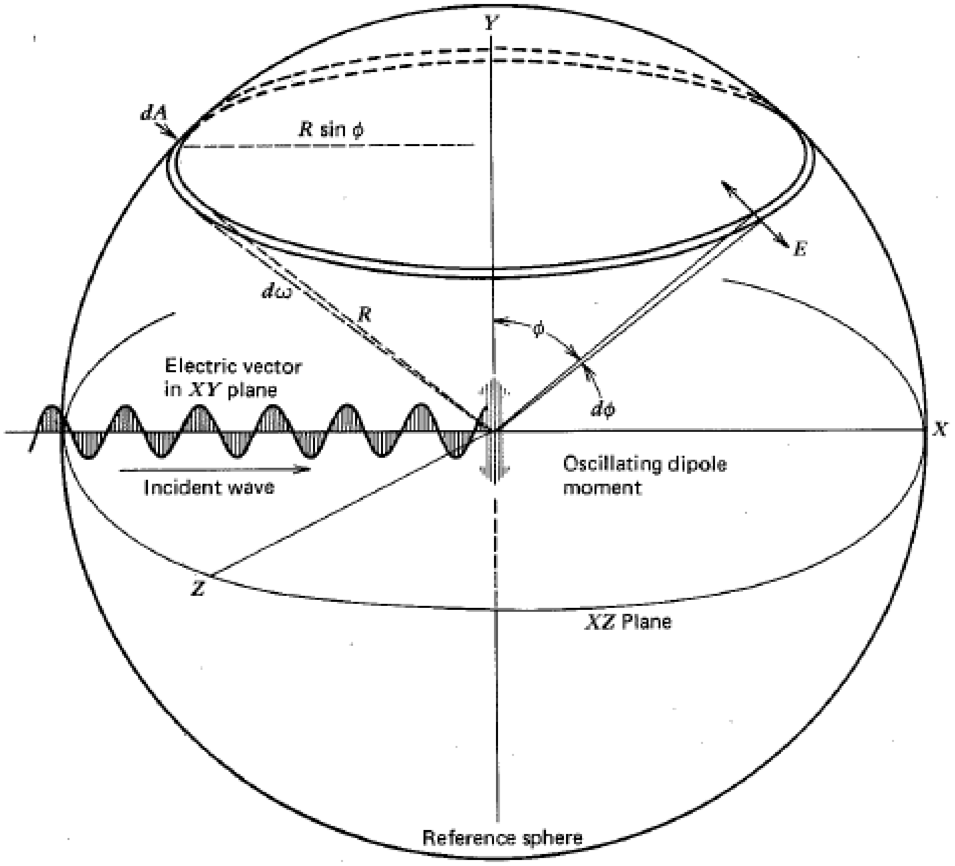

Figure 2-10: Geometry of molecular dipole radiation [*McCartney, 1976*]

The scattered intensity, I(ϕ), from a single particle is given by,

$$\mathrm{I}(\phi)=\frac{8\pi^4\varepsilon_o c r^6 \sin^2\phi}{\lambda^4}\left(\frac{n^2-1}{n^2+2}\right)^2 E_O{}^2. \qquad [2.9]$$

From Eq. 2.9, the scattered intensity and the energy removed from the incident beam is proportional to the sixth power of the radius for a spherical particle. We can also see that the scattered intensity is proportional to the 4th power of frequency (-4th power of wavelength). The scattered intensity is also governed by $\sin^2\phi$, which describes the dipole field. We can extend the above concepts and equations to define the angular and total scattering cross-sections, which are important in scattering theory, as they lead to several coefficients and expressions having great practical utility.

The angular scattering cross-section represents the ratio of the scattered intensity to the incident irradiance and is defined as the cross-section of an incident wave, acted on by a molecule, having an area such that the power flowing across it is equal to the power scattered by the molecule per steradian at an angle ϕ. When the scatterer is very small, in the case of Rayleigh scattering, the angular cross-section, $\sigma_p(\phi)$, is obtained by dividing Eq. 2.9 by Eq. 2.7, and is given as,

$$\sigma_{\mathrm{p}}(\phi)\mathrm{S} = \mathrm{I}(\phi) \qquad [2.10]$$

$$\sigma_{\mathrm{p}}(\phi) = \frac{16\pi^4 r^6 \sin^2\phi}{\lambda^4}\left(\frac{n^2-1}{n^2+2}\right)^2 . \qquad [2.11]$$

An expression identical to the one above can be obtained from Mie theory when the particle satisfies the small-size requirement $r < 0.01\lambda$.

The total scattering cross-section is defined as that cross-section of an incident wave, acted upon by the molecule, having an area such that the power flowing across it is equal to the total power scattered in all directions. Therefore the total scattering cross-section is obtained by taking the integral of the angular cross-section over 4π steradians,

$$\sigma_{\mathrm{p}} = \int_0^{4\pi} \sigma_{\mathrm{p}}(\phi)\mathrm{d}\omega = \int_0^{4\pi} \frac{16\pi^4 r^6 \sin^2\phi}{\lambda^4}\left(\frac{n^2-1}{n^2+2}\right)^2 d\omega . \qquad [2.12]$$

Substituting $d\omega = 2\pi\sin\phi\, d\phi$ into the above equation, we obtain

$$\sigma_{\mathrm{p}} = \frac{32\pi^5 r^6}{\lambda^4}\left(\frac{n^2-1}{n^2+2}\right)^2 \int_0^{4\pi} \sin^3\phi d\phi . \qquad [2.13]$$

$$\sigma_{\mathrm{p}} = \frac{128\pi^5 r^6}{3\lambda^4}\left(\frac{n^2-1}{n^2+2}\right)^2 . \qquad [2.14]$$

While the above equations account for the redistribution of incident radiation due to light scattering, incident radiation may also be absorbed by the particle. The rate of the total amount of incident energy removed from the incident beam due to interactions with a single particle is calculated directly from the extinction cross section. The extinction cross section represents loss of energy from the incident beam due to both scattering and absorption. The extinction cross section, σ_{ext}, may be expressed as

$$\sigma_{ext} = \sigma_{abs} + \sigma_{sca}, \qquad [2.15]$$

where σ_{abs} and σ_{sca} are the absorption and total scattering cross-sections, respectively, and have dimensions of area. For most aerosol particles and non-absorbing molecules, the extinction cross-sections depend only on the total scattering cross-section. Also, the concepts of efficiency factors, which are widely used in Mie theory, are applicable to small particles in the Rayleigh regime. The scattering efficiency factor is defined as the ratio of the total scattering cross-section to the geometric cross-section of the particle.

For particles that can be assumed to be spherical, the efficiency factor, Q, is given as

$$Q_x = \frac{\sigma_x}{\pi r^2}, \qquad [2.16]$$

where the subscript x could refer to extinction, absorption or scattering. Hence, we can write

$$Q_{ext} = Q_{abs} + Q_{sca}. \qquad [2.17]$$

From Eq. 2.14 we can deduce the total scattering efficiency of a small sphere to be

$$Q_{\mathrm{SCA}} = \frac{128\pi^4 r^4}{3\lambda^4}\left(\frac{n^2-1}{n^2+2}\right)^2. \qquad [2.18]$$

Thus, we see that for small particles the scattering efficiency is dependent on the wavelength and can be used to explain the blue of the sky. The particles that are small in comparison with the wavelength are inefficient scatterers, but their efficiency rises rapidly with particle size. However, this relationship is not maintained beyond r = 0.01λ, which can be considered to be an upper limit for Rayleigh scattering calculations.

2.4.2 Mie Theory

When the particle dimensions are appreciable compared to the wavelength of the incident radiation it is no longer sufficient to consider merely an induced dipole in the scattering analysis. The scattering process is more complex, as a three-dimensional charge distribution is set up within the scatterer with non-vanishing quadrupole and higher moments. Such scattering by particles, whose size is greater than about 0.01 times the wavelength of the light, is called Mie scattering. Mie scattering is characterized by a complicated dependence of scattered light intensity on the angle of observation, and an increasing component of forward scatter compared to backscatter intensity, as the particle size increases. Also, unlike Rayleigh scattering, there is little dependence on wavelength when the particle size becomes large compared with the wavelength, as can be observed in the scattering of light by cloud particles. Thus a white cloud and a blue sky symbolize the limits for the two types of scattering.

The theory developed by Lorentz in 1890 and Gustav Mie in 1908 is typically used to describe the scattering of light by aerosols. This theory can only be applied to particles that are spherical or ellipsoids, therefore, complex shaped aerosols are frequently assumed to be a distribution of spheres for this analysis. Mie theory solves Maxwell's equations for the electromagnetic fields within a dielectric sphere in terms of an expansion in spherical harmonics and Bessel functions. The properties of the scattered wave emerge in terms of the dimensionless size parameter,

$$\alpha = \frac{2\pi r}{\lambda} = kr. \qquad [2.19]$$

When the size parameter is less than 0.2, scattering by particles may be described using the Rayleigh theory. Otherwise, scattering by larger particles is typically described using the Mie theory. Since the derivation of the scattering formulas resulting from Mie theory is tedious, only a few of the results are presented here, based on work from McCartney (1976) and Bohren and Huffman (1983).

The angular characteristics of Mie scattering for all particle sizes and wavelengths are expressed by two intensity distribution function i_1 and i_2. The light scattered by a particle at an observational angle θ may be treated as consisting of two components, which are polarized perpendicular and parallel to the plane of of polarization of the incident EM wave. These components are proportional to the two intensity distributions i_1 and i_2, respectively. These functions represent the primary feature from Mie theory and depend on the size parameter, α, the refractive index, m, and the angle θ. The intensity functions are calculated from an infinite series and are given as,

$$i_1 = \left| \sum_{n=1}^{\infty} \frac{2n+1}{n(n+1)} \left[a_n \pi_n(\cos\theta) + b_n \tau_n(\cos\theta) \right] \right|^2 . \qquad [2.20]$$

$$i_2 = \left| \sum_{n=1}^{\infty} \frac{2n+1}{n(n+1)} \left[a_n \tau_n(\cos\theta) + b_n \pi_n(\cos\theta) \right] \right|^2 . \qquad [2.21]$$

Each series converges slowly, and when α is greater than unity the number of terms required for satisfactory convergence is somewhat greater that the value of α. The scattered waves consist of partial waves radiated by the multipoles formed by the electric charges constituting the particle. The first partial wave emanates from a dipole, the second from a quadrupole, and so on to higher orders. The amplitudes of the nth electric partial wave are given by the complex functions a_n and b_n.

$$a_n = \frac{\Psi_n(\alpha)\Psi'_n(m\alpha) - m\Psi_n(m\alpha)\Psi'_n(\alpha)}{\xi(\alpha)\Psi'_n(m\alpha) - m\Psi_n(m\alpha)\xi'_n(\alpha)} . \qquad [2.22]$$

$$b_n = \frac{m\Psi_n(\alpha)\Psi'_n(m\alpha) - \Psi_n(m\alpha)\Psi'_n(\alpha)}{m\xi(\alpha)\Psi'_n(m\alpha) - \Psi_n(m\alpha)\xi'_n(\alpha)} . \qquad [2.23]$$

The values of a_n and b_n are found from Ricatti-Bessel functions, whose arguments are formed from particle characteristics α and m. The Ricatti-Bessel functions Ψ and ξ are defined in terms of the half-integer-order Bessel function of the first kind ($J_{n+1/2}(z)$), where

$$\Psi_n(z) = \left(\frac{\pi z}{2}\right)^{\frac{1}{2}} J_{n+1/2}(z) \qquad [2.24]$$

$$\xi_n(z) = \left(\frac{\pi z}{2}\right)^{\frac{1}{2}} H_{n+1/2}(z) = \Psi_n(z) + i\mathrm{X}_n(z) . \qquad [2.25]$$

and where $H_{n+1/2}(z)$ is the half-integer-order Hankel function of the second kind. The parameter X_n is defined in terms of the half-integer-order Bessel function of the second kind, $Y_{n+1/2}(z)$,

$$\mathrm{X}_n(z) = -\left(\frac{\pi z}{2}\right)^{\frac{1}{2}} Y_{n+1/2}(z) . \qquad [2.26]$$

The angular dependent function π_n and τ_n are expressed by the Legendre polynomials as

$$\pi_n(\cos\theta) = \frac{P_n^{(1)}(\cos\theta)}{\sin\theta} . \qquad [2.27]$$

$$\tau_n(\cos\theta) = \frac{dP_n^{(1)}(\cos\theta)}{d\theta} . \qquad [2.28]$$

When a particle is illuminated by unpolarized light represented by two electric vectors of equal magnitude perpendicular and parallel to the plane of observation but having no coherent relationship, the scattered light consists of two incoherent components given as

$$I(\theta) = E\frac{\lambda^2}{4\pi^2}\left(\frac{i_1 + i_2}{2}\right). \qquad [2.29]$$

Proceeding as we did for Rayleigh scattering we can obtain the angular scattering coefficient.

$$\sigma_{\mathrm{p}}(\theta)=\frac{I(\theta)}{E_o}=\frac{\lambda^2}{4\pi^2}\left(\frac{i_1+i_2}{2}\right). \qquad [2.30]$$

The total scattering coefficient is then obtained by integrating the above equation over 4π steradians.

$$\sigma_{\mathrm{p}}=\frac{\lambda^2}{4\pi}\int_0^{\pi}\left(i_1+i_2\right)\sin\theta d\theta. \qquad [2.31]$$

For purposes of computation the above equation is usually represented in terms of a_n and b_n as

$$\sigma_{\mathrm{p}}=\frac{\lambda^2}{2\pi}\sum_{n=1}^{\infty}(2n+1)(|a_n|^2+|b_n|^2). \qquad [2.32]$$

Dividing the above expression by the geometric cross-section, πr^2, gives the scattering efficiency factor

$$Q_{sca}=\frac{2}{\alpha^2}\sum_{n=1}^{\infty}(2n+1)(|a_n|^2+|b_n|^2). \qquad [2.33]$$

Figure 2-11 shows the scattering efficiency calculated using Mie theory for various values of the size parameter. When α is very small, the value of the efficiency factor is much smaller than unity. Particles in this region comprise of Rayleigh scaterers, and these particles scatter far less flux than would be intercepted by its geometric cross-section. As α increases, the efficiency factor rises to a maximum value near four and then slowly converges to an average value of two. For particles in the Mie regime, two characteristics are noted. The large maxima and minima ripple structure is observed due to the complex interactions of scattered and refracted rays that result in constructive and destructive interference along different paths. The ripple-like structure in the form of small extremely sharp peaks and troughs is observed for non-absorbing particles if the real part of the refractive index n is larger than 1. These ripple-like fluctuations result from the resonances of virtual modes [*Bohren and Huffman, 1983*]. In addition the efficiency factor converges to a value of two indicating that twice as much energy is removed than expected based on the geometric cross section. This is referred to as the extinction paradox. In actuality, one half of the energy is removed by scattering/extinction, while the second half is removed via near-forward angle diffraction and the efficiency of each of these factors is 1.

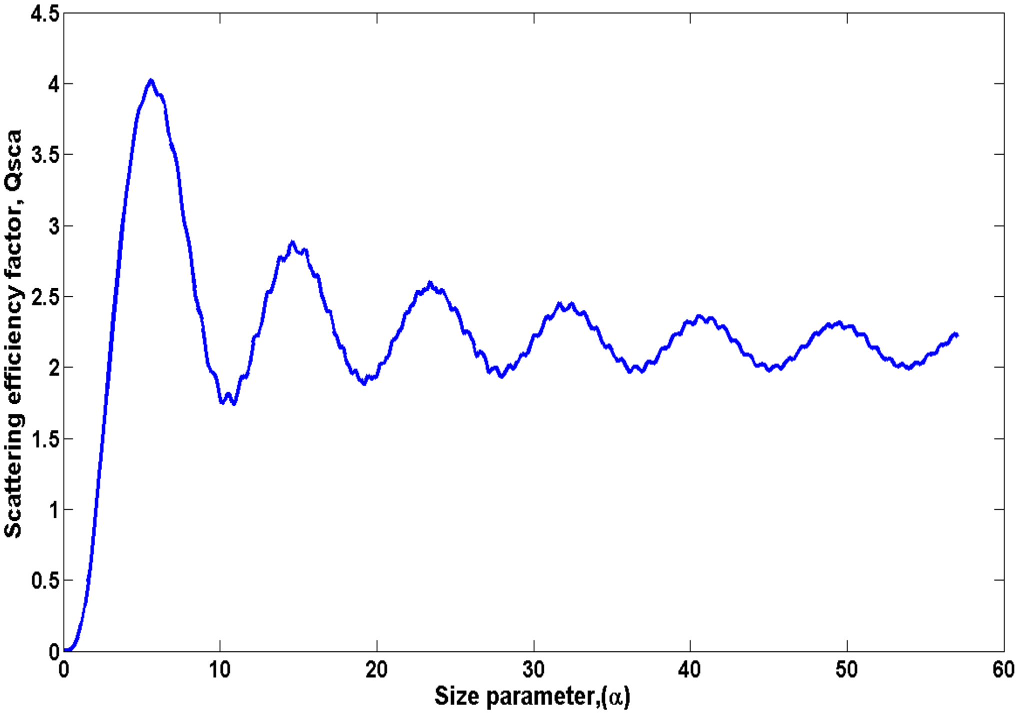

Figure 2-11: Scattering efficiency factor versus size parameter calculated using Mie theory.

The scattering of electromagnetic energy in the atmosphere is as complex as it is important, and hence this section was not an attempt to provide the reader with a complete tutorial on elastic scattering, but to introduce the concepts to the reader. The reader is referred to Van de Hulst (1981), Bohren and Huffman (1983), and McCartney (1976) for in-depth analyses of the theory and concepts related to the topic.

Chapter 3

Instrumentation and Measurement Techniques

3.1 Introduction

Historically, measurements of our atmosphere have been done using single-point sensors. Although these instruments are usually precise and accurate, they fail to provide us with continuous spatial and temporal coverage of data to describe the parameter variations and dynamical effects. During the past few decades, since the advent of the lasers and other technologies, active remote sensing instruments have been developed which help us to observe and continuously monitor the Earth's surface and atmosphere on a three-dimensional scale. These measurements have greatly improved our understanding of the environment and the functioning of its processes. The remote probing techniques of the atmosphere using laser sources are called LIDAR, described by its acronym Light Detection and Ranging; it is the application of radar at optical wavelengths. In this chapter we briefly describe the theory of operation and measurement techniques of Penn State's LAPS Raman lidars.

3.2 Lidar Atmospheric Profile Sensor (LAPS) Lidar

The Lidar Atmospheric Profile Sensor (LAPS) instrument was built by the staff and graduate students of the Applied Research Laboratory and the College of Engineering of Penn State University, as an operational prototype for the U.S Navy. It is the third Raman lidar system designed and fabricated at Penn State. The LAPS Raman lidar provides the profiles of water vapor and temperature as real time data products to support requirements for profiles of RF-refraction and meteorological data [*Philbrick, 1998*]. The LAPS instrument uses Raman lidar techniques to provide simultaneous profiles of water vapor, temperature, ozone and optical extinction [*Philbrick, 2001*].

These measurements provide the key results for understanding the processes involved in the evolution of pollution episodes.

The LAPS laser transmitter sends a pulsed beam at the doubled (532 nm) and quadrupled (266 nm) wavelengths of the Nd:YAG laser into the atmosphere, and a telescope receives the signals that have been backscattered by the molecules and particles of the atmosphere. The time interval between the transmission of the pulse and the reception of its backscatter signals gives the altitude of the scattering volume. Measurements of the atmospheric properties and constituents are obtained from the return signal intensity at the transmitted wavelength as well as at Raman shifted wavelengths. LAPS was tested onboard a U.S. Navy ship, the USNS SUMNER during September and October 1996 while deployed in the Gulf of Mexico and Atlantic Ocean. Since then LAPS has been used in a number of research investigations, which have been primarily concerned with understanding air pollution episodes. PSU's LAPS is a rugged instrument that was designed for automatic operation to enable measuring in virtually any environment at any given time. Raman lidar measurements of atmospheric properties are expected to be the major tool to provide the meteorological data in the future.

Penn State University's LAPS lidar consists of more than twenty sub-systems to control its operation and obtain measurements. The primary subsystems of the LAPS instrument are the transmitter, receiver, detector, data collection electronics, and control system. The transmitter, receiver and control system are housed in a weather-sealed unit so that it can be deployed in the outdoor environment and operated under a wide range of environmental conditions. The unit includes an environmental control sub-system, with air-conditioning and heating, to maintain the instrument within a range of acceptable operating temperatures. This primary part of the instrument has been termed as the 'Deck Unit'. The deck unit also includes a safety radar system to automatically shut down the laser beam when an aircraft enters a 6º cone angle around the beam. Another system called the 'Console Unit' houses the command computer, detector, and the data analysis and display electronics. The console unit and the deck unit are connected by power lines and fiber optic cables used to control the system operation, and to transfer the received signals from the receiver telescope to the detectors. The primary subsystems of LAPS are summarized in Table 3-1.

Table 3-1: Summary of LAPS subsystems.

Transmitter	Continuum 9030 –30 Hz 5X Beam Expander	600 mJ @ 532 nm 130 mJ @ 266 nm
Receiver	61 cm Diameter Telescope Focal length – 1.5 m	Fiber optic transfer
Detector	Eight PMT channels Photon Counting	660 and 607 nm – Water Vapor 528 and 530 nm – Temperature 295 and 284 nm – Daytime Water Vapor 277 and 284 nm – Raman/DIAL Ozone 607, 530, and 284 nm – Extinction 532 nm – Backscatter (3m resolution)
Data System	DSP 100 MHz	75-meter range bins
Safety Radar	Marine R-70 X-Band	Protects 6° cone angle around beam

The transmitter is a Nd:YAG laser, which operates at a fundamental wavelength of 1064 nm. The Nd:YAG laser is pulsed at 30 Hz with an output power of 1.6 joules per pulse at 1064 nm. The laser transmits an average power of 48 Watts at its fundamental wavelength with a peak power of about 200 MW. Frequency doubling and quadrupling crystals are used to generate the second harmonic (532 nm) and fourth harmonic (266 nm) from the fundamental wavelength (1064 nm). The residual primary wavelength is then dumped inside the instrument on a water cooled surface by a dichroic beamsplitter, while the 532 nm and 266 nm beams are sent through a 5X beam expander and then into the atmosphere. It has been proposed to use the 355 nm transmission wavelength in the design of the Advanced LAPS (ALAPS) system [*Slick*, *2002*]. The laser transmitter system of LAPS is shown in Figure 3-1 . Characteristics of the transmitter section are given in Table 3-2 .

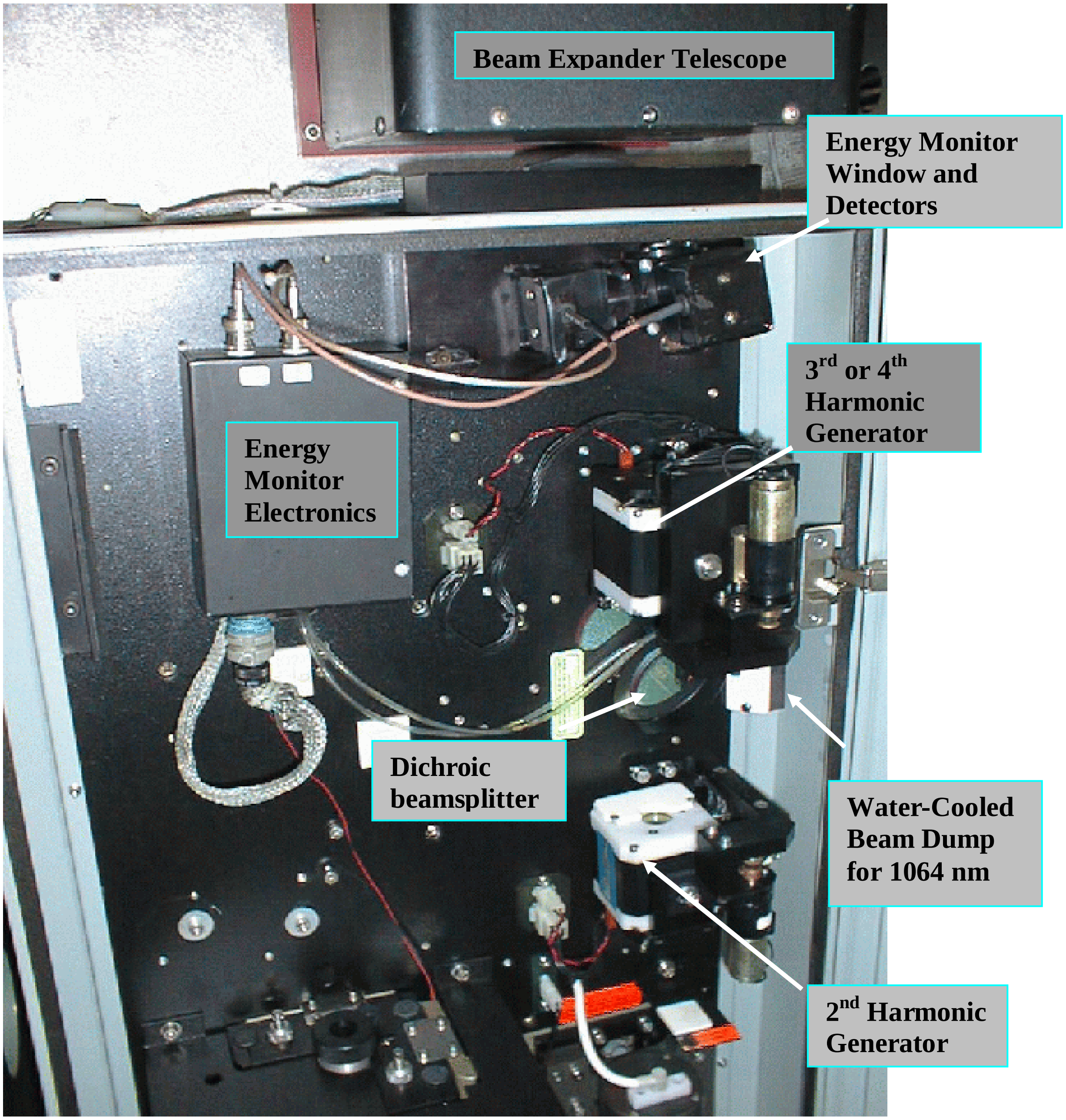

Figure 3-1: LAPS Transmitter optics (photo credit, C.R. Philbrick).

Table 3-2: LAPS transmitter characteristics [*Philbrick, 1998*].

Laser	Continuum Model 9030 with 5X Beam Expander
Pulse Repetition Frequency	30 Hz
Pulse Duration	8 ns
Fundamental Power	1.6 J/Pulse
Power Output at 1064 nm	Dumped into heat sink
Power Output at 532 nm	600 mJ
Power Output at 266 nm	120 mJ

The 5X beam expander is used to expand the beam from 9 mm diameter to 4.5 cm diameter. The larger cross-section area achieved with the beam expander serves two purposes by ensuring a power density below ANSI standards for near-field diffuse reflections and by reducing the beam divergence to a smaller field-of-view at a distance. The beam expander decreases the divergence of the transmitted beam by five times to about 80 μrad so that it is confined within the 250 μrad field of view of the telescope and fiber combination [*Slick, 2002*]. The deck unit also consists of a X-band radar, which is used to prevent any hazard due to reflection from an aircraft flying through the beam. The radar forms a 6° protecting cone around the beam and shuts the beam off automatically if it detects an intrusion. It is designed to automatically disable the laser Q-switch if a targets return signal is detected. The X-band radar operates at 9375 MHz with a peak pulse power of 10 kW.

Since a lidar receiver is a light collecting system and not an imaging system, the two main requirements of the receiver are to collect light backscattered from a minimum near-field distance to infinity, and to concentrate the collected light inside a field stop aperture or optical fiber [*Jenness et al., 1997*]. The receiver subsystem, shown in Figure 3-2 , consists of a prime focus reflecting telescope, constructed with a parabolic mirror 61 cm in diameter with a focal length of 1.5 m, and a fiber optic cable. The fiber optic cable is 1 mm in diameter and is located at the focal point of the mirror. The position of the fiber can be easily adjusted from the console by computer-controlled 3-axis micropositioners. The return signal is reflected and focused into a 1mm fiber as shown in Figure 3-2 . Fiber optic cables provide a convenient transfer of signal light from the telescope to the remote detector box, and the fiber also serve as a field stop to limit the transfer of background light to the detector box [*Jenness et al., 1997*]. The fiber optic cables transfer the return signal to the detector box in the console unit, where the Raman wavelengths are separated and the signal photons are converted to digital pulses by the photomultiplier tubes (PMT's), which are used in pulse detection mode. In the detector box, seven of the filters are selected at the vibrational and rotational Raman-shifted wavelengths corresponding to the laser wavelengths at 532 nm and 266 nm. The eighth filter is centered at 532 nm to measure direct backscatter. The light entering into the detector box from the fiber optic cable is then directed toward each of the filters using wavelength-separating (dichroic) and intensity-separating beamsplitters. The signals pass through their respective narrowband filters and are then transferred to photon counting PMT's. High sensitivity PMT's are used because the Raman scattered signals are weak due to small scattering cross-sections and low concentrations of scatterers. For optimal detection performance of the Raman signals, the PMTs should have high collection efficiency, good multiplication statistics, low noise, and high photocathode quantum efficiency in the spectral range of interest. In order to stabilize gain sensitivity, reduce dark current effects, and provide a linear response over a large dynamic range, the PMTs in the LAPS detector are used in the photon counting mode. This means the individually generated current pulses for each photoelectron are detected with a pulse height above a set threshold; rather than performing an A/D conversion of the DC current levels [*Chada, 2001*]. Data from the seven wavelength channels are stored simultaneously in half-microsecond channels providing range bins of 75 m resolution.

The console unit consists of the command computer, detector, photon counting electronics, and the data processor. It is possible to control all the subsystems of LAPS from the command/analysis computer in the console unit. When the system is in operation, the data acquisition system transfers the signals, as photon counts are detected by the PMT's, to the computer for processing. The raw data are processed in real time, and vertical profiles of atmospheric temperature, water vapor concentration, ozone, and raw photon counts are displayed. LAPS has a vertical resolution of 75 meters for seven of the PMT's and a vertical resolution of 3 meters for the backscatter detector. The raw data are used to profile the water vapor mixing ratio, ozone, temperature and extinction using the lidar equation, which will be discussed in 3.2.2 .

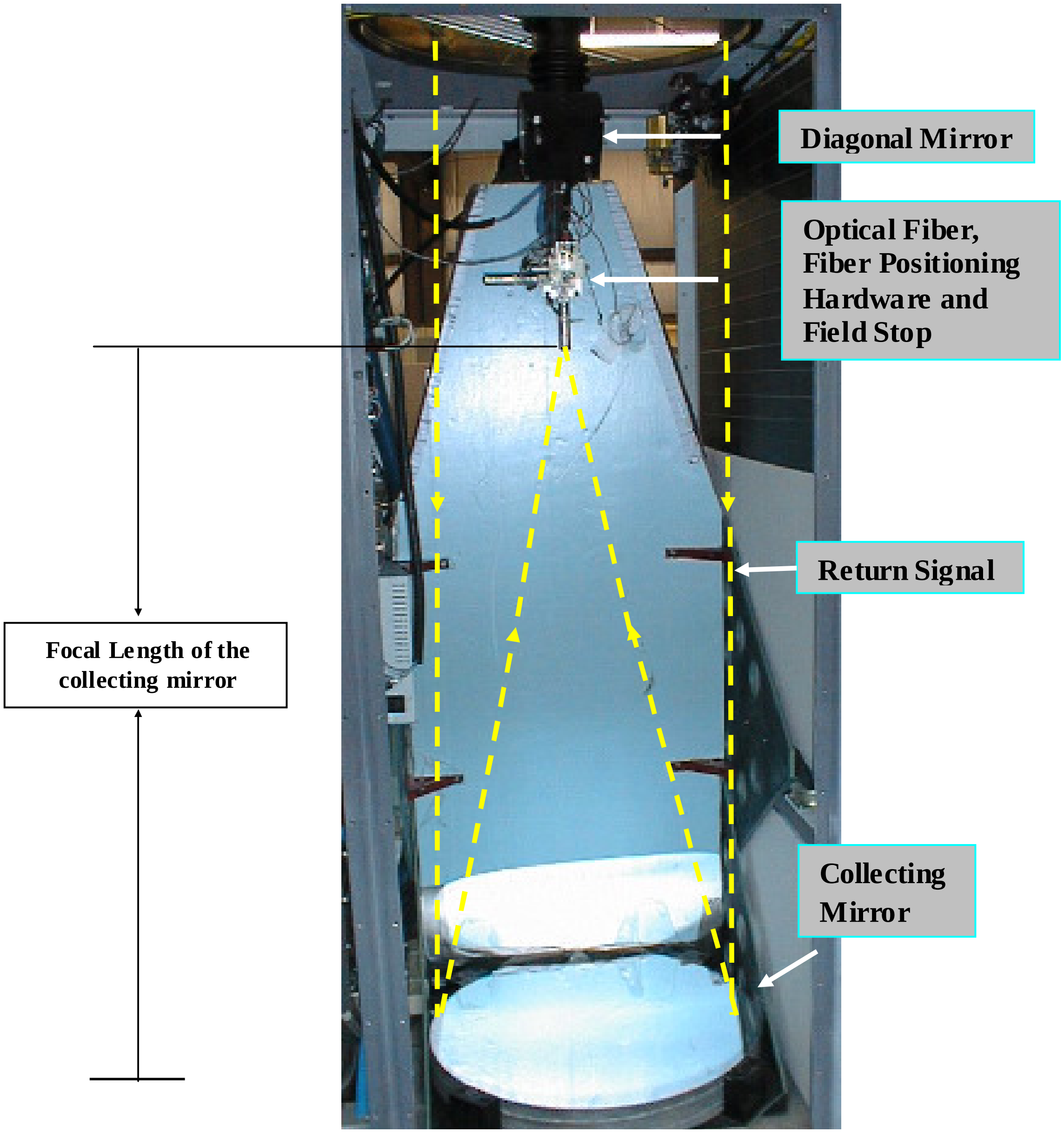

Figure 3-2: Receiver components and schematic of received beam (photo credit, C.R. Philbrick).

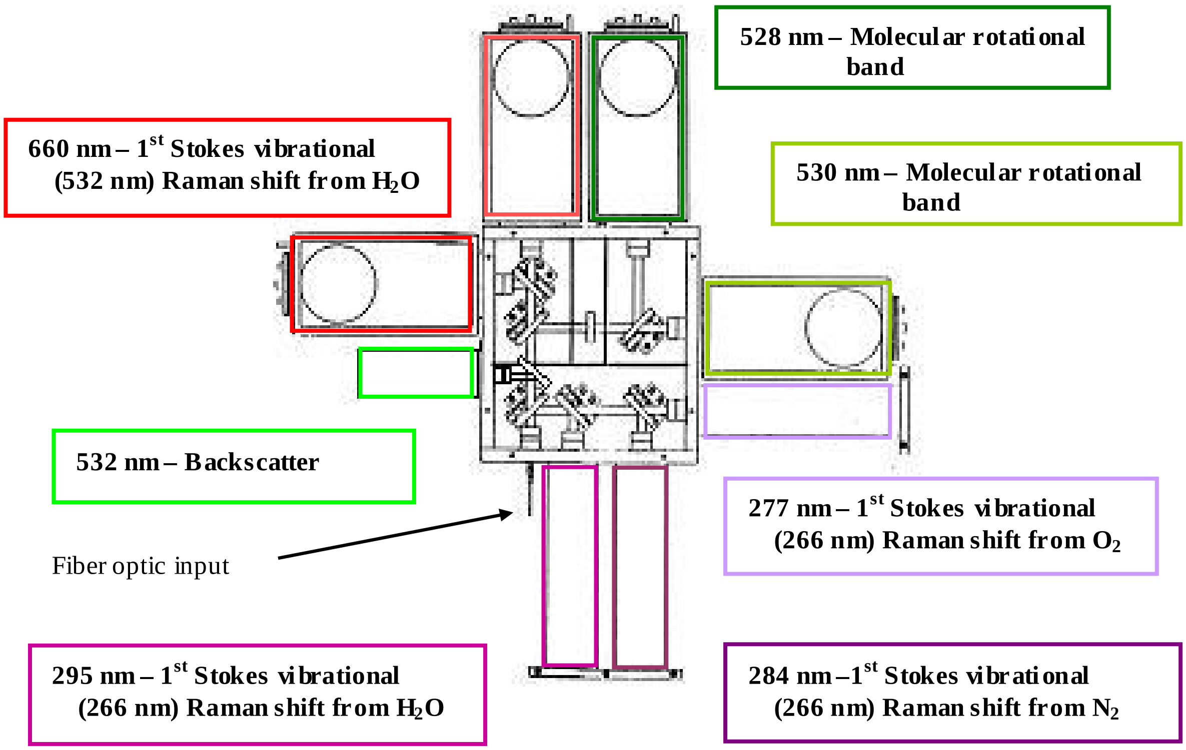

Figure 3-3: LAPS detector box with steering optics and the layout of each PMT [*Jenness et al., 1997*].

3.2.1 Raman Scattering

Penn State University's LAPS lidar measures the properties of the atmosphere from the Raman scatter signals generated by the laser beam interaction with the molecules of the atmosphere. The process of scattering of incident EM radiation by a molecule can be simply visualized as the electric field of a photon causing an atom or molecule to exist in a "virtual" energy state for the instant the photon interacts with the charge distribution of the molecule. The process is said to be elastic (Rayleigh scattering) if the scattered frequency is nearly the same as the incident frequency and inelastic

(Raman scattering) if the scattered frequency and the incident frequency are different. Raman scattering shifts the frequency of the scattered photon by the amount of the energy difference associated with the vibrational and rotational energy states of the scattering molecule. These scattering processes are shown schematically in Figure 3-4. The scattered radiation is seen to have a lower frequency when the molecule gains energy from the radiation field, a process referred to as the Stokes component. The anti-Stokes component or the higher frequency radiation results when the molecule loses energy to the radiation field by initially residing in an energy level above the final state. The anti-Stokes transition is rare for vibrational transitions of atmospheric molecules, because at normal temperatures the vibrational energy states above the ground state are rarely populated [*Measures, 1984*].

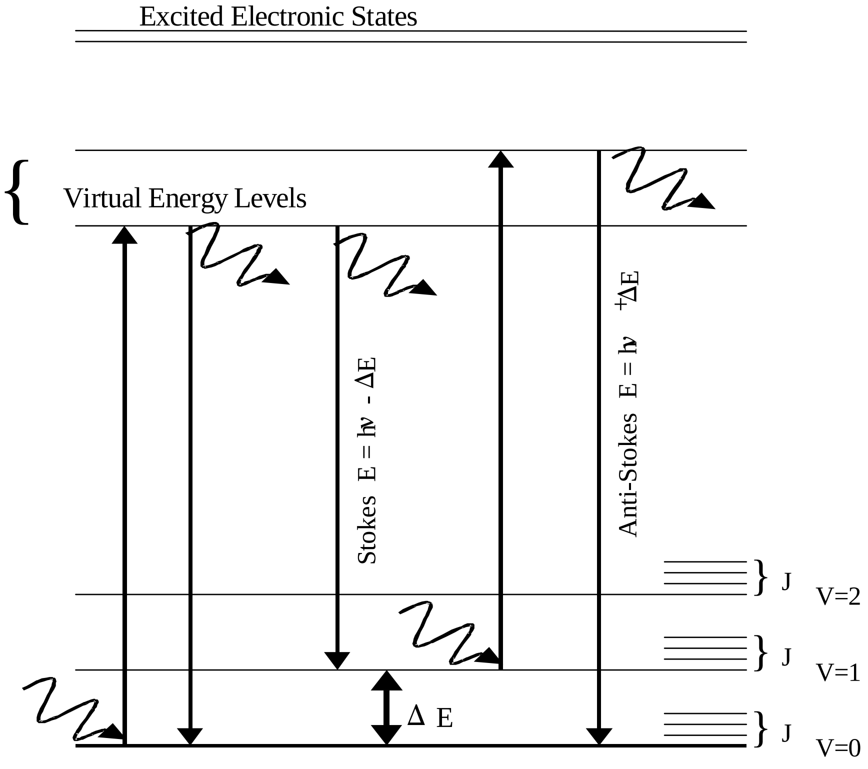

Figure 3-4: Energy diagram representation of the Stokes and anti-Stokes components due to Raman scattering [*Philbrick, 1994*].

The intensity of Stokes vibrational Raman scattering is roughly one-thousandth that of Rayleigh scattered component. Thus, the sensitivity of the process usually limits the detection to molecules occurring in high concentrations. Classification of the various optical interaction processes in laser remote sensing is given in Table 3-3. Raman scattering and fluorescence are the two interaction processes that exhibit inelastic scattering from the electronic energy states of molecules. Fluorescence can be sometimes used for high sensitivity detection of molecules, due to its large cross section. However, in the lower atmosphere fluorescence of major atmospheric molecules requires wavelengths in the deep ultraviolet region, and the intensity is reduced by collisional quenching by air molecules; depending on pressure, temperature and humidity. The emission spectrum of fluorescence is spread over many spectral lines in most molecules [*Kobayashi, 1987*]. These factors limit the application of this process in remote sensing in the lower atmosphere. The resonance scattering processes are currently being investigated for applications to measure trace constituents of species. The absorption process is well developed and used for DIAL (Differential Absorption Lidar) in many applications today for measurement of the concentrations of a particular species.

Table 3-3 Optical interaction processes used in laser remote sensing [after *Kobayashi, 1987*].

Interaction process	**Received wavelength**	**Interaction cross-section (m^2)**	**Detectable matter**
Mie scattering	λ_0	$10^{-28} \sim 10^{-10}$	Particle
Rayleigh scattering	λ_0	$\sim 10^{-29}$	Atom, Molecule
Raman scattering	$\lambda_0 \pm \Delta\lambda$	$10^{-35} \sim 10^{-30}$	Molecule
Fluorescence	$\lambda_0 \pm \Delta\lambda'$	$10^{-29} \sim 10^{-27}$	Atom, Molecule
Resonance scattering	λ_0	$10^{-18} \sim 10^{-15}$	Atom
Absorption	λ_0	$10^{-24} \sim 10\text{-}^{15}$	Atom, Molecule

The Raman scattering technique is advantageous because of its quantitative measurement capabilities using a single fixed wavelength. Raman scatter signals can be used to identify a trace constituent and quantify it relative to the major constituents of a mixture [*Measures, 1984*]. The magnitude of the frequency shift of the scattered photon provides a unique signature of the scattering molecular species. The frequency shift is independent of the incident laser wavelength and corresponds to the vibrational energy states of the molecular species. Observations of lidar measurements of Raman vibrational scattering were first presented by Leonard (1967). They measured the Raman scattering due to nitrogen to determine the atmospheric transmission as a function of range [*Leonard and Caputo, 1974*]. Cooney reported measurements of the Raman vibrational and rotational scattering from nitrogen [*Cooney, 1968*], water vapor [*Melfi et al., 1969; Cooney, 1970*], and ozone [*Cooney, 1986*]. Melfi et al. (1969) obtained the first profiles of water vapor from the Raman scattered signals. As summarized in Table 3-4, the LAPS instrument uses the vibrational Raman scattered signals to measure water vapor, ozone, and optical extinction, and uses the rotational Raman scatter signals to measure temperature. It collects the rotational Raman backscatter signals at 528 nm and 530 nm and the vibrational Raman backscatter signals at 607 nm, 660 nm, 277 nm, 284 nm and 295 nm. The 607 and 660 nm signals are the 1st Stokes vibrational Raman shifts from the N_2 and H_2O molecules in the atmosphere excited by the second harmonic (532 nm) of the Nd:YAG laser. The 277, 284 and 295 nm signals correspond to the 1st Stokes vibrational Raman shifts from the O_2, N_2, and H_2O molecules in the atmosphere excited by the fourth harmonic (266 nm) of the Nd:YAG laser. The ratio of the signals 660 nm/ 607 nm and 295 nm/ 284 nm are used to measure the water vapor concentration. The ratio of rotational Raman signals at 528 nm and 530 nm provides the measurement of atmospheric temperature [*Haris, 1995*]. Since the rotational states of all the molecules in the lower atmosphere are distributed according to the local temperature, the temperature can be directly measured by taking the ratio of the backscatter signals at two wavelengths in this distribution. Optical extinction is measured using the gradient of the measured molecular profile compared with that expected for the density gradient [*O'Brien et al, 1996*]. Techniques to measure water vapor and ozone will be discussed in Sections 3.2.4 and 3.2.5 respectively. The measurement capabilities of the LAPS instrument using Raman scatter techniques are summarized in Table 3-4 .

Table 3-4: LAPS measurement capabilities using Raman scatter techniques [*Esposito, 1999*].

Property	**Measurement**	**Altitude (km)**	**Time Resolution**
Water Vapor	660/607 Raman 295/284 Raman	Surface to 5 Surface to 3	Night - 1 min. Day/Night - 1 min.
Temperature	528/530 Rotational Raman	Surface to 5	Night - 30 min.
Optical Extinction - 530 nm	530 nm Rotational Raman	Surface to 5	Night 10 to 30 min.
Optical Extinction - 607 nm	607 nm Vibrational Raman	Surface to 5	Night 10 to 30 min.
Optical Extinction - 284 nm	284 nm Vibrational Raman	Surface to 3	Day/Night 30 min.
Ozone	277/285 Raman/DIAL	Surface to 2 - 3	Day/Night 30 min.

3.2.2 Lidar Equation

Measurements using the LAPS instrument provide profiles of water vapor, ozone, and optical extinction from the vibrational Raman scatter signals, while rotational Raman scatter signals are used to provide temperature profiles. The raw photon counts obtained from the backscatter of the laser radiation provide us with information about the concentrations of N_2, O_2, and H_2O at different altitudes. Since LAPS utilizes the backscatter of the laser beam, the form of the lidar equation is fairly simple, but the interpretation of the lidar signal may be complicated by geometrical considerations that include the degree of overlap between the laser beam and the field of view of the receiver optics, as well as the details of the telescope. Most of these concerns were minimized for the LAPS instrument through the choices made during the design. The reader can refer to

Measures (1984) for the derivation of the scattering lidar equation, which is described by the power of the signal received by a monostatic lidar denoted by $P(\lambda_R, z)$, given by :

$$P(\lambda_R, z) = P_T(\lambda_T)\xi_T(\lambda_T)\xi_R(\lambda_R)\frac{c\tau}{2}\frac{A}{z^2}\beta(\lambda_T, \lambda_R)\exp\left[-\int_0^z [\alpha(\lambda_T, z') + \alpha(\lambda_R, z')]dz'\right] \qquad [3.1]$$

where,

z	is the altitude of the volume element from which the return signal is scattered [m],
λ_T	is the wavelength of the laser light transmitted [m],
λ_R	is the wavelength of the signal received [m],
$P_T(\lambda_T)$	is the power transmitted at wavelength λ_T [W],
$\xi_T(\lambda_T)$	is the net optical efficiency at wavelength λ_T of all transmitting elements [unitless],
$\xi_R(\lambda_R)$	is the net optical efficiency at wavelength λ_R of all receiving elements [unitless],
c	is the speed of light in air [m s^{-1}],
τ	is the bin duration [s],
A	is the area of the receiving telescope [m^2],
$\beta(\lambda_T, \lambda_R)$	is the backscatter cross section [m^{-1}] of the volume element for the laser wavelength λ_T at Raman shifted wavelength λ_R [m^{-1}],
$\alpha(\lambda, z')$	is the extinction coefficient at wavelength λ at range z' [m^{-1}].

Using Eq. 3.1 and the fact that most of the Raman measurements are based upon ratios of signals of photon counts, we can obtain the vertical profiles of the atmospheric properties. It should be noted that return signals for the LAPS system using Eq. 3.1, $P_T(\lambda_T)$ are the time-averaged values for transmitted power at wavelength, λ_T. It becomes apparent from the examination of the lidar equation that the Raman scattering techniques, which use the ratio of the signals at two wavelengths, greatly simplifies the measurement of the various parameters. Most of the terms in the equation cancel out in the ratio, so specific details of the transmitter and the receiver are not required to obtain quantitative measurements. In the above equation $\xi_R(\lambda_R)$ is commonly known as the geometrical form factor and is critically dependent upon the details of the receiver optics. The analysis of the near field data (<800 m) is also important, because overfilling of the detector causes the effective profile of the received signal to be distorted [*Mulik, et. al., 2000*]. This signal distortion can be corrected by normalizing the detected signal to the actual received signal calculated using the geometry of the optics.

3.2.3 Optical Extinction Measurement

Optical extinction, which is a measure of the total attenuation of a laser beam due to scattering and absorption in the atmosphere, is obtained directly from the slope of the measured molecular profiles of N_2 and O_2 compared to the expected hydrostatic gradient. The LAPS instrument measures the optical extinction profiles from the gradients in each of the measured molecular profiles, at 607 nm, 530 nm and 284 nm. The 284nm and 607nm profiles are derived from the Raman shift of nitrogen scattering from the 2nd and 4th harmonics of the Nd:YAG laser respectively, and the 530nm wavelength is from the rotational Raman scattering of the 2nd harmonic laser beam. For these wavelengths the extinction is mainly due to optical scattering by aerosols, including airborne particulate matter. The extinction coefficient can be derived directly from the Raman lidar equation as described in Measures (1984). The Raman lidar equation, which describes the power of the signal received by a monostatic lidar, given by Eq. 3.1.can be simplified to,

$$P(\lambda_R, z) = \frac{K}{z^2}\beta(\lambda_T, \lambda_R)\exp\left[-\int_0^z [\alpha(\lambda_T, z') + \alpha(\lambda_R, z')]dz'\right], \qquad [3.2]$$

where, the system coefficient K includes all of the system constants which are range independent. Rearranging terms in the above equation, the Raman lidar equation can be expressed as

$$\exp\left[\int_0^z [\alpha(\lambda_{T,} z') + \alpha(\lambda_{R,} z')]dz'\right] = \frac{K}{z^2}\frac{\beta(\lambda_{T,} \lambda_R)}{P(\lambda_R, z)} \ . \qquad [3.3]$$

Taking the log of both sides of Eq. [3.5], the Raman lidar equation becomes

$$\int_0^z [\alpha(\lambda_{T,} z') + \alpha(\lambda_{R,} z')]dz' = \ln K + \ln\left[\frac{\beta(\lambda_{T,} \lambda_R)}{z^2 P(\lambda_R, z)}\right] \ . \qquad [3.4]$$

Differentiating the above equation with respect to z, we obtain

$$\alpha(\lambda_{T,} z') + \alpha(\lambda_{R,} z') = \frac{d}{dz}\left[\ln\left[\frac{\beta(\lambda_{T,} \lambda_R)}{z^2 P(\lambda_R, z)}\right]\right] \quad , \qquad [3.5]$$

The backscatter coefficient $\beta(\lambda_T,\lambda_R)$ can be shown to be

$$\beta(\lambda_T, \lambda_R, z) = N(z)\left\{\frac{d\sigma(\lambda_T, \lambda_R, \pi)}{d\Omega}\right\}, \qquad [3.6]$$

where $N(z)$ represents the number density of the molecules, and $\left\{\frac{d\sigma(\lambda_T, \lambda_R, \pi)}{d\Omega}\right\}$ is the differential Raman backscatter cross section of the vibrational/rotational Raman shift at wavelength λ_R. Since the number density of nitrogen is a well-known fraction of the atmospheric molecules, it can be used to represent the number density of all the molecules in the atmosphere. The differential form of $\ln\beta(\lambda_T,\lambda_R)$ is

$$\frac{d}{dz}\ln\beta(\lambda_T, \lambda_R, z) = \frac{d}{dz}\left[\ln N(z) + \ln\left\{\frac{d\sigma(\lambda_T, \lambda_R, \pi)}{d\Omega}\right\}\right] \qquad [3.7]$$

$$\frac{d}{dz}\ln\beta(\lambda_T, \lambda_R, z) = \frac{d}{dz}\ln N(z) \qquad [3.8]$$

The extinction coefficients in Eq. [3.5] can be written as

$$\begin{aligned}&\alpha(\lambda_T, z)+\alpha(\lambda_R, z)= \\ &\alpha_{\lambda_T}^{mol-sca}(z)+\alpha_{\lambda_T}^{aer-sca}(z)+\alpha_{\lambda_R}^{mol-sca}(z)+\alpha_{\lambda_R}^{aer-sca}(z)+\alpha_{\lambda_T}^{abs}(z)+\alpha_{\lambda_R}^{abs}(z)\end{aligned} \qquad [3.9]$$

where $\alpha_{\lambda}^{mol-sca}(z)$ and $\alpha_{\lambda}^{aer-sca}(z)$ are the extinction coefficients due to molecular and aerosol scattering at the transmit and receive wavelengths, and α_{λ}^{abs} are the molecular and aerosol extinction coefficients due to optical absorption. Both the transmitted and the received wavelengths must be considered since the different wavelengths may experience different scattering and absorption along the path. The molecular scattering contribution to the extinction can be easily calculated from temperature profile measurements or models. Normally the temperature profile is obtained from the LAPS lidar rotational Raman signals. The selected visible wavelengths do not correspond to any significant molecular absorption features in the atmosphere. However, the additional absorption at ultraviolet wavelengths is due to ozone and can be used to calculate tropospheric ozone density [*Esposito, 1999, Mulik 2000*]. The extinction at visible wavelengths is primarily due to aerosol scatter and molecular scatter contributions. The aerosol extinction coefficient at the visible wavelengths can be expressed by rewriting Eq. [3.5] as

$$\alpha_{\lambda_R}^{aer} = \frac{\dfrac{d}{dz}\left[\ln \dfrac{N(z)}{P(z)z^2}\right] - \alpha_{\lambda_T}^{mol}(z) - \alpha_{\lambda_R}^{mol}(z)}{1+\dfrac{\lambda_T}{\lambda_R}} \quad . \qquad [3.10]$$

The wavelength dependence of particle extinction coefficients is λ^{-q}, where $0.7 < q < 1.9$ for tropospheric particles. Here $q = 1$, which has been suggested to be a reasonable assumption for tropospheric particles [*Ansmann et al., 1990*]. At the UV wavelengths, between 200 nm and 300 nm, the absorption due to ozone is significant. Since the cross-section for the Hartley band of ozone is well known (better than 1%), and the ozone concentration is measured from the departure of the measured O_2/N_2 ratio from the expected constant value in the lower atmosphere, we can determine the ultraviolet extinction due to aerosols [*Li, 2004*]. For the UV wavelengths the extinction equation includes the compensation for the ozone absorption as,

$$\alpha_{\lambda_R}{}^{aer} = \frac{\frac{d}{dz}\left[\ln \frac{N(z)}{P(z)z^2}\right] - \alpha_{\lambda_T}{}^{mol}(z) - \alpha_{\lambda_R}{}^{mol}(z) - \alpha_{\lambda_T}{}^{Abs}(z) - \alpha_{\lambda_R}{}^{Abs}(z)}{1 + \frac{\lambda_T}{\lambda_R}} \quad . \qquad [3.11]$$

3.2.4 Water Vapor Measurement Technique

Water vapor concentration is a fundamental property of the atmosphere and provides us with information about the most important properties of our environment. Water vapor is a primary factor in the distribution of heat energy over the globe because of the latent heat taken up and given off during phase changes. Water vapor is also an excellent tracer of the local atmospheric dynamics. The largest concentration of atmospheric water vapor is found in the lower atmosphere and its concentration decreases with increasing altitude. The earliest Raman lidar measurements to yield the spatial distribution of water vapor in the atmosphere were performed by Melfi et al. (1969) and Cooney (1970). They used a frequency-doubled Q-switch ruby laser and normalized their water vapor return using the nitrogen vibrational Raman return. The LAPS instrument measures the water vapor mixing ratio by taking the ratio of the signals from the 1st Stokes vibrational Raman shifts for water vapor and nitrogen. Profiles of water vapor can be obtained during the day (295/284) and the night (660/607) with the ultraviolet and visible laser wavelengths [*Rajan et al., 1995; Balsiger et al., 1996*]. LAPS has the capability of obtaining day time measurements by operating in the ‘solar blind’ spectral interval, between 230 and 300 nm, where stratospheric ozone absorbs the incoming radiation and limits the strong sky background radiance. The water vapor mixing ratio is expressed by taking the ratio of its number density to the number density of ambient air and multiplying by a calibration constant. The equation to obtain vertical profiles of water vapor at visible wavelengths is,

$$\mathrm{W(z)} = \mathrm{K_{cal}} \frac{\mathrm{S_{H2O}(z)}}{\mathrm{S_{N2}(z)}} \tag{3.12}$$

where,

S_{H2O} is the received signal from the vibrational Raman shift of H_2O at 660 nm,
S_{N2} is the received signal from the vibrational Raman shift of N_2 at 607 nm,
K_{cal} is a calibration constant.

The calibration constant, K_{cal}, may be obtained by fitting the ratio of the return signals of H_2O and N_2 with the data obtained from a radiosonde balloon for water vapor profile at the same time. Since we are taking the ratio of the two signals and the numerator and the denominator have the same transmit wavelength most of the terms in the lidar equation cancel providing a simpler equation [*Esposito, 1999*].

$$\frac{P_{H20}(z)}{P_{N2}(z)} = \frac{\xi_R(\lambda_{H2O})}{\xi_R(\lambda_{N2})} \frac{\beta(\lambda_T, \lambda_{H2O}, z)}{\beta(\lambda_T, \lambda_{N2}, z)} \frac{\exp\left[-\int_0^z [\alpha(\lambda_{H2O}, z')]dz'\right]}{\exp\left[-\int_0^z [\alpha(\lambda_{N2}, z')]dz'\right]} \tag{3.13}$$

The extinction coefficient is assumed to equal the sum of the scattering due to molecules, scattering due to aerosols along the path, and the absorption by ozone. A constant, K_{system}, is introduced to simplify the calculation [*Esposito, 1999*].

$$\frac{P_{H_20}(z)}{P_{N2}(z)} = k_{system} \frac{\exp\left[-\int_0^z [\alpha_m(\lambda_{H2O}, z') + \alpha_a(\lambda_{H2O}, z') + \alpha_{O3}(\lambda_{H2O}, z')]dz'\right]}{\exp\left[-\int_0^z [\alpha_m(\lambda_{N2}, z') + \alpha_a(\lambda_{N2}, z') + \alpha_{O3}(\lambda_{N2}, z')]dz'\right]} \tag{3.14}$$

where,

$\alpha_m(\lambda_x,z)$ is the attenuation due to molecular scattering at wavelength λ_x,

$\alpha_a(\lambda_x,z)$ is the attenuation due to absorption and scattering of aerosols at wavelength λ_x,

$\alpha_{O3}(\lambda_x,z)$ is the attenuation due to ozone absorption at wavelength λ_x.

Since the differences between the absorption and scattering due to aerosols at the two wavelengths are small, they can be neglected or treated as having a λ^{-1} dependence as an approximation,

$$\frac{P_{H20}(z)}{P_{N2}(z)} = k_{system} * \exp\left[-\int_0^z [\alpha_m(\lambda_{H2O}, z') - \alpha_m(\lambda_{N2}, z') + \alpha_{O3}(\lambda_{H2O}, z') - \alpha_{O3}(\lambda_{N2}, z')]dz' \right] \qquad [3.15]$$

Equation 2.5 has to be corrected for molecular scattering and ozone absorption at the Raman shifted wavelengths in order to obtain an accurate water vapor measurement. The molecular scattering at each wavelength is given as [*Esposito, 1999*],

$$\sigma_x K(z) = \int_0^z \alpha_m(\lambda_x, z')dz' = \sigma_x \int_0^z \left[NH\left(1 - \exp\left(\frac{-z'}{H}\right)\right) dz' \right] \qquad [3.16]$$

$$H = \frac{kT(z)}{mg} \qquad [3.17]$$

$$T(z) = To + \gamma z \qquad [3.18]$$

where,

N is the number density at ground level,

k is Boltzman's constant (1.380658 x 10^{-34}), m is average mass per molecule,

g is gravitational acceleration,

T_o is the surface temperature,

γ is the lapse rate of -6.5 K/km (valid only for the lower 10 km),

σ_x is the Rayleigh scattering cross-section at the x^{th} Raman shifted wavelength.

The molecular component of the signal loss can thus be removed from the data based upon the molecular scattering cross sections and the fractional abundance of N_2 and O_2,

$$W(z) = K * \frac{S_{H2O}(Z)}{S_{N2}(Z)} \exp(\sigma_{H2O} - \sigma_{N2}) K(z) \ . \qquad [3.19]$$

The water vapor mixing ratio calculated from the 1st Stokes vibrational Raman shift of the visible transmitted beam (532 nm) does not need to be corrected for ozone absorption and hence the above equation, corrected for molecular scattering is used.

Since LAPS obtains profiles of water vapor in the daytime by using the *solar-blind* region, some of the transmitted radiation is absorbed by tropospheric ozone and hence correction for ozone absorption is necessary. By measuring the Raman backscatter return of O_2 at 277 nm and N_2 at 284 nm, it is possible to obtain the total ozone column density at low altitudes. Applying the Beer-Lambert law to this ratio of O_2 and N_2 leads to the following expression [*Renault et al, 1980*] for ozone column density,

$$\frac{S_{O2}}{S_{N2}} = \frac{O_2}{N_2} \exp(-C(z)), \qquad [3.20]$$

where C(z) is the optical depth for ozone and is,

$$C(z) = (\sigma_{O_2} - \sigma_{N_2})\int_0^Z O_3 dz \quad = \ln\left(\frac{S_{O2}}{S_{N2}}\right). \qquad [3.21]$$

The UV water vapor mixing ratio, which has been corrected for ozone absorption, can be expressed in the form,

$$w(z) = K\frac{S_{H2O}(z)}{S_{N2}(z)}\left(\frac{S_{O2}(z)}{S_{N2}(z)}\right)^{\frac{\sigma_{H2O}-\sigma_{N2}}{\sigma_{N2}-\sigma_{O2}}}. \qquad [3.22]$$

3.2.5 Ozone Measurement Technique

Ozone measurements are obtained by a DIAL (Differential Absorption Lidar) analysis of the Raman shifts of N_2 (284 nm) and O_2 (277nm), which occur on the steep side of the Hartley absorption band of ozone. Taking the ratio of the return signal from the Stokes Raman shifted signal from nitrogen molecules in the scattering volume, the lidar equation reduces to [*Balsiger et al*, *1996*],

$$\frac{P_{O2}(z)}{P_{N2}(z)} = \frac{\xi_R(\lambda_{O2})}{\xi_R(\lambda_{N2})}\,\frac{\beta(\lambda_T, \lambda_{O2}, z)}{\beta(\lambda_L, \lambda_{N2}, z)}\,\frac{\exp\left[-\int_0^z [\alpha(\lambda_{O2}, z')]dz'\right]}{\exp\left[-\int_0^z [\alpha(\lambda_{N2}, z')]dz'\right]} \qquad [3.23]$$

Choosing a system constant, ksystem,

$$k_{system} = \frac{\xi_R(\lambda_{O2})}{\xi_R(\lambda_{N2})}\,\frac{\beta(\lambda_T, \lambda_{O2}, z)}{\beta(\lambda_T, \lambda_{N2}, z)} = \frac{\xi_R(\lambda_{O2})}{\xi_R(\lambda_{N2})}\,\frac{\sigma_{O2}}{\sigma_{N2}}\,\frac{[O2]}{[N2]} \qquad [3.24]$$

where,

σ_x is the Raman cross-section of x at the laser wavelength,

[X] is the number density concentration of x in the atmosphere.

simplifies the above equation to [*Esposito, 1999*],

$$\frac{P_{O2}(z)}{P_{N2}(z)} = k_{system} * \exp\left[-\int_0^z [\alpha_m(\lambda_{O2}, z') - \alpha_m(\lambda_{N2}, z')]dz'\right] \exp\left[-\int_0^z [\alpha_{O3}(\lambda_{O2}, z') - \alpha_{O3}(\lambda_{N2}, z')]dz'\right] \quad [3.25]$$

where,

$\alpha_m(\lambda_x, z')$ is the attenuation due to molecular scattering at wavelength λ_x,

$\alpha_{O3}(\lambda_x, z')$ is the attenuation due to ozone absorption at wavelength λ_x.

The number density of ozone in a scattering volume is calculated by differentiating the integrated ozone number density corrected for molecular scattering [Esposito, 1999] and is,

$$[O_3(z)] = \frac{d}{dz}\left[\ln\left(\frac{P_{O2}(z)}{P_{N2}(z)}\frac{1}{k_{System}}\right) * \frac{1}{(\sigma_{N2} - \sigma_{O2})} + \frac{(\sigma_{O2} - \sigma_{N2})}{(\sigma_{N2} - \sigma_{O2})}K(z)\right] \quad [3.26]$$

From the above equation it is possible to obtain the ozone concentration at altitudes above the first bin, i.e., approximately 113 m above ground level. To incorporate ground level measurements into the lidar profiles, surface measurements are used. The reader is referred to Mulik (2000) for a detailed explanation of this procedure for completing the atmospheric profile of ozone to the ground. The primary errors in the measurement are due to the photon count limitation. A higher power laser transmitter and/or a larger telescope receiver extend the useful altitude range. The only other factor influencing the measurement is the ozone absorption cross-section accuracy and that is known to better than 1% from laboratory measurements.

3.3 Campaigns

The data used in this thesis were taken from an extensive dataset that was collected during several campaigns at different locations. This dataset contains a wealth of information that could be used for future studies of the lower atmosphere, air pollution, aerosol distributions, and cloud properties. The measurements in this dataset were obtained through the dedicated efforts of numerous researchers from different schools and agencies. This section provides the reader with a brief history of the various campaigns.

3.3.1 Testing onboard the USNS Sumner (1996)

The LAPS instrument was initially prepared as a prototype instrument to provide real time data of meteorological properties and refractivity. It was tested successfully onboard the USNS Sumner during the fall of 1996. This campaign, in addition to testing the LAPS instrument, also provided a rich dataset on the properties in the lower marine boundary layer. The LAPS instrument took measurements of water vapor, temperature, extinction and ozone. Rawinsonde balloons were released during several time periods, coincident with the lidar measurements, and were used a comparison to the lidar data. Testing of the instrument was carried out as survey operations were conducted in the Gulf of Mexico off the Atlantic coast of the United States. The lidar was able to obtain data for an average of 10 hours each day during this period and was run continuously for extended periods of one to several days on several occasions Measurements were made during the day and night, and in all weather conditions. Several measurements were made during cloudy conditions, with data available in-between and through clouds with low optical thicknesses. The capability to obtain high quality RF ducting prediction data with real-time data products was shown [*Philbrick, 1996*]. This dataset also contains several cases that show the convective uptake of water into the base of growing cumulus clouds.

3.3.2 Southern California Ozone Study (SCOS – 1997)

During the period between 24 August and 18 September 1997, researchers from Penn State University participated in the Southern California Ozone Study (SCOS) at the Hesperia, CA site. The study was co-sponsored by the California Air Resources Board, the Mojave Desert Air Quality Management District (MDAQMD), the USEPA National

Exposure and Research Laboratory, and the US Marine Corp at 29 Palms. The goal of the study was to develop databases that support detailed photochemical modeling and analysis to better understand the processes involved in the formation of high ozone concentrations in the South Coast Air Basin and across the southern California regions [*CARB, 1999*]. The Raman lidar was used to measure the atmospheric properties in order to investigate the processes leading to ozone production in the Los Angeles basin and subsequent transport into the high desert that lies to the east. The site was located north of the west end of the Los Angeles basin at the edge of the high desert plateau. The Raman lidar obtained profiles of water vapor, temperature, and ozone during both day and night. The dataset also includes particulate matter data, radiosonde measurements, and wind and temperature measurements using a RASS instrument. The results obtained during the SCOS97 program have shown processes involved in the formation of high ozone concentrations in the southern California region features that are important in understanding the meteorological control of air pollution and air quality [*SCOS Report*].

3.3.3 Measurements during the ARM Program – Barrow, Alaska (1998)

The Atmospheric Radiation Measurements (ARM) Program works towards understanding the global scale environmental change issues associated with the national policies on use of fuels that supply energy for industrial and individual use. The ARM program has measurement sites that have been established at Norman, Oklahoma, on a Pacific Ocean Island, and at Barrow, Alaska. These sites have been used to gather data to provide the basic measurements which are used to formulate our national policy on fuel use. The arctic site has been important in providing data on water vapor, arctic haze and tropospheric ozone. The LAPS instrument was used to obtain data at the ARM North-slope site in March and May of 1998. Key parameters of the atmosphere, such as water vapor, ozone, temperature, and optical extinction, were measured using the Raman lidar. Data were collected for eight days in March and thirteen days in May during the NASA FIRE program. This campaign resulted in the collection of an excellent dataset of simultaneous measurements of cloud properties and atmospheric thermodynamic properties. The data shows the buildup of air pollution exhibited by the phenomena of arctic haze in the high latitude atmosphere. The results obtained were used to study the characteristics of the arctic atmosphere and to make a statement about the value of the lidar technique in making high latitude measurements of the atmosphere [*Philbrick et al., 2000*].

3.3.4 North-East Oxidant and Particle Study (NE-OPS)

The EPA-sponsored NEOPS campaigns (1998, 1999 and 2001), and Pennsylvania DEP-sponsored NEOPS (2002) campaign were intensive summer field measurements conducted at a field site located just North of Philadelphia near the Baxter Water treatment plant (Site Location - 40^o 02.14' N, 75^o 00.28' W). The 1998 program was intended to prepare the field site and to evaluate the instrument techniques, which were used during the investigations. The primary objectives of the NE-OPS campaigns were to investigate the urban polluted atmosphere to find the relationships among conditions leading to high ozone concentrations and increased levels of fine particles, determine the contributions from local and distant sources, and to examine the role that meteorological properties play in the build-up and distribution of pollutant concentrations. The program included the instruments that are most useful for describing the evolution of air pollution events and examining the controlling factors of local meteorology on the particulate matter and chemical species distribution in the lower atmosphere. The measurements overlapped the activity of the three PM (Particulate Matter) Supersites in the northeast region, Baltimore, Pittsburgh and New York. The major instruments included remote sensing radar and lidar for vertical profiling of the meteorological and air quality properties, insitu measurements of meteorology and ozone from surface to 300 m using instrumented tethered balloons, a suite of surface based instruments for measuring the concentrations of key chemical species and particulate physical/chemical properties, and a few profiles from aircraft measurements. Also, minor/toxic species were measured using filter samples, which were analyzed with high-resolution GC/MS laboratory techniques. The data set comes from a collaboration of Penn State University, Millersville University, Drexel University, University of Maryland, Harvard School of Public Health, Brigham Young University, Brookhaven National Laboratory, Carnegie Mellon University, Texas Tech, Philadelphia Air Management Services, the Pacific Northwest National Lab, and the Argonne National Laboratory. The NE-OPS campaigns have improved our capability to forecast pollution events in the mid-Atlantic region, by providing an improved understanding of the influence of the local and regional dynamics and transport on the conditions that lead to the generation of air pollution episodes. Detailed information on the NE-OPS campaigns can be found in the NEOPS reports [*Philbrick et al., 2002; Philbrick et al., 2003*]. A list of the participants and measurements during each of the NEOPS campaigns can be found in appendix D.

3.3.5 Philadelphia 2005 Winter Study

This study was sponsored by the City of Philadelphia Air Management Services Laboratory and its main objective was to use remote sensing and in-situ measuring instruments to investigate air quality issues during the winter season 2004-2005 at the Baxter Water Treatment Plant in northeast Philadelphia. Data was collected using a Doppler wind profiling radar, Radio Acoustic Sounding System (RASS), 10-meter instrumented meteorological tower, ozone analyzer, DustTrak aerosol monitor, and three-wavelength nephelometer, which were operated during the winter months from January to March. The dataset, which documents the kinematic and thermodynamic structure of the lower atmosphere, is used with other simultaneous measurements to investigate the dynamical processes controlling the PM concentration and describe winter air quality. The location of the site enhances the importance of the study because it is centered in the air pollution corridor in the northeast region, and also because it has been the location of several previous air pollution studies [*Philbrick et al., 2005*].

Chapter 4

Data Analysis and Results

Lidar measurements, which can determine the extinction coefficient profile as a function of height, are of great utility in determining aerosol properties because aerosol physical characteristics such as number density, size, or mass concentration are more directly related to extinction coefficient than to backscatter cross-section. The extinction coefficient obtained is also the fundamental parameter on which radiative transfer models of the atmosphere may be based [*Spinhirne et al., 1980*], and provides us with important information for climate prediction. The measurements obtained during different periods by the PSU LAPS Raman lidar have provided an extensive dataset on water vapor, extinction, ozone, and temperature data, which are used to characterize aerosol distributions and cloud properties. The ratios of the extinction coefficients at the different wavelengths contain important size information for accumulation-mode particles. The change in the size of the cloud particles during the different stages can also be observed in the multi-wavelength aerosol extinction. My results show the importance of the multi-wavelength measurements of extinction ratios, along with support of the interpretations from theoretical simulations of extinction ratios calculated using Mie scattering, for understanding the effects of particle size variations. The wavelength variation in the extinction profiles is also used, along with simultaneous measurements of water vapor profiles, to investigate the formation and dissipation of cloud structures. The Raman lidar aerosol extinction provides us with a capability to determine the visibility, or visual range along a path through the atmosphere, and describes our ability to see distant objects depends upon the aerosol extinction along the path. I have selected a few sets of data to describe the characteristics of aerosols and clouds that have been investigated.

4.1 Extinction Ratio Analysis of Aerosol and Cloud Particle Size Variations

To examine variations of the extinction for different particle sizes and wavelengths we use extinction coefficient values calculated using Mie theory and measurements of extinction obtained from the LAPS lidar. The assumption of spherical particles enables us to use Mie calculations to obtain solutions, which otherwise would be extremely because aerosols may come in various shapes. However, in the high-humidity regions of the eastern U.S., the aerosol population is typically dominated by sulfate and acid based aerosols, which can be considered as spherical because of their hygroscopic nature. In the western U.S. irregular shapes associated with mineral dust are more prevalent. In most atmospheric situations aerosols are neither large enough nor small enough compared to the wavelength of optical radiation to be satisfactorily treated by simplifying approximations. In general, particles absorb as well as scatter radiation, and Mie developed solutions for the absorption, scattering and extinction cross sections as a function of the scattering angle for spherical particles. The function for the extinction efficiency factor, Q_{ext}, for spheres of refractive index n in air is derived using Mie theory, which describes the efficiency with which light is scattered as a function of the size parameter. Figure 4-1 shows the extinction efficiency calculated for the three wavelengths at which optical extinction values are obtained with the LAPS Raman lidar. The location of the peak of the function is seen to be directly proportional to the wavelength. Thus, shorter wavelengths tend to detect smaller particles and vice versa. The variations in the extinction values of the three wavelengths directly measured using the LAPS Raman lidar are located in the size range of condensation nuclei. Thus, these measurements can be used to provide important information regarding CCN size variations. Li (2004) analyzed the ratio of backscatter signals at different wavelengths, using Mie theory, to obtain information on particle size. Lidar backscatter signals, at 523 nm and 1046 nm, were used to investigate particle characteristics in artificial plumes of dust that were released into the atmosphere. The backscatter signal information was used along with particle size distributions to study particle settling rates of soil and dust particles suspended in the air by agricultural activities.

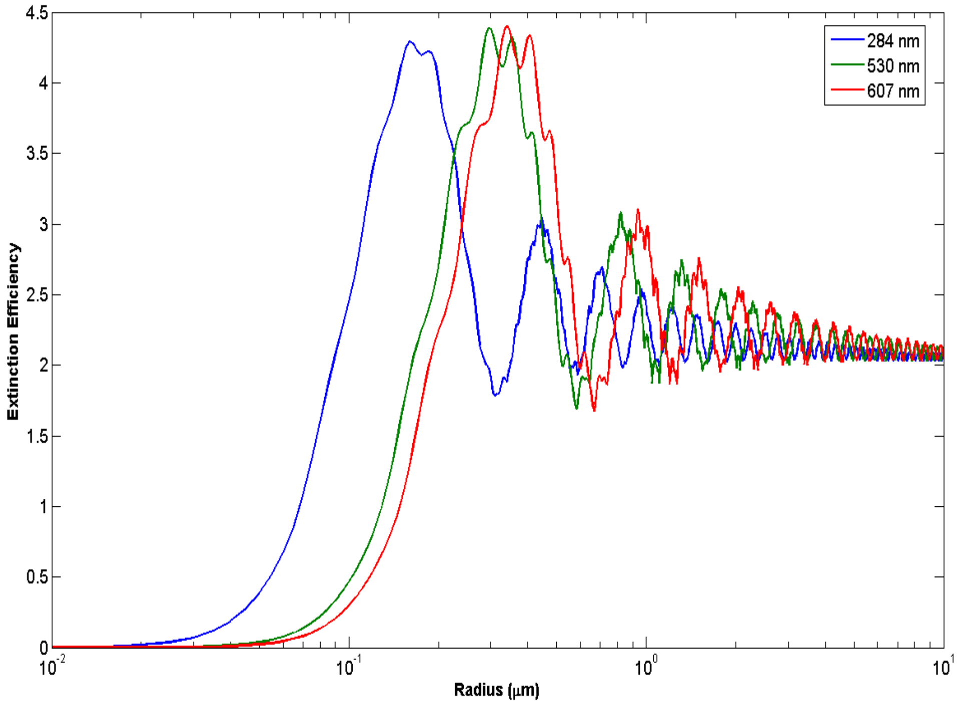

Figure 4-1: Extinction efficiency calculated using Mie theory for three wavelengths at which optical extinction values are obtained with the LAPS Raman lidar.

The LAPS lidar has a distinct advantage in being able to measure optical extinction at different wavelengths, and we use the extinction measurements to infer particle size variation by taking ratios of the extinction coefficients measured at the different wavelengths. Figure 4-2 shows a model calculation of the ratios of the extinction coefficients for wavelength ratios, 530 nm/284 nm and 607 nm/530 nm. The calculation was carried out using Mie theory assuming only spherical particles. We see that the ratios of the extinction coefficients provide us with information about variations in the size of particles. When the particle size is small compared to wavelength, the scattered intensity is inversely proportional to the fourth power of the wavelength, while the scatter cross-section increases as the sixth power of the particle radius. For accumulation mode particles, where the size range is between 0.05 μm and 1 μm, the ratios of the extinction coefficients are size dependent and structured as a function of size. For coarse mode particles the ratios lose their size dependence and approach unity (for optical wavelengths in the visible spectrum). In Figure 4-2, which shows the simulation of the ratios of the extinction values at the different wavelengths, we see that size variation information for particles in the accumulation mode can be inferred as the ratio of the extinction efficiencies increases with increasing particle radius. The LAPS Raman lidar has the capability of measuring through optically thick clouds, and we use this to our advantage to study particle size variations inside the boundary regions of low-density clouds.

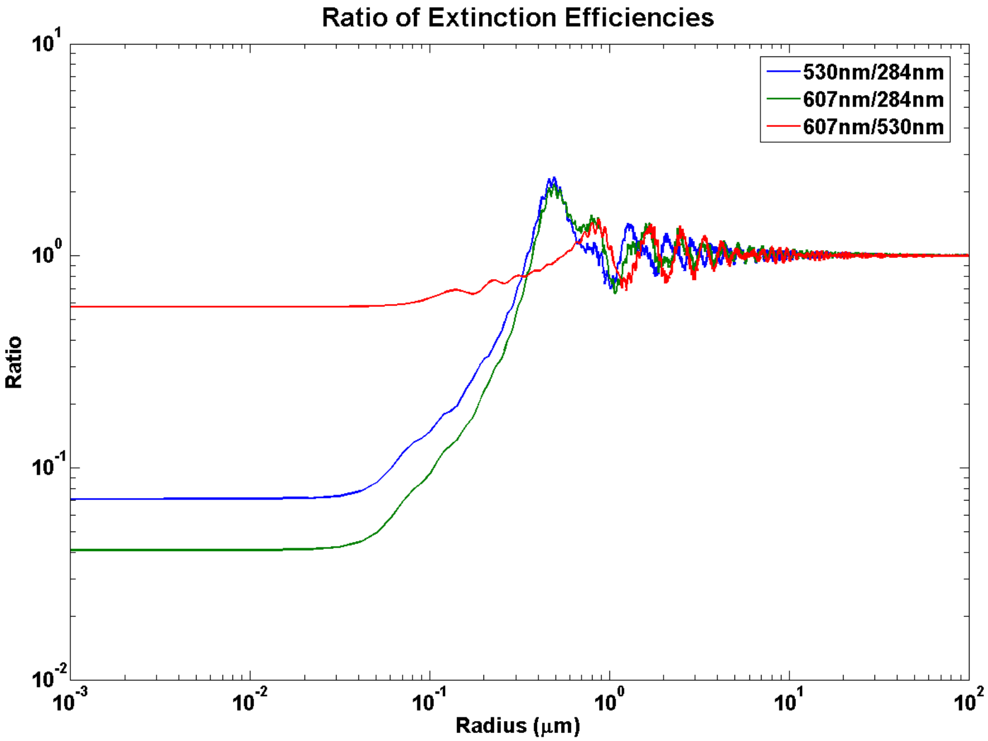

Figure 4-2: Ratios of extinction coefficients as a function of particle size calculated using Mie theory for three wavelengths at which optical extinction values are obtained with the LAPS Raman lidar.

The wavelengths typically used in lidars are most efficient in detecting particles from 0.1 μm to ~ 1 μm and this range corresponds to the size range of condensation nuclei particles; therefore we can derive important information regarding CCN size variation.

The particle distributions in the regions of formation and dissipation of clouds, and in fog regions are likely to be within this range of sizes.

Figure 4-3 shows cloud and haze distributions models constructed using the modified gamma distribution function. These models, whose numerical parameters were obtained from Deirmendjian (1969), represent some of the distributions commonly seen in haze, fog, and cloud layers. The general form of the four-parameter distributions is given by

$$n(r) = ar^{\alpha} \exp\left[-\frac{\alpha}{\gamma}\left(\frac{r}{r_c}\right)^{\gamma}\right], \quad 0 \leq \mathrm{r} < \infty \qquad [4.1]$$

where $n(r)$ is the volume concentration of droplets per unit radius as a function of the radius. The shape of each size distribution curve is determined by the three parameters α, γ and mode radius r_c. The size parameter α assumes only positive and integer values, and γ has to be positive and real. The parameter a normalizes the total number N of droplets per unit volume. One may construct a great variety of specific distributions based on the general form of the modified gamma distributions of Eq 4.1. Table 4-1 shows six basic size distribution models constructed by Deirmendjian (1969), to depict different cloud and haze distributions. The cumulus cloud distribution C.1 represents cumulus clouds of moderate thickness. The corona clouds model C.2 has the same mode radius as C.1 and are used to model clouds whose integrated angular scattering properties will indicate colored coronas of the right radius. The Mother of Pearl (MOP) model C.3 is typically used to models high-altitude clouds. The Haze M model was introduced to reproduce marine or costal types of distributions. By changing the size and the wavelength unit from microns to millimeters and by reducing N, the model can be used to fit to certain natural raindrop distributions [*Deirmendjian, 1969*]. The Haze H model also serves a double purpose. It can be used to represent high-level or stratospheric aerosol or dust layers composed of submicron particles. Changing the size and wavelength units to centimeters converts this model to a hailstone distribution. The Haze L models are adopted to represent continental type of aerosol distributions.

Table 4-1: Size distribution models, based on Deirmendjian (1969), to depict various cloud and haze distributions for N = 100 cm-3.

Distribution type	**a**	r_c	**α**	**γ**
Cumulus cloud, C.1	2.3730	4.0 μ	6	0.5
Corona cloud, C.2	$1.0851\text{x}10^{-2}$	4.0 μ	8	0.5
MOP cloud, C.3	5.5556	2.0 μ	8	1
Haze M	$5.3333\text{x}10^{4}$	0.05 μ	1	1
Haze L	$4.9757\text{x}10^{6}$	0.07 μ	2	3
Haze H	$4.0\text{x}10^{5}$	0.1 μ	2	3

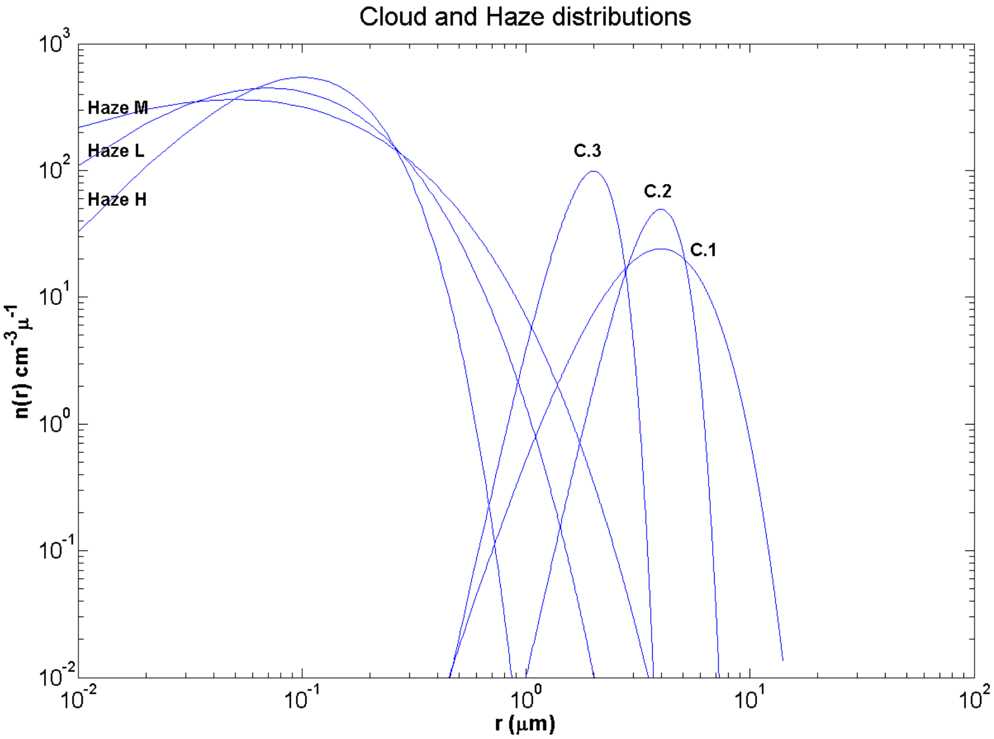

Figure 4-3: Haze and Cloud-type distributions constructed using the modified gamma distribution and based on parameters by Deirmendjian (1969).

By looking at the distributions in Figure 4-3, we see that the accumulation mode particles fall in the range where the transition occurs between haze and cloud layers. Thus by using the multi-wavelength extinction obtained from the Raman lidar we are able to observe CCN size changes as aerosols acquire additional water and increase in size to form clouds. Similarly, we are able to observe size changes as the cloud begins to dissipate. Figure 4-4 presents the model results for volume extinction coefficients for several atmospheric conditions calculated by Deirmendjian (1969). Rayleigh scattering intensity should be inversely proportional to the fourth power of the wavelength when the particle size is small compared to the wavelength. As the particle sizes increase, for example under haze conditions, the wavelength dependence of aerosol scattering becomes approximately inversely proportional to the wavelength, while scattering by large particles, for instance inside clouds, is almost independent of the wavelength.

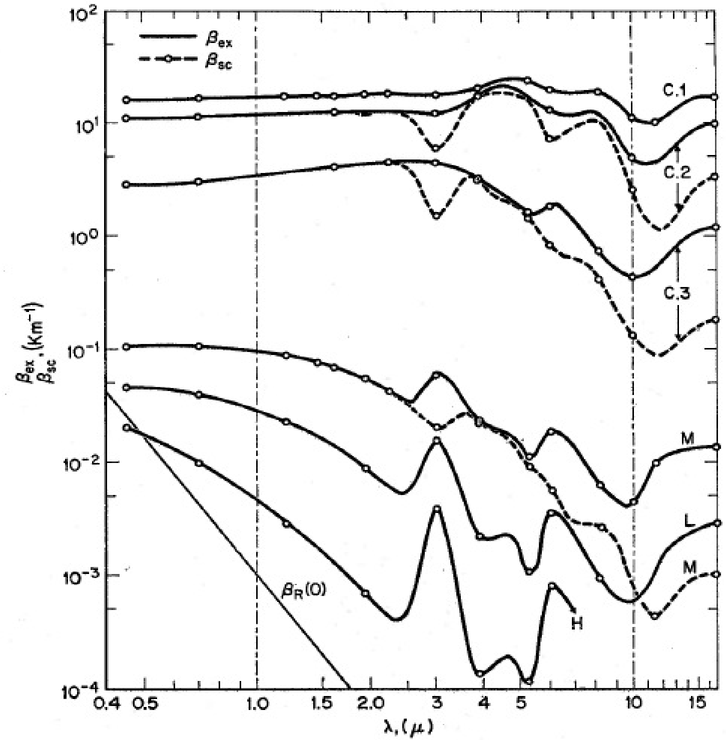

Figure 4-4: Volume extinction (solid line) and scattering (dashed line) coefficients for various distributions of water spheres calculated by Deirmendjian (1969).

This research effort is focused on examining the several datasets and developing a technique to observe size variations from the optical extinction measurements obtained at three different wavelengths by the LAPS Raman lidar, and infer the changes in the microphysical properties of the particles. Since the ratio of the extinction at the different wavelengths contains important size information for particles in the size range of the accumulation mode we can use the multi-wavelength extinction ratios to investigate particle size information. We are interested studying the accumulation mode particles because this size range corresponds to the size range for cloud condensation nuclei and the scatterers of this size exhibit the largest changes for the wavelengths of laser radiation available for the LAPS lidar.

Figure 4-5 shows an example of the optical extinction measurements made at the three wavelengths during the SCOS97 measurement program (Hesperia, CA), and relates them to the information in Figure 4-2 and Figure 4-4. The vertical profiles show the variation of extinction with altitude. The data obtained have been integrated over a 60 minute period and plotted as a function of altitude. By comparing these data with the model calculations we observe that a large number of aerosol particles (typical size on the order of 0.5 μm) seem to dominate in the lower atmosphere, from the surface near 1.2 km up to about 1.7 km. The UV and visible extinction coefficients imply the presence of accumulation mode particles with size distribution peaked near the middle wavelengths of visible light. At altitudes between 1.7 km and 4 km, the ultraviolet extinction is much greater than the visible extinction (approximately a factor of 4 or 5) and this suggests a distribution of smaller particles in this region (a ratio of a factor of 12 would imply that the particles are less than 50 nm in size), however the number density of the small particles must be very large to result in the high extinction values measured. At higher altitude, we also observe two layers with no significant wavelength dependence above 4.5 km (the extinction values being the same in the UV and visible wavelength) where the scattering is due to the large particles in a cloud. This example shows the features that follow closely with the model results by Deirmendjian (1969), for volume extinction coefficients of different particle sizes, where the wavelength dependence disappears, as the particle size increases to the size ranges typical of cloud particles.

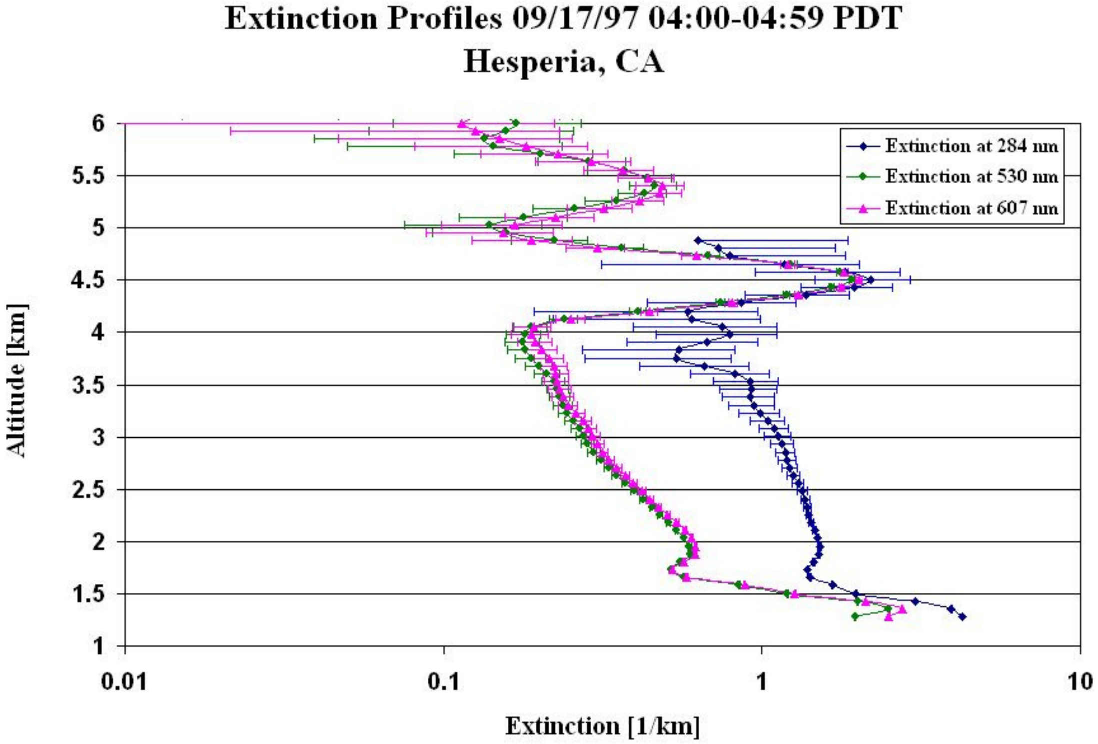

Figure 4-5: One-hour integrated vertical profiles of optical extinction at 284 nm, 530 nm and 607 nm on September 17, 1997, at Hesperia, CA (elevation – 976 m).

Cloud data obtained using the LAPS Raman lidar during the NARSTO-NEOPS campaign was analyzed using the extinction ratios at the UV and visible wavelengths to study particle size variations. Figure 4-6 show the time sequence plots of extinction at the ultraviolet and visible wavelengths on the night of 16 August, 1999 at the Philadelphia site during the NARSTO-NEOPS campaign. Figure 4-7 shows simultaneous measurements of the water vapor mixing ratio measured using the Raman lidar. During this time period we observe that several aerosol cloud layers advect through the laser beam and our analysis of the ratio of the extinction coefficient of 530/284 shows changes in particle size relative to variations in regions both inside, and surrounding the cloud layers. We also observe high water vapor concentrations in and around the cloud regions in Figure 4-7.

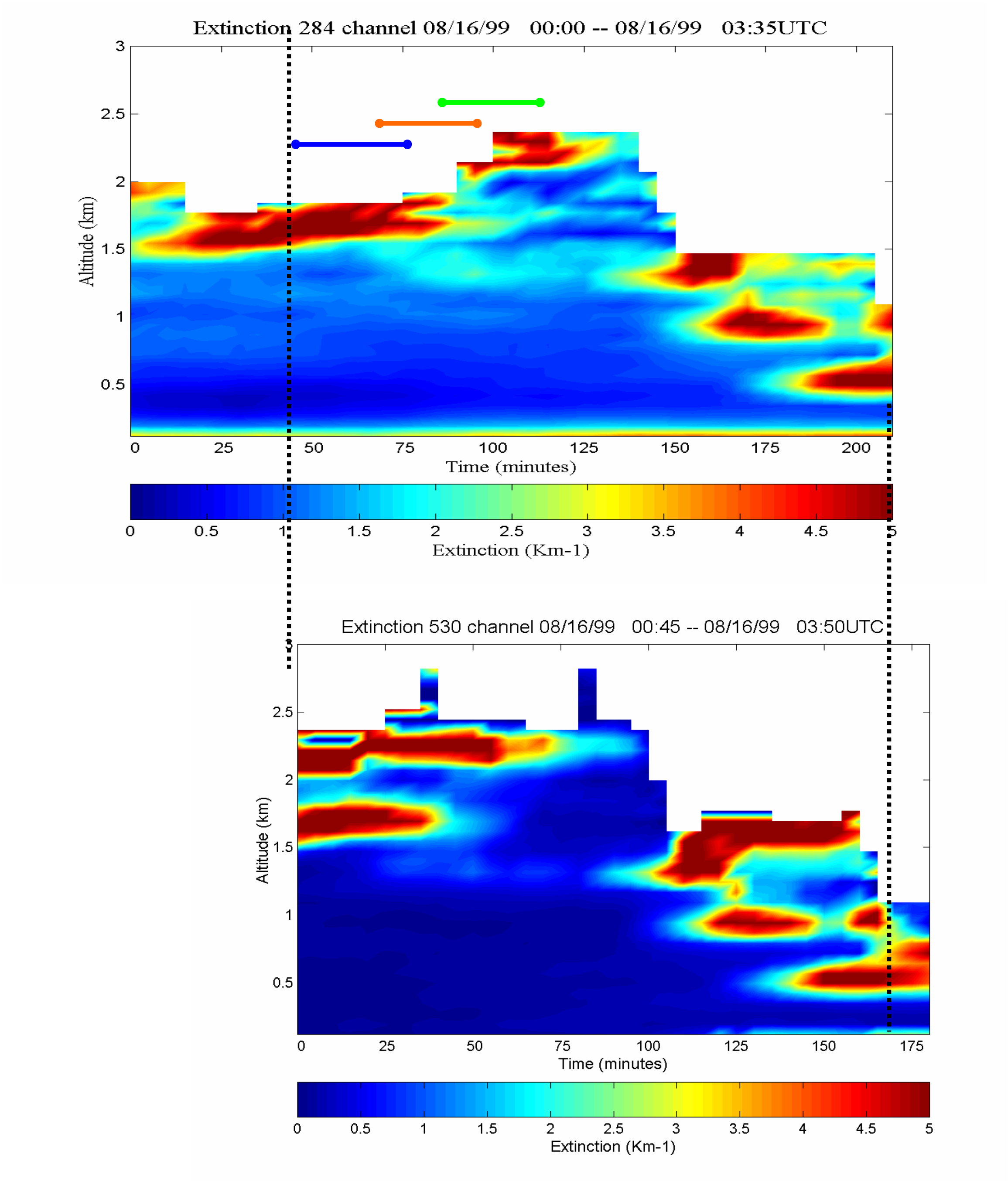

Figure 4-6: Time sequence plot of extinction on August 16, 1999 at (a) 284nm (b) 530nm (the visible wavelength is only available after darkness of the sky).

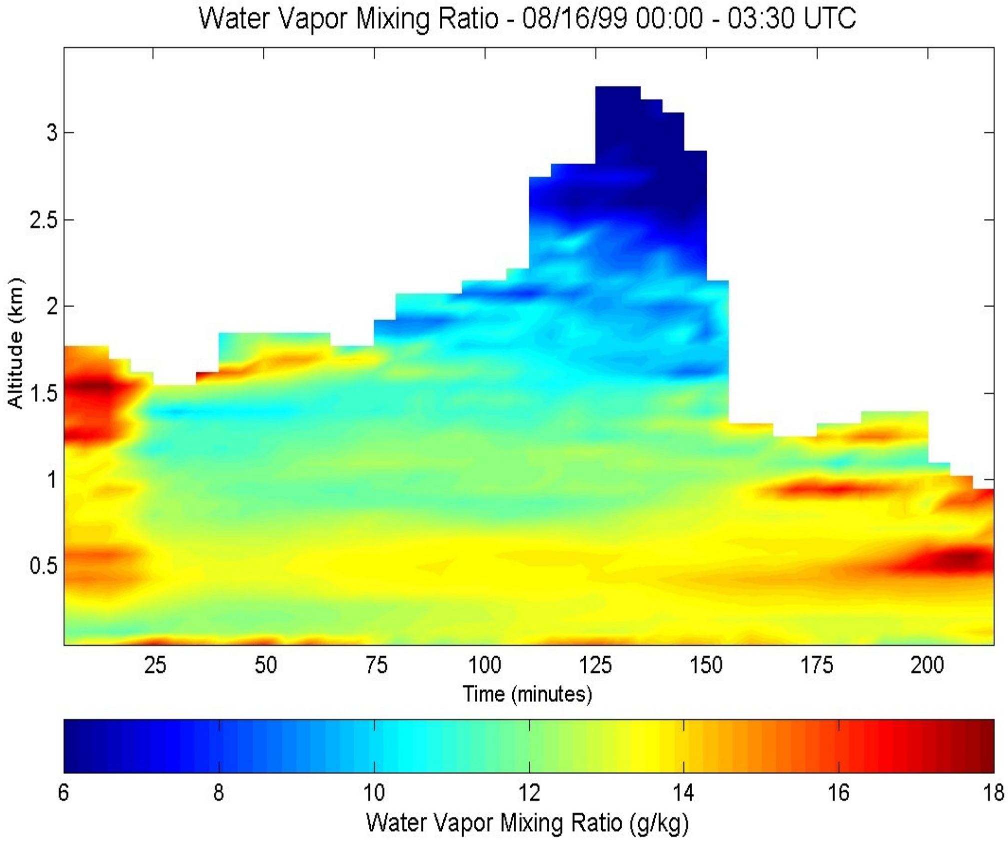

Figure 4-7: Time sequence plot of water vapor mixing ratio on August 16, 1999.

A time sequence of the ratio of the extinction coefficients, as the clouds pass though the laser beam, is shown in Figure 4-8. Vertical profiles of the extinction ratio at selected intervals during the time sequence, each integrated for a half hour periods, are shown in Figure 4-9. The three different periods of integration in Figure 4-9 correspond to the colored lines in Figure 4-6. The time sequence plot showing the ratio of the extinction coefficients enables us to see particle size variation over longer time periods as the atmosphere advects over the region. We see particle size variations, both small and large particles, pass through the lidar beam. Also, they transform in size if they are present for sufficiently long periods over the lidar beam. Figure 4-8 shows regions where particles grow in size, seen by the increasing two-wavelength particle extinction ratio, and other regions where the extinction ratio decreases indicates particles getting smaller. An increase in the 530/284 ratio corresponds to an increase in the relative size of the particles present in the scattering volume. The increasing particles size ratio could indicate regions when the lidar beam passes through the edge of a developing cloud, and into the cloud itself. If the region is sufficiently stable and the lidar beam probes the same region for a significant time, this increasing ratio would indicate particles growing in size due to particles accumulating water vapor or by coagulation of small particles. Similarly a decreasing ratio could indicate passing from inside a cloud to its trailing edge, or a region where the loss of water from aerosol particles results in decreasing size as the cloud is dissipating.

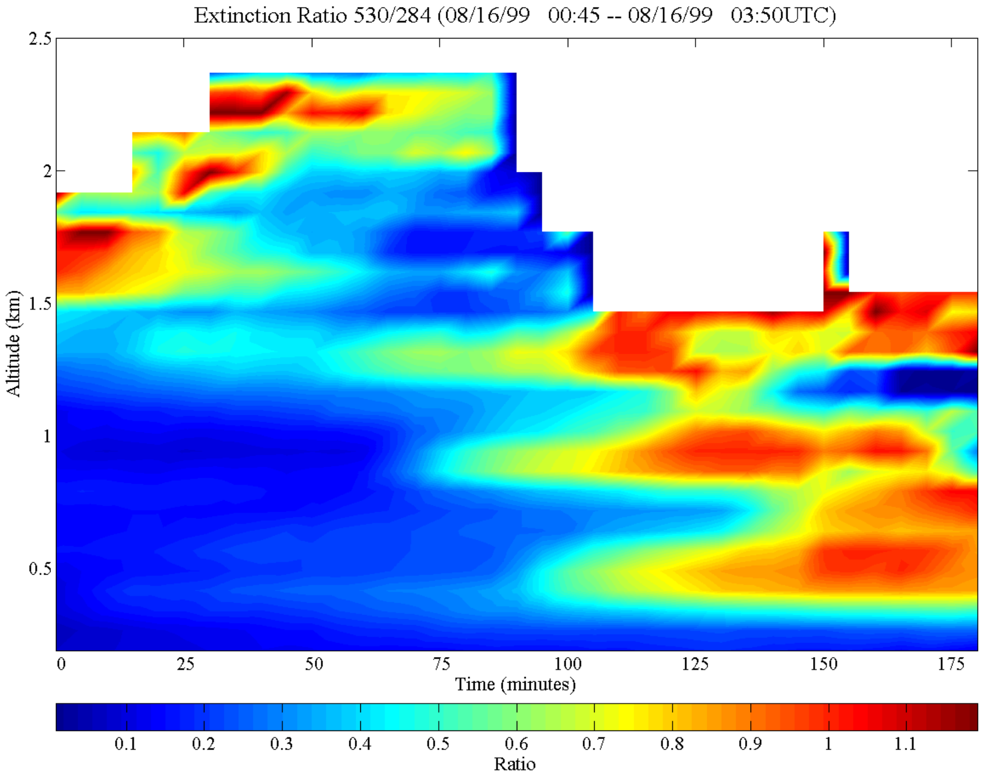

Figure 4-8: Ratio of extinction coefficient of 530 nm to 284 nm on August 16, 1999.

Figure 4-6(a) and Figure 4-6(b) show the presence of a cloud at 0045 UTC, between 1.5 km and 2 km, and we see the expected increase in the extinction coefficient ratios in Figure 4-9. The ratio is very close to 1.0 inside the cloud and this suggests that the cloud is composed of particle sizes greater than 2 μm to 5 μm. The ratio of 530 nm to 284 nm is also higher near the ground, indicating a higher concentration of larger aerosol particles in the surface layer. The ratio of the extinction coefficients at these different times (see Figure 4-9) depicts the evolution of the cloud, as it advects past the laser beam. Comparing the time sequences with the ratio plot, we see that as the cloud particle sizes begin to reduce the ratio begins to fall to lower values. This could be due to the edge of the cloud passing through the lidar beam, or the process of dissipation of the cloud. Both conditions would occur with changes from particles of larger to smaller sizes. We can also infer an increase in particle sizes between 1 km and 1.3 km in Figure 4-9 and the figure shows the time sequences plots as corresponding to increasing extinction in that region. Figure 4-6 also shows the capability of the LAPS Raman lidar to look through optically thick clouds. This is advantageous because it enables us to study the top and bottom layers of various cloud and aerosol layers.

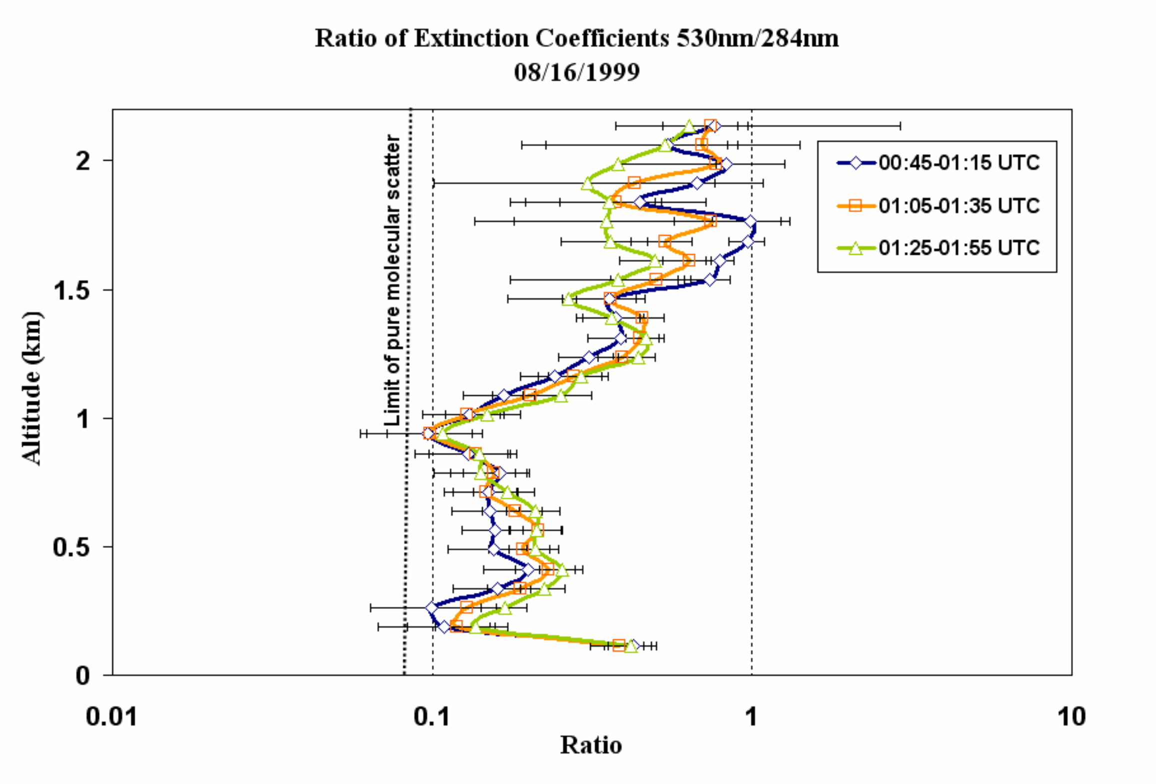

Figure 4-9: Ratio of extinction coefficient of 530 nm to 284 nm on August 16, 1999 taken for 30 min integrated time periods.

This dataset provided an opportunity to study the relationship between particle size increase/decrease in cloud regions, in terms of the extinction coefficients, and also changes in relative humidity. Figure 4-10 shows thirty minute integrated vertical profiles of the extinction coefficients calculated using the LAPS lidar. The three time periods shown correspond to the same time periods used in Figure 4-6 and Figure 4-9. The profiles of the extinction coefficients, at the different time periods, are placed side by side to emphasize the information that these plots have with respect to changing particle sizes in a region. Figure 4-11 shows the thirty minute integrated vertical profiles of the extinction coefficients along with the relative humidity profile measured using the Raman lidar during that time interval. Examination of Figure 4-10, shows changes in the extinction coefficients distinctly in two layers, one between 0.2 km and 0.8 km, and the other one between 1.5 km and 2 km. In the lower layer, between 0.2 km and 0.8 km, the extinction coefficients at 530 nm and 607 nm increase in values from 0045 UTC to 0155 UTC, while the extinction coefficients at 284 nm remain relatively constant. By looking at the relative humidity values during these time periods, we see that the increase in extinction values at 530 nm and 607 nm correspond to the simultaneous increase in relative humidity in that region. As the relative humidity values increase, the particles begin to grow in size as the water condenses onto the particles, thus causing an increase in the extinction values at 530 nm and 607 nm. We also observe that the change in extinction coefficients at 284 nm, in the lower region, remain relatively constant during the three time periods. This is consistent with what we would expect to see. Figure 4-1 shows that as the particles in the layer begin to grow in size, the longer wavelengths are affected more than the shorter wavelengths. As the larger particles begin to form and their population increases in the region, the extinction coefficient values of the longer wavelengths begin to approach those of the shorter wavelengths. Figure 4-12 shows the ratio of extinction coefficient of 530 nm to 284 nm, and relative humidity profiles measured using the Raman lidar on August 16, 1999 during the selected 30 min integrated time periods. Figure 4-12 shows the important relationship between changes in relative humidity and extinction ratio values. Since a change in the extinction ratio

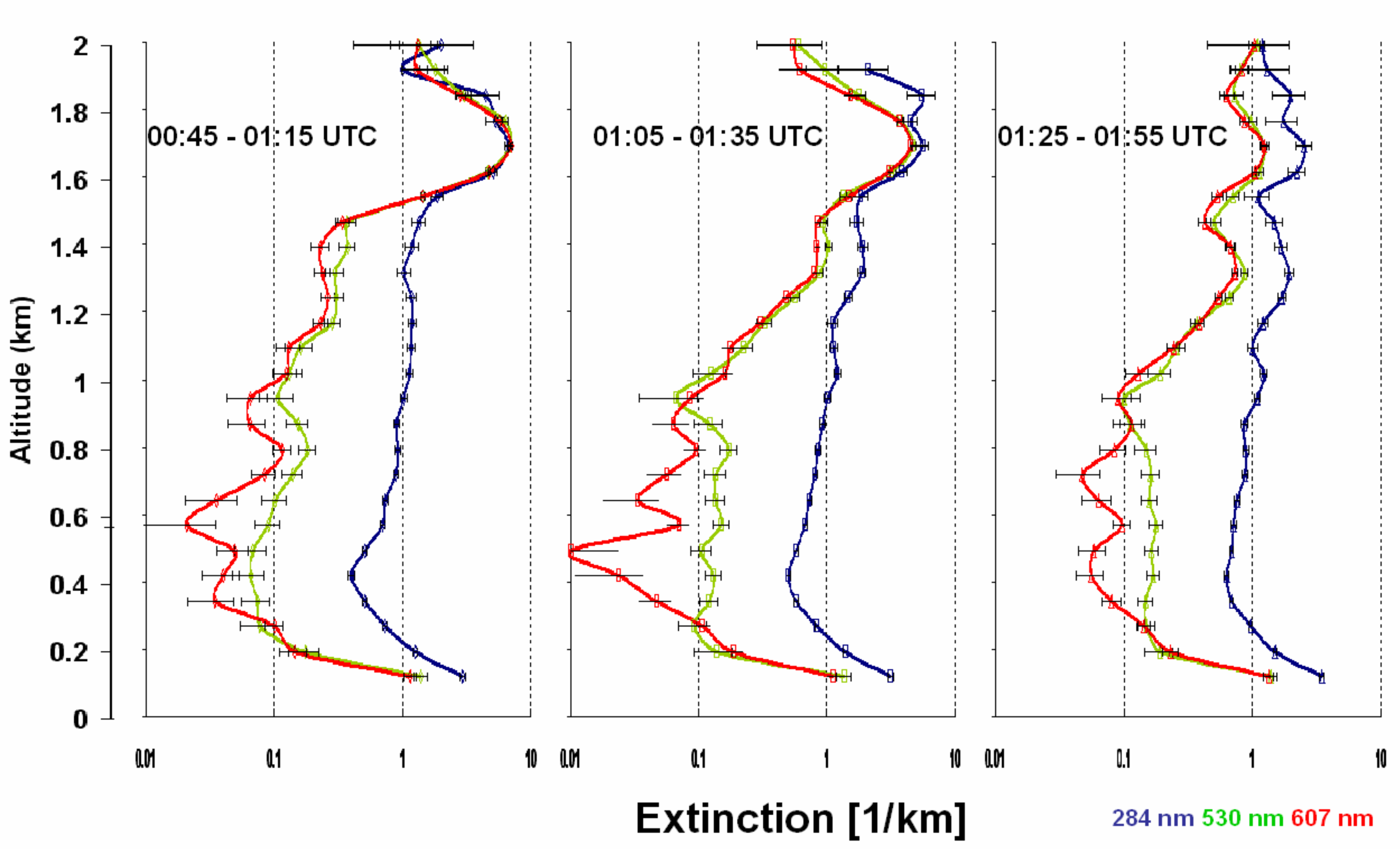

Figure 4-10: 30 min integrated vertical profiles of optical extinction at 284 nm, 530 nm and 607 nm for time periods shown in Figure 4-9.

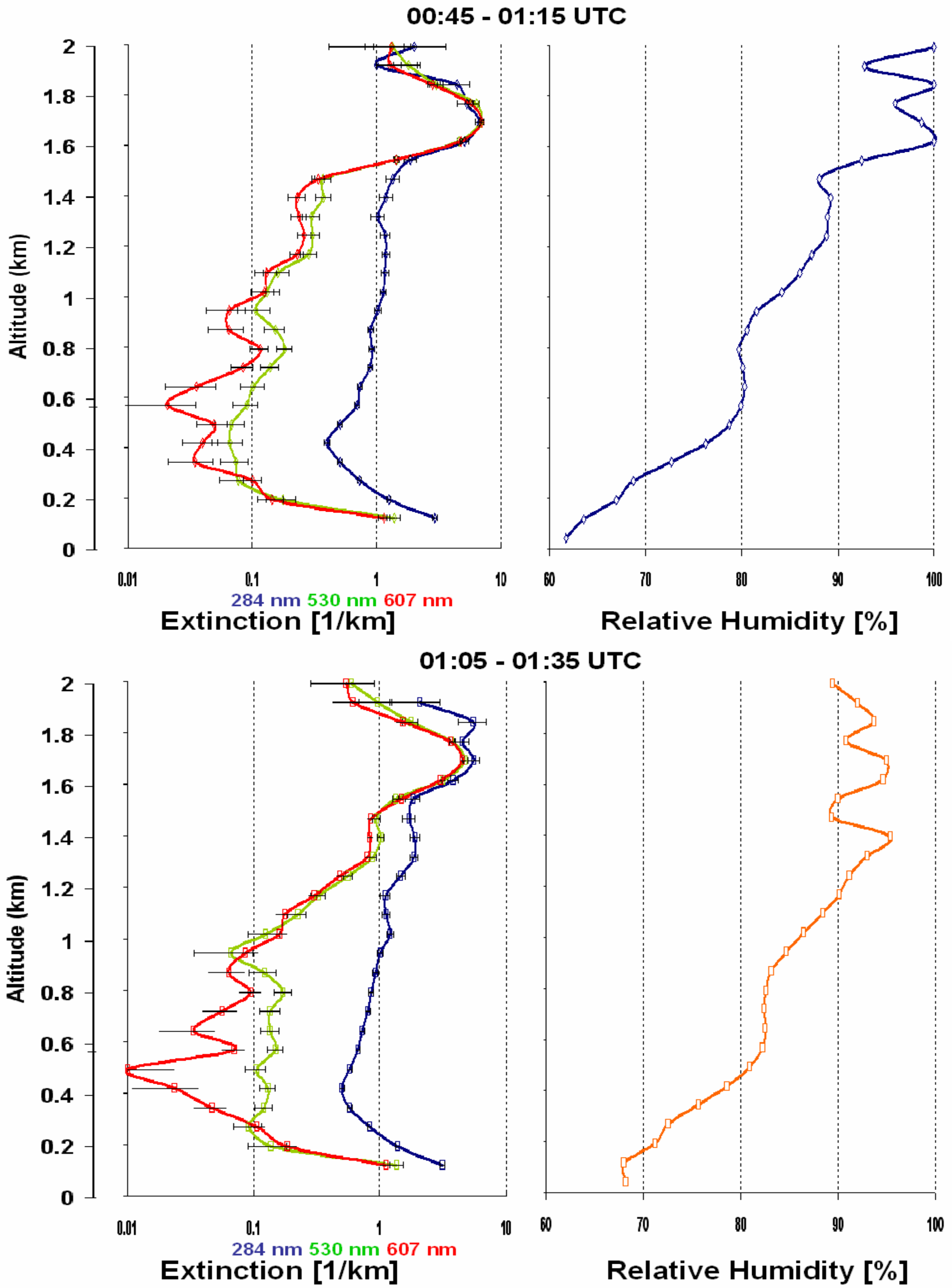

Figure 4-11: 30 min integrated vertical profiles of optical extinction at 284 nm, 530 nm and 607 nm and relative humidity calculated using the LAPS lidar on August 16, 1999 at (a) 0045 UTC (b) 0105 UTC

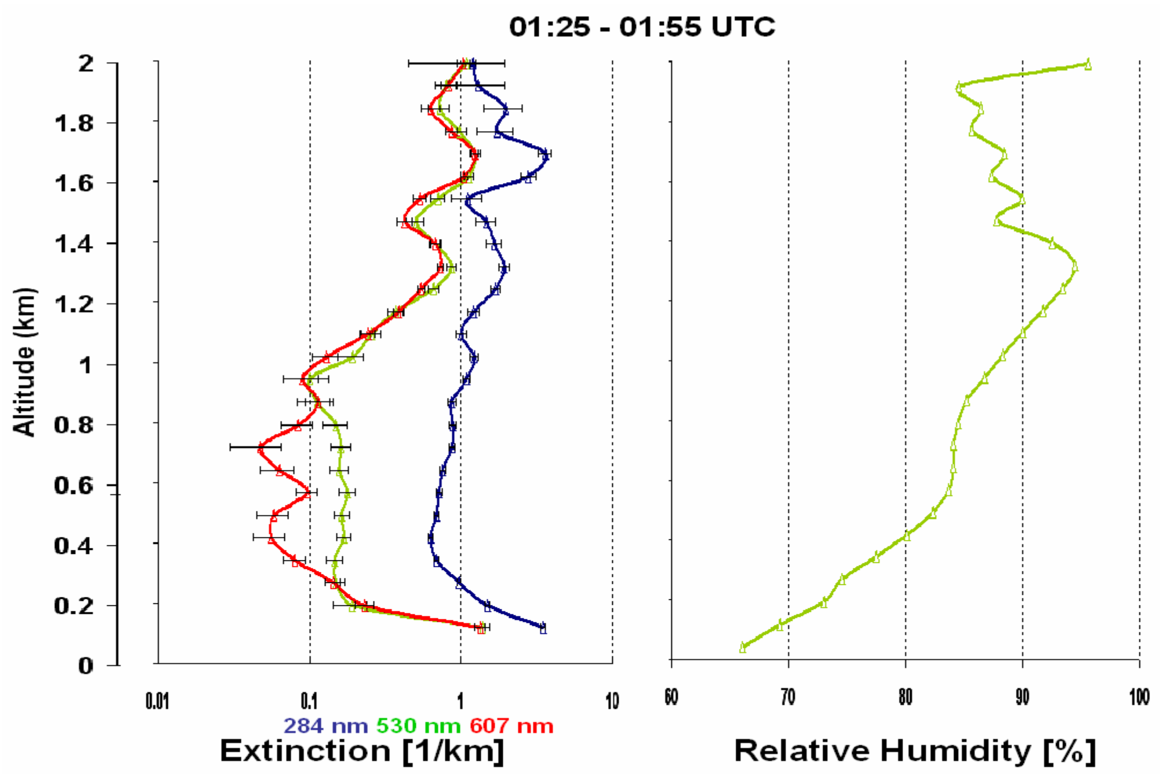

Figure 4-11(cont): 30 min integrated vertical profiles of optical extinction at 284 nm, 530 nm and 607 nm and relative humidity calculated using the LAPS lidar on August 16, 1999 at (c) 0125 UTC

corresponds to a change in the particle size, examination of Figure 4-12 shows that we can infer a one-to-one relationship between relative humidity and particle size changes. Figures 4-11 and 4-12, show that, in the region between 0.2 km and 0.8 km, the ratio of the extinction coefficients indicates an increase in value with time. The relative humidity profiles also show an increase of values with time, and support the interpretation of growth of particles in that region. As the particles grow, under the influence of increasing relative humidity and the corresponding condensation of water on the particles, the optical extinction ratio increases as the longer wavelength values increase more than the shorter wavelength.

In the upper region, between 1.5 km and 2 km, we observe the presence of a cloud at 0045 UTC, and we see the corresponding extinction ratio reach a value of 1 inside the cloud indicating a distribution of larger particles (> ~ 5 µm). Figures 4-11a and 4-12 also show the relative humidity in that region is close to 100%. As we examine later times, the cloud particle sizes begin to decrease, the ratio begins to fall to lower values, and the relative humidity decreases in the region. The region becomes populated with a distribution of smaller particle sizes due to the lower relative humidity in the region. The distribution of smaller particles results in the extinction ratio falling to lower values as the extinction coefficient values of the longer wavelengths reduce. The shorter wavelength extinction coefficients are less affected, as expected based on data in Figure 4-1. Notice that the extinction coefficients of the longer wavelengths decrease from the shorter wavelengths rapidly as the cloud begins to dissipate (see Figure 4.10).

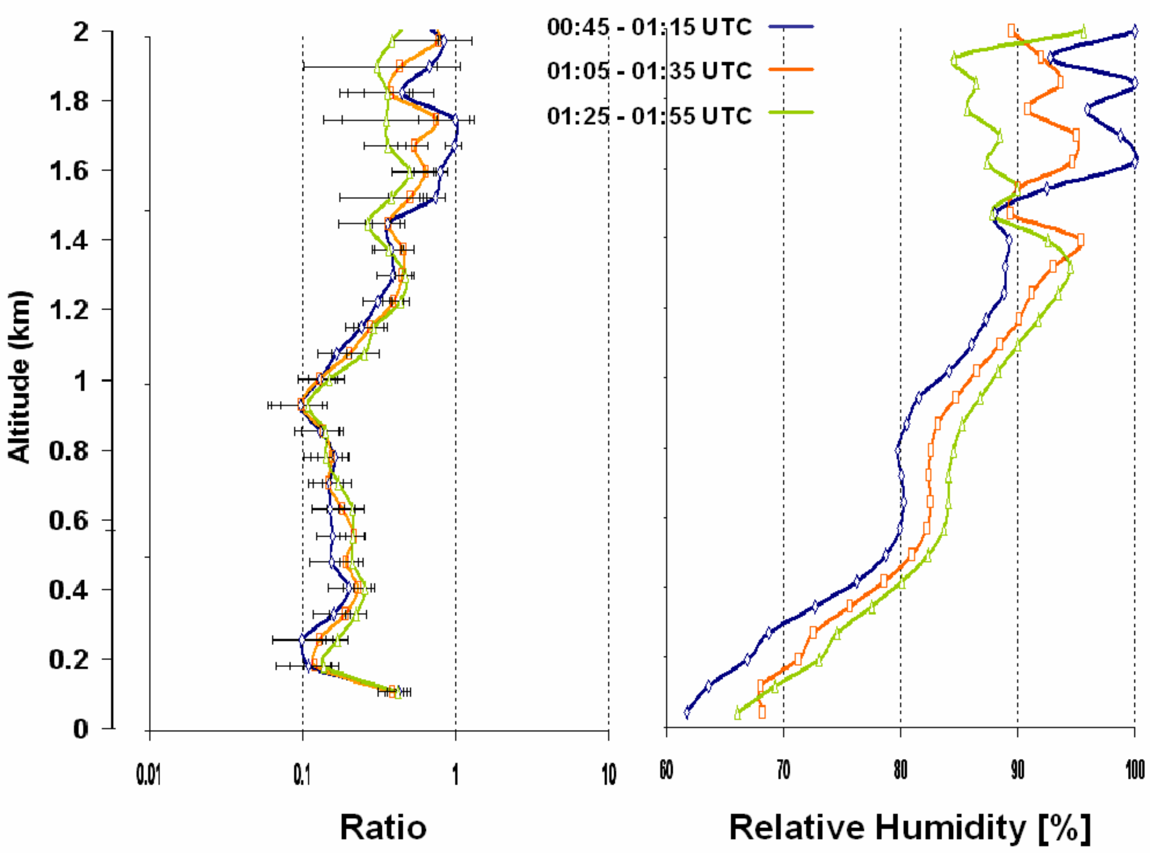

Figure 4-12: Ratio of extinction coefficient of 530 nm to 284 nm, and relative humidity on August 16, 1999 taken for 30 min integrated time periods. The changing relative humidity at the different times is seen to correspond to changes in the ratios of the extinction coefficients.

Figures 4-11 and 4-12 clearly exhibit the relationship that exists between the relative humidity, extinction ratio and particle size change. This data set provides an example where we see that as the relative humidity values increase in a region the particles grow in size due to the water condensing onto the particles, and result in an increase in the extinction ratio. Similarly, when the relative humidity in the region becomes less, the resulting distribution of smaller particles leads to a drop in the extinction ratio. Several cases supporting this picture of the relationship between the extinction, particle size change, and relative humidity have been studied and another example is now briefly considered.

Atmospheric data obtained during the testing of the LAPS Raman lidar onboard the USNS Sumner have provided a rich dataset for studying the lower marine boundary layer. Since several sets of measurements were made during cloudy conditions, we selected a time period for our analysis using the extinction ratio to describe variations of the aerosol and cloud particle sizes as a function of altitude and time. Figures 4-13 (a), (b), and (c) show the optical extinction obtained using the LAPS Raman lidar at the three wavelengths on 4 October 1996. Figure 4-13(d) shows measurements which have been filtered using a 30 minute integration of the optical extinction at each of the wavelengths during the time when clouds were passing over the lidar beam. Measurements of profiles of water vapor mixing ratio and temperature obtained simultaneously using the Raman lidar are shown in Figure 4-14. The water vapor data are shown for 1 minute time steps with 5 minute smoothing, and the temperature data are shown for 5 minute steps with 30 minute smoothing. Rawinsonde balloons were released onboard the USNS Sumner during several time periods that coincide with the lidar measurements. Temperature and relative humidity data obtained from a balloon sounding at 1000 UTC are shown in Figure 4-15. Figure 4-16 shows the time sequence of the ratio of the extinction coefficients obtained for 530nm/284nm. Figure 4-13 shows the presence of clouds, at 0.5 km and between 2 km and 2.5 km, in the optical extinction data at each of the three wavelengths. The extinction plots indicate the presence of large particles in the lower 500 m of the marine boundary layer. This is consistent with expectations based upon the high humidity combined with the presence of hygroscopic particles from sea spray; containing sea-salt typical of the marine boundary layer. By comparing the extinction ratio plot, Figure 4-16, with theoretical calculations using Mie theory, we can conclude that the lower 500 m is composed of particles greater than 0.3 μm in radius as the visible to ultraviolet wavelength ratio values are seen to be greater than

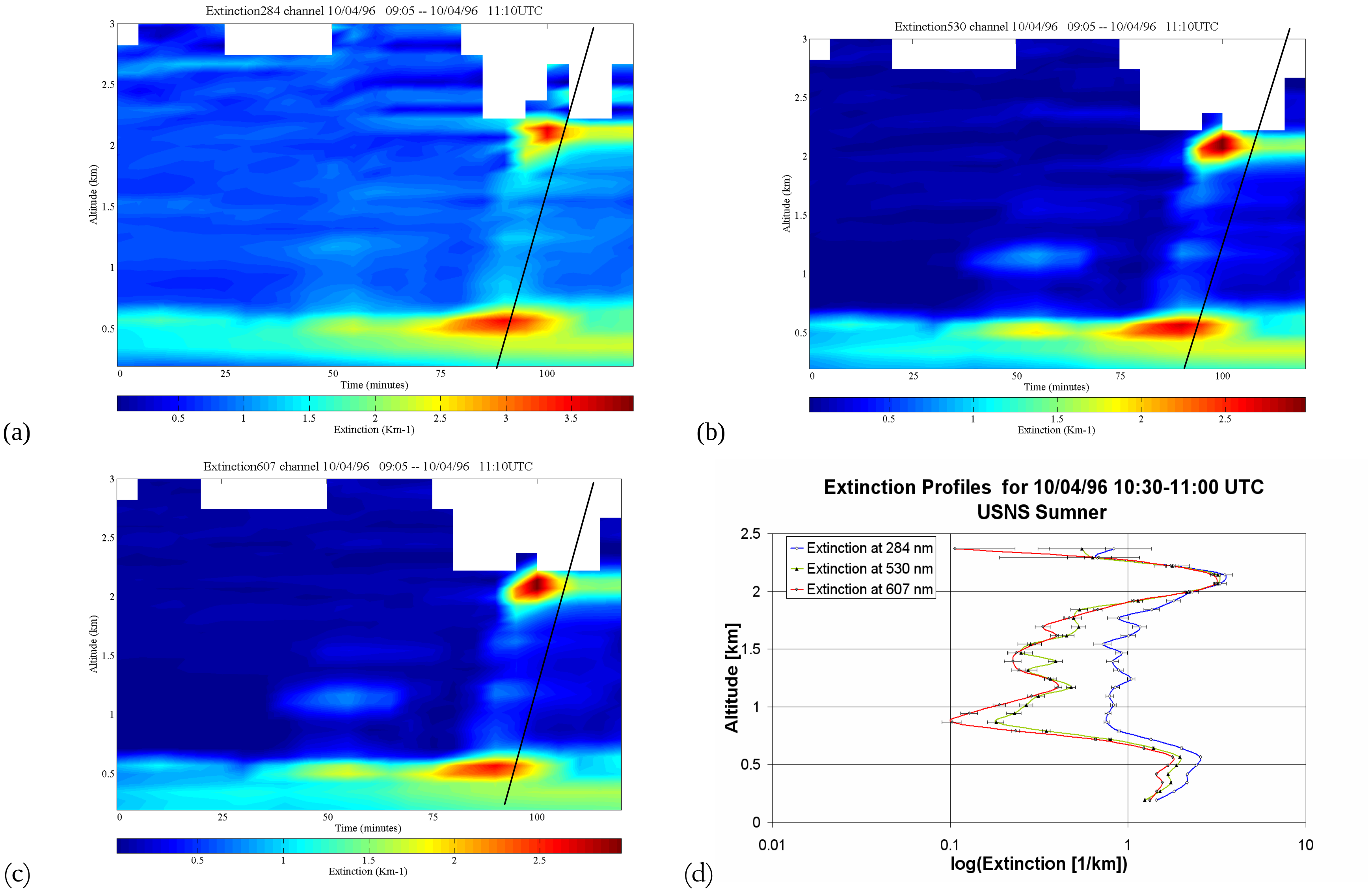

Figure 4-13: Time sequence of plots of optical extinction obtained onboard the USNS Sumner on October 4, 1996. (a) 284 nm (b) 530 nm (c) 607 nm (d) 30 minute integrated extinction profiles for the three wavelengths. The line on the time-sequence plots is a reference to the integrated extinction profiles in 4-13 (d).

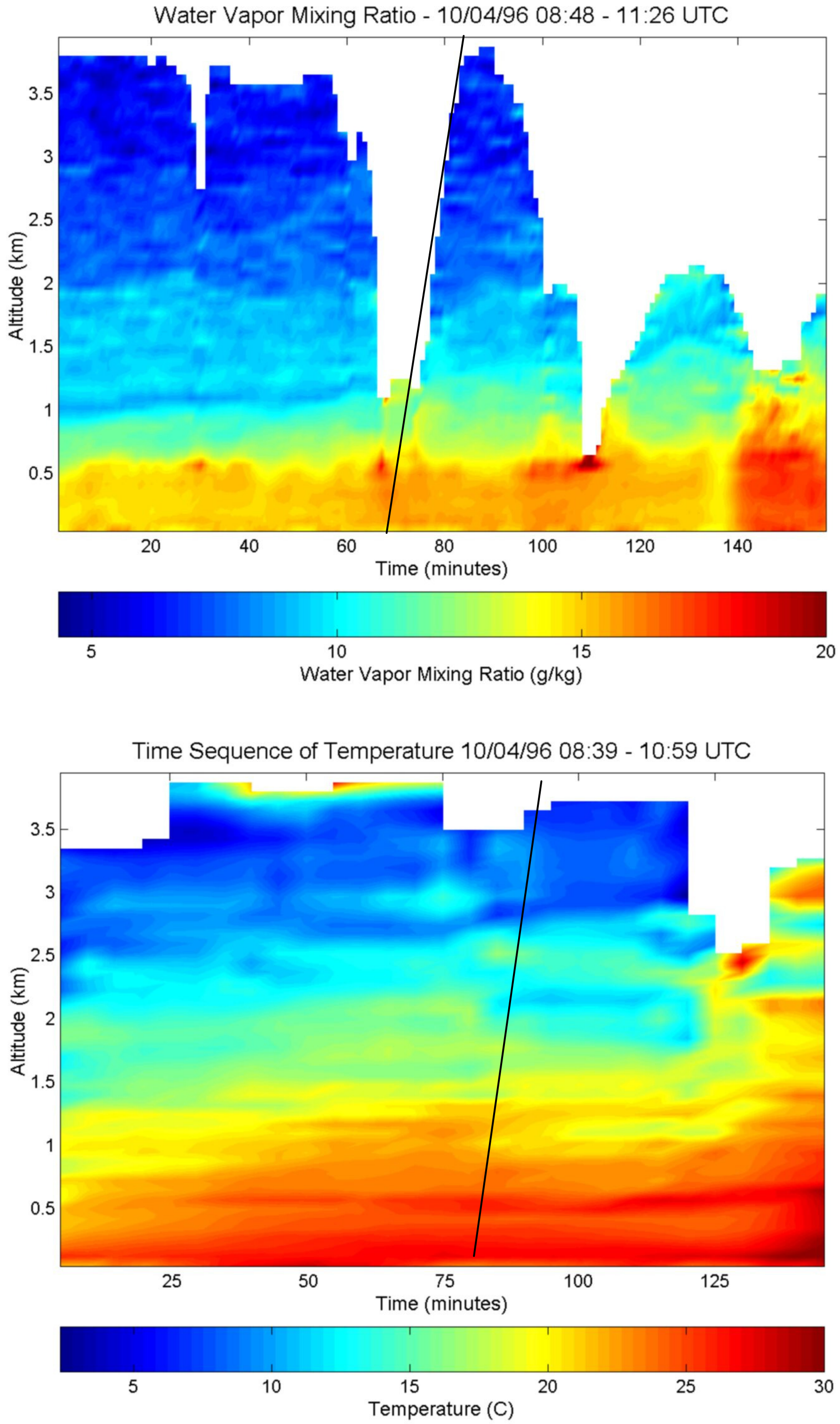

Figure 4-14: Water vapor mixing ratio and temperature profiles obtained using the Raman lidar on October 4, 1996. The line on the plots is a reference to the balloon sounding, shown in Figure 4-12, onboard the USNS Sumner at 1000 UTC.

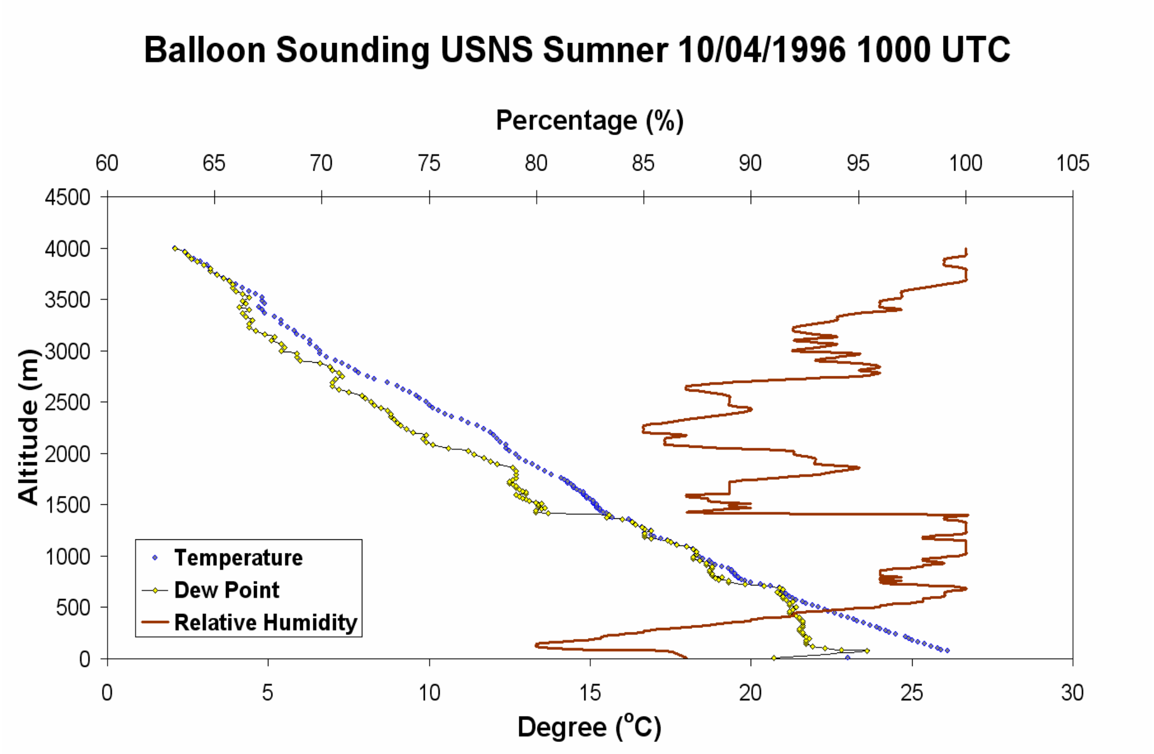

Figure 4-15: Temperature and relative humidity measurements obtained onboard the USNS Sumner on October 4, 1996.

0.7. We also see that the extinction ratio values close to the surface are much higher for this case study than the previous one, which measured continental aerosols during the NEOPS 99 campaign. The measurements here exhibit a characteristic typical of larger particles in the marine boundary layer.

The time sequence plots of extinction at the different wavelengths and the extinction ratio plot (see Figure 4-16) also reveal the presence of a sub-visual cloud beginning to form above the ship at around 0945 UTC. This cloud layer, between 1 and 1.5 km is observed as a slight increase in the extinction values, but is seen clearly when the ratio of the extinction coefficients are taken (see Figure 4-16). The data obtained from a balloon sounding at the same time, see Figure 4-15, shows high relative humidity in the region where the cloud exists and this corroborates the conclusion that there exists a growing cloud in that region. A 30 minute integrated profile of the extinction ratio during

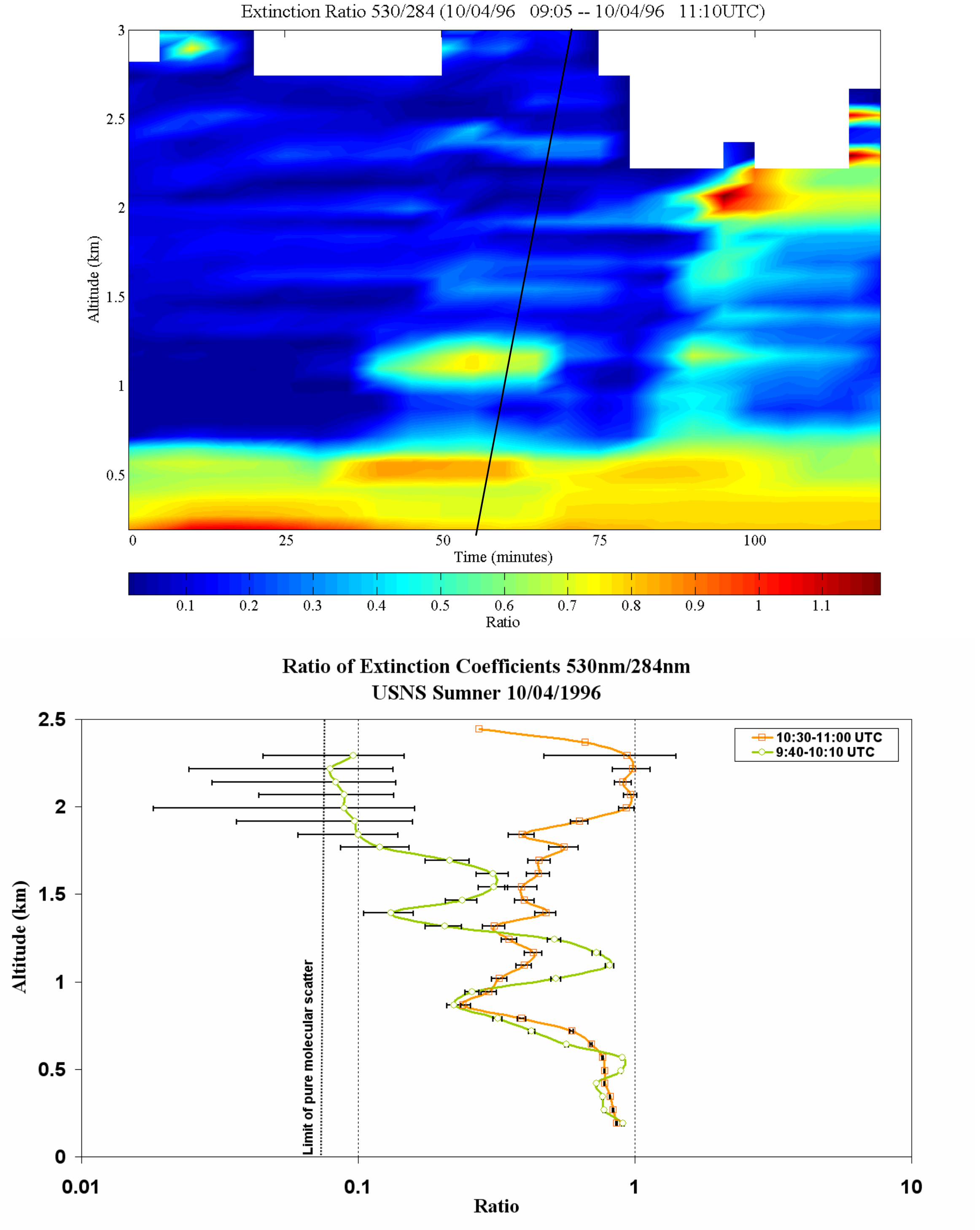

Figure 4-16: Ratio of extinction coefficient of 530 nm to 284 nm on October 4, 1996. (a) 0900 -1110 UTC. The line on the plots is a reference to the balloon sounding, shown in Figure 4-12, onboard the USNS Sumner at 1000 UTC (b) 30 min integrated time periods.

this time period is shown in Figure 4-16(b). We see the extinction ratio falls to lower values once above the marine boundary layer because of the reduced number of larger particles. The ultraviolet extinction is greater than the visible extinction values in this region because of the larger number of smaller scattering particles. The fact that the scattering is proportional to the 6th power of the radius and inversely proportional to the fourth power of the wavelength indicates that the smaller particles outnumber the larger particles by several orders of magnitude in this region. Near 1 km, the extinction ratio values begin to increase toward a value of 1, indicating the presence of particles in the size range of clouds, and then begin to fall back to values signifying smaller particles when we are outside the region of the cloud. Above 2 km the extinction ratio falls close to the limit for pure molecular scattering, indicating a region dominated by the presence of atmospheric molecules. Figure 4-16(b) also shows a 30 minute integrated profile at a later time. We notice the lower values between 1 to 1.5 km indicate the replacement of the cloud region with a distribution of smaller particles. The extinction ratio also increases to a value of 1 between 2 and 2.3 km indicating the presence of a cloud and we observe the corresponding increase in the extinction coefficients in Figure 4-13. This analysis depends on the theoretical results, which indicate a small extinction ratio when the particles are smaller than the wavelength used, and the ratio increasing to unity as the extinction coefficients lose their wavelength dependence when particles grow towards size ranges found in cloud structures.

4.2 Optical Extinction Variations during Morning and Nighttime

Optical extinction variations induced by aerosol and atmospheric changes during different periods of the day have been documented for a number of data periods during several field campaigns. This has provided the opportunity to study and compare, the processes associated with increases or decreases in optical extinction values in the lower boundary layer in different regions of the United States. Frequent variations, with increased extinction values after sunrise and sunset were observed on many days during the SCOS and the NEOPS campaigns. The data obtained demonstrated different characteristics which depend on variation in the processes during the times of increased/decreased extinction. Figure 4-17 shows the UV and visible optical extinction measurements obtained by the LAPS Raman lidar during the night of August 26th 1997 at Hesperia, CA. Simultaneous measurement of water vapor mixing ratio are shown in

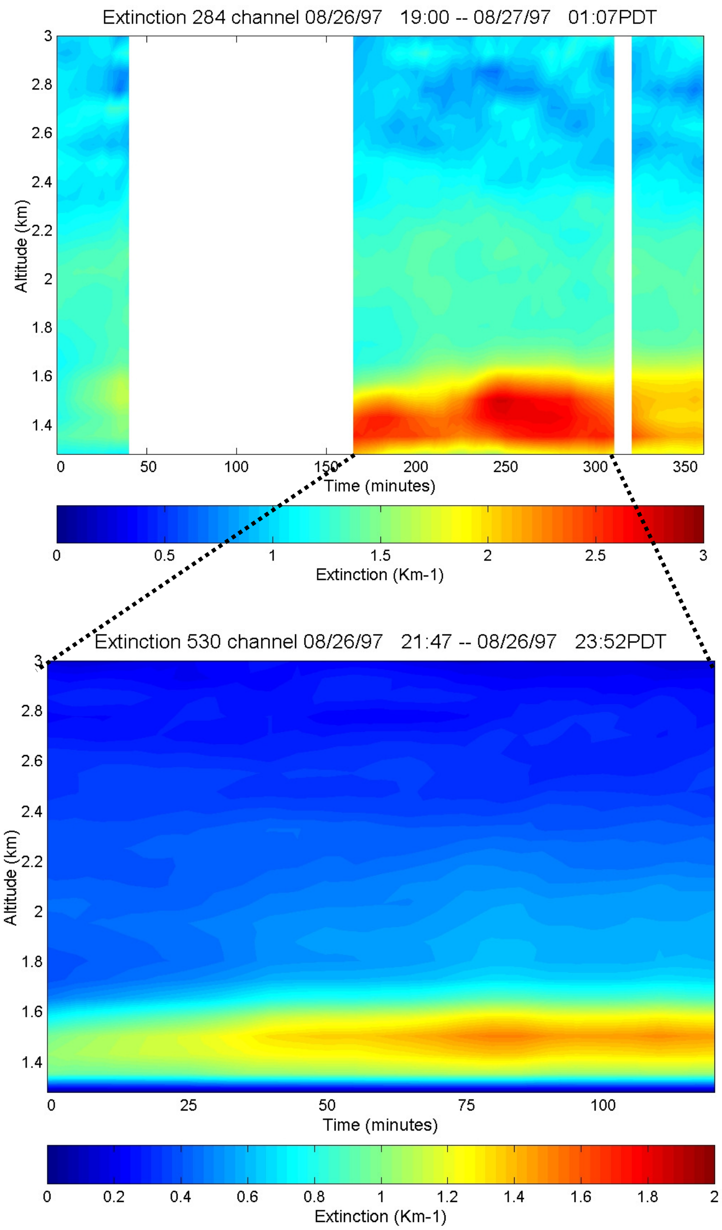

Extinction 284 channel 08/26/97 19:00 -- 08/27/97 01:07PDT

Extinction 530 channel 08/26/97 21:47 -- 08/26/97 23:52PDT

Figure 4-17: Time sequence of plots of optical extinction obtained after sunset on August 26, 1997. (a) 284 nm (b) 530 nm

Figure 4-18. Figure 4-19 shows surface measurements of temperature and relative humidity at the site, while Figure 4-20 shows measurements of surface ozone and NO_x. The period when the optical extinction measurement were available, seen in Figure 4-17, is represented as the first shaded yellow period in Figure 4-19 and Figure 4-20. From Figure 4-17 we observe a steady increase of extinction values in the lower boundary layer immediately after sunset. We also observe from Figure 4-18 a layer rich in water vapor to be present in the nocturnal boundary layer as much of the moisture content gets trapped there when convective mixing ceases after sunset. The extinction values in the ultraviolet and visible wavelengths indicate the growth of particles during the night as we observe the extinction values at 530 nm increase with time close to the surface. The temperature decrease coupled with the relative humidity increase shown in Figure 4-19 results in aerosol growth in the lower boundary layer. The water vapor content present in the lower layer plays an important role in the increased extinction values because the

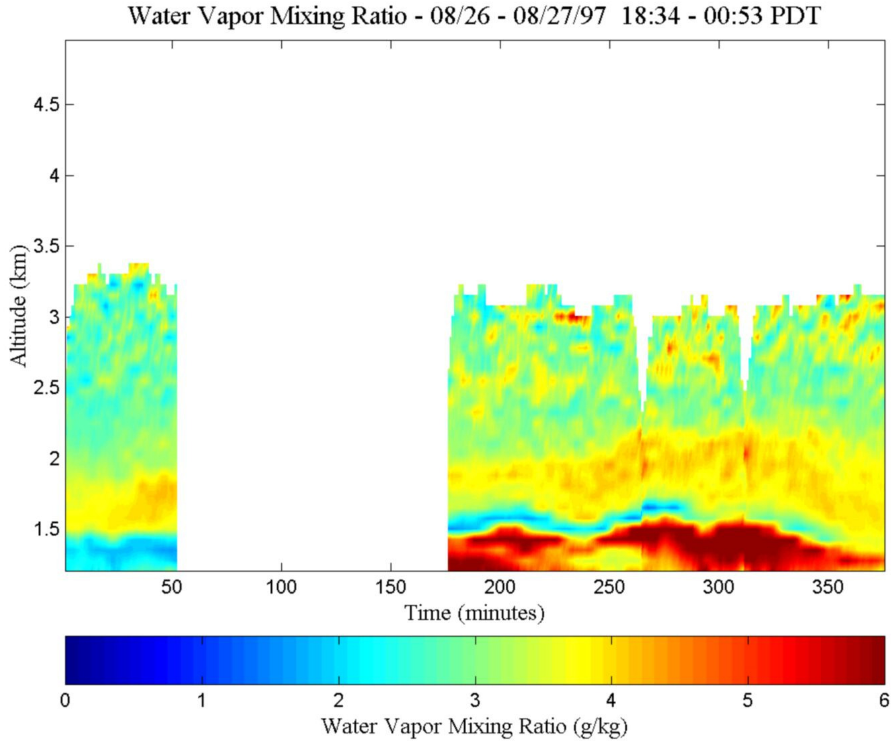

Figure 4-18: Water vapor mixing ratio obtained on August 26, 1997.

particles grow by condensing water vapor. The scattering cross-section of the particle increases, and thus increases the optical extinction. The extinction at the ultraviolet wavelengths tends to remain constant as the particles grow larger in size than the wavelength, and thus causes a smaller effect on the ultraviolet extinction values. If the number density of the aerosol particles was changing in this region, rather than just the size increasing, the UV extinction would increase. However, we only observe the extinction values at 530 nm to be increasing as the night progresses indicating growth of particles in the accumulation mode range, and not a change in the number of particles in this layer. In Figure 4-20 we also observe that changes in the ozone and NO_x values do not appear to contribute much to the aerosol extinction coefficients (the ozone absorption contribution to the extinction has been removed).

Figure 4-21 shows the UV and visible optical extinction measurements obtained by the LAPS Raman lidar during the early hours of the morning on the next day. The start and end times of this measurement period are indicated in the plots of the surface measurement as the second shaded block of yellow in Figure 4-19 and Figure 4-20. Soon after sunrise, we observe the extinction coefficients drop to lower values, in the lower altitude layer near the surface, as the temperature begins to increase. The extinction values drop to an extinction value of 1 km^{-1} over a 30 minute period as the temperature begins to increase and the relative humidity begins to decrease. The decreasing relative humidity along with the increase in temperature results in the evaporation of water from the hygroscopic aerosols after sunrise. Hence the scattering efficiency reduces due to presence of smaller size particles, which causes a decrease in the extinction values at both the wavelengths. The redistribution of water from liquid to vapor phase can also be observed in the time sequence plot of water vapor mixing ratio shown in Figure 4-22. Before sunrise we see the layer of high extinction values at 1.4 km to correspond to a layer of decreased water vapor content in Figure 4-22. This decrease in the water vapor results due to the change from vapor phase to liquid as water condenses on to hygroscopic particles. As the temperature increases and the corresponding water vaporizes from the particles we see the water vapor content to increase in the layer and particle extinction to decrease.

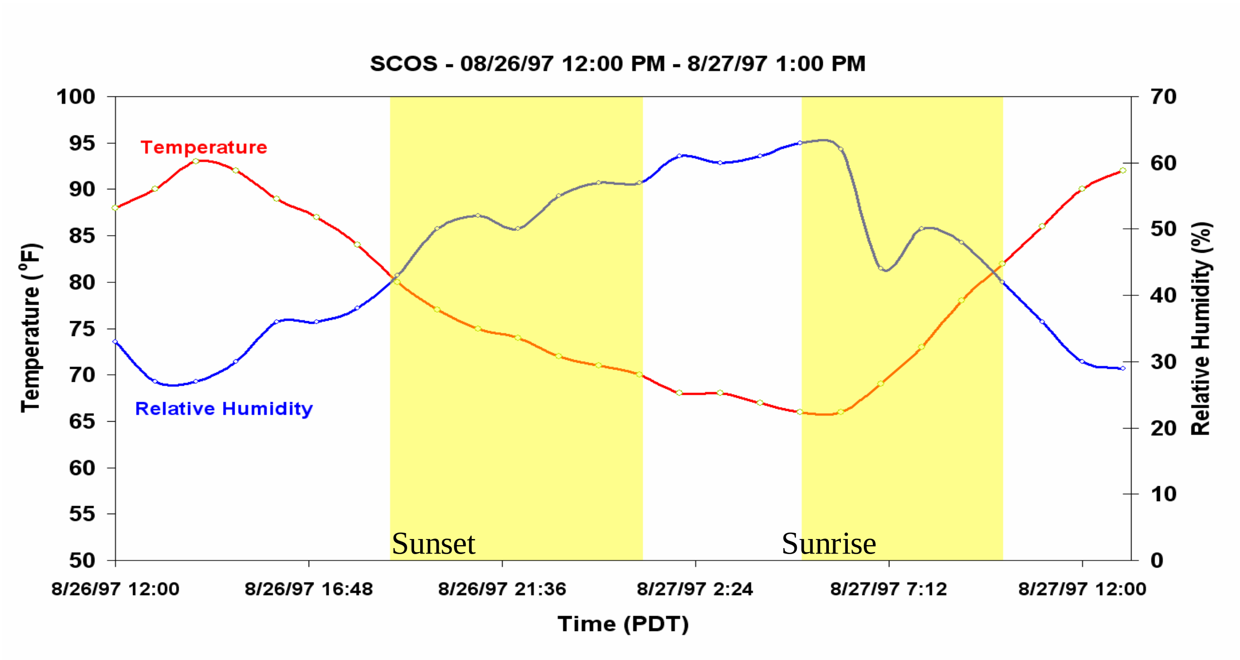

Figure 4-19: Surface measurements of temperature and relative humidity during the SCOS campaign, at Hesperia, CA, on August 26-27, 1997 (Data courtesy Leon Dolislager).

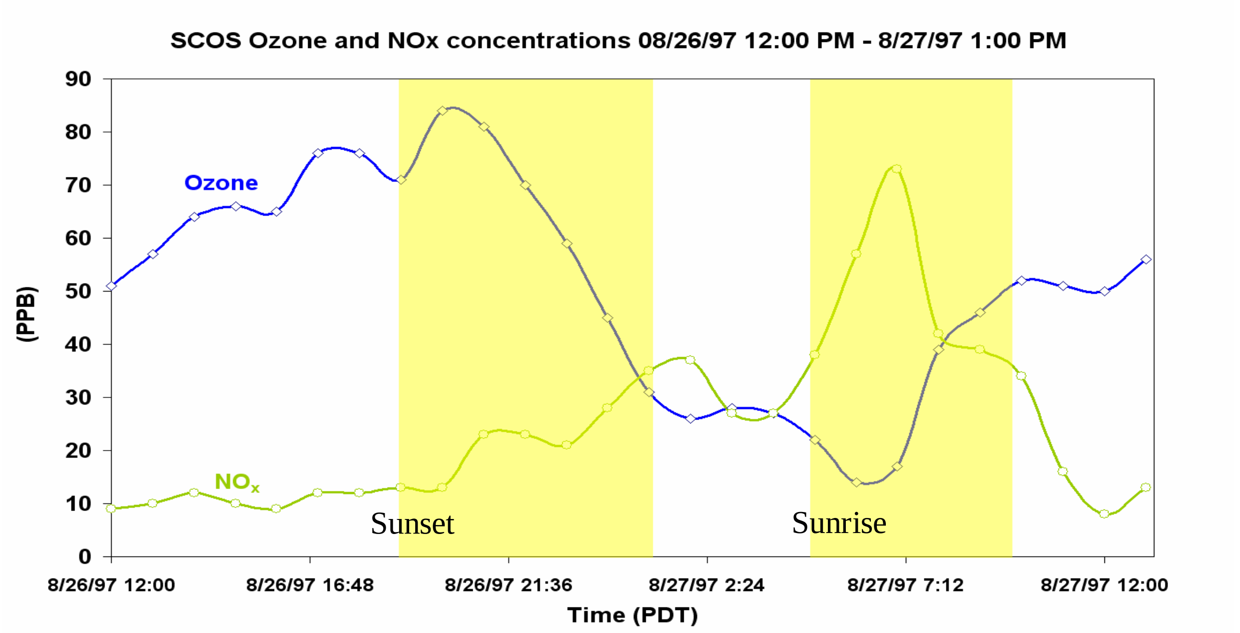

Figure 4-20: Surface measurements of ozone and NO_x during the SCOS campaign, at Hesperia, CA, on August 26-27, 1997 (Data courtesy Leon Dolislager).

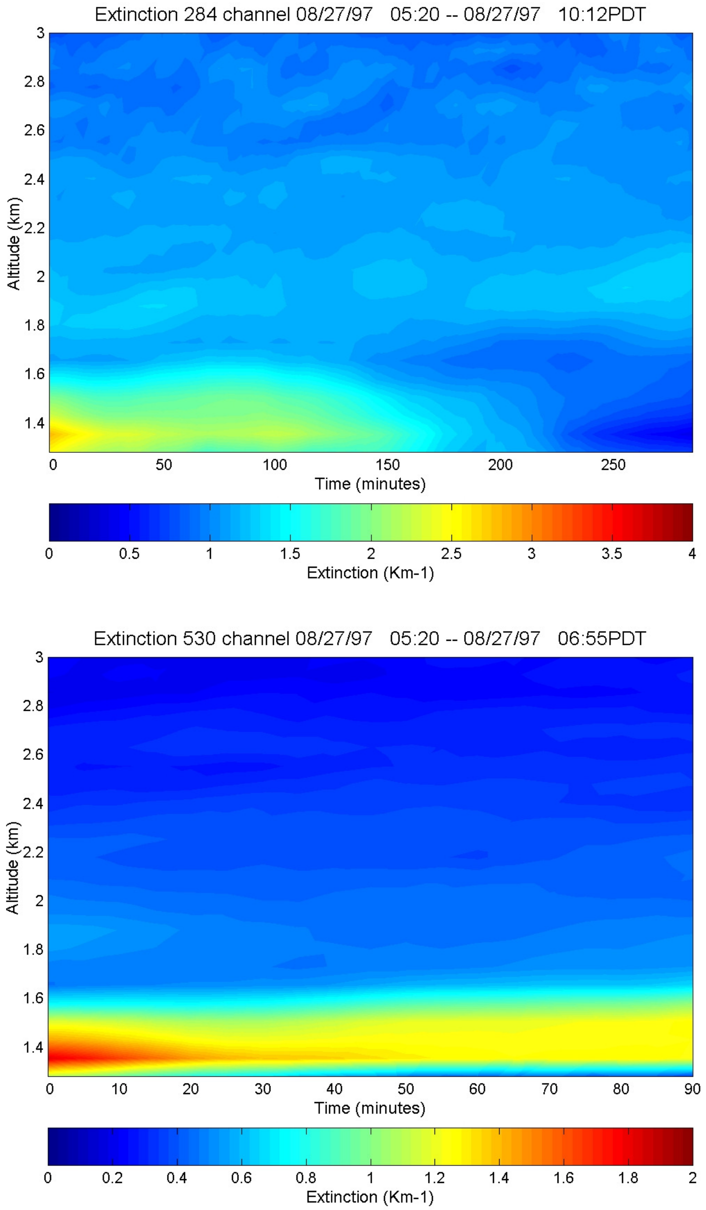

Figure 4-21: Time sequence of plots of optical extinction after sunrise on August 27, 1997. (a) 284nm (b) 530 nm

Another interesting feature is that the increase in pollutant concentrations does not affect the optical extinction values. We see an increase in ozone and NO_x concentrations after sunrise but the extinction values at both wavelengths do not follow with this change because the extinction is being governed by the scattering of the hygroscopic aerosols.

This leads to the conclusion that the extinction variations during the morning and nighttime during the SCOS campaign (western U.S.) are more closely tied to changes in atmospheric moisture than to chnages in pollutant concentrations. There are periods when the particulate matter is the governing factor, but the size of the aerosol particles, which depend on the amount of water available to grow the hygroscopic aerosols, is more important. We have also observed a number of other cases during the SCOS campaign, which follow the same trend; an increase in optical extinction after sunset, and a decrease in extinction values after sunrise. The SCOS campaign was conducted during the period of unusually high precipitation due to the peak of the El Nino period; so there was more moisture available than usual, and may have contributed to the process.

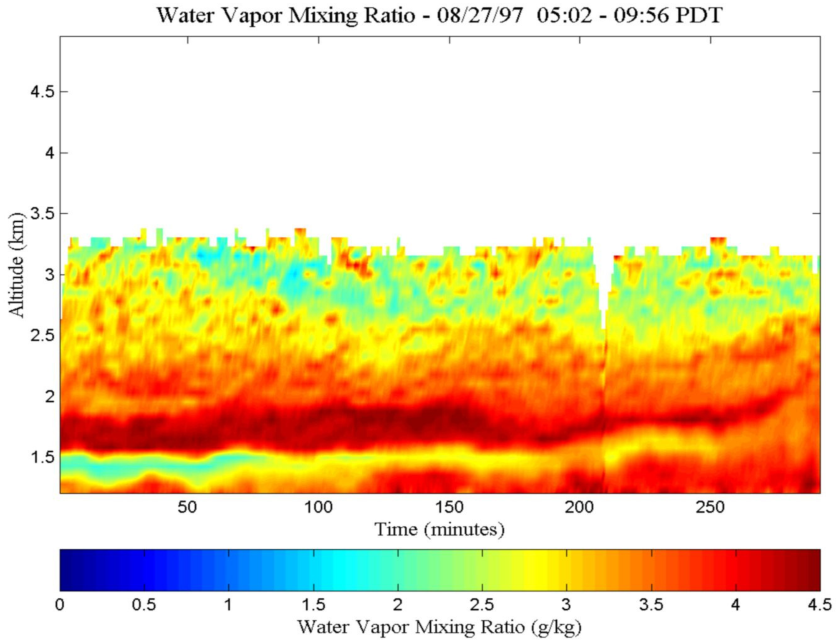

Figure 4-22: Time sequence of water vapor mixing ratio obtained during the morning of August 27, 1997.

Diurnal variations of the optical extinction were also observed in a number of datasets during the NEOPS campaigns at Philadelphia. In a large number of cases, an increase in optical extinction was observed following sunrise and a subsequent decrease in extinction values occurred in the nocturnal boundary layer. Figure 4-23 shows two examples of optical extinction variations that were typically observed after sunrise. We have analyzed the case of August 5 1999, taken during the NEOPS campaigns at Philadelphia, to better understand the sources responsible for the increase in optical extinction values in the boundary layer after sunrise. Figure 4-24 shows plots of 10-meter met-tower measurements of the various meteorological variables that were measured by our laboratory, as well as ozone and $PM_{2.5}$ concentrations measured by the Philadelphia AMS and the Harvard School of Public Health (HSPH) respectively. The meteorological variables are plotted with 15 minute averages, the $PM_{2.5}$ concentration with 10 minute

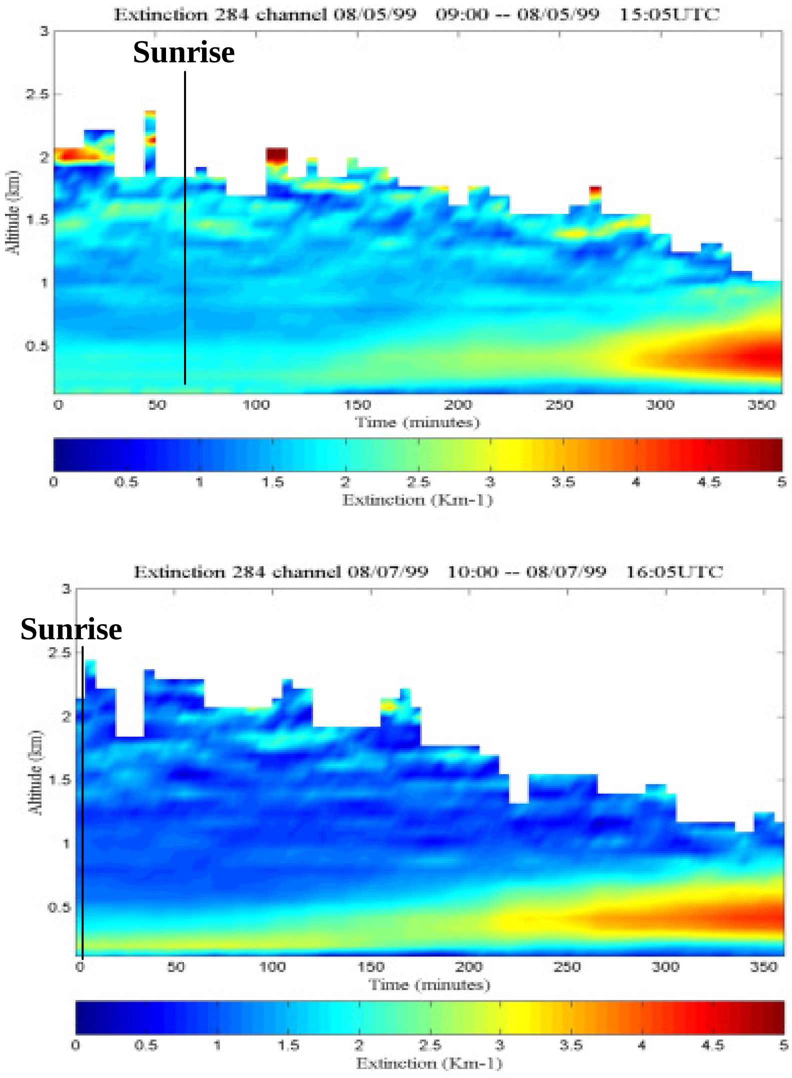

Figure 4-23: Time sequence of extinction at 284 nm showing variations in values after sunrise on (a) August 5 1999 and (b) August 7 1999.

averages, and the ozone concentration is plotted for 1 hour averages. We see from the time sequence of the extinction plot, on August 5 1999 that the optical extinction values begin to rise at about 1100 UTC and this coincides exactly with the time when the temperature and solar radiation begin to increase. From Figure 4-24 we also observe a steady rise in the concentration of $PM_{2.5}$ and ozone at this time. The increase in the optical extinction values during the morning, in contrast to the decreasing extinction values that were observed during the SCOS campaigns, is associated with the daily rise in temperatures and the onset of human activity in the region. As the temperature begins to increase after sunrise, convective turbulent activity builds up the boundary layer causing the moisture and pollutant precursors to mix uniformly. Fresh particulate matter generated from vehicular emission and other industrial activities are also injected into the boundary layer increasing the optical extinction. Figure 4-25 shows the ozone concentrations in the boundary layer at the same time when the optical extinction values began to increase. We see the increase in ozone concentrations follows the same pattern that we observed for the extinction after sunrise. The ozone concentration of about 120 ppb contributes to about 1.5 km^{-1} of the total optical extinction at 285nm. However, the extinction has a peak value of about 5 km^{-1} and this contains contributions from the other pollutants and from the newly formed larger particles as the boundary layer begins to grow due to convective mixing.

After sunset, as the convective activity ceases, it is observed that the optical extinction began to drop to lower values and stayed low till the next morning. Figure 4-26 shows an example of the decrease in the extinction values after sunset on August 11 1999. Figure 4-27 shows plots of met-tower measurements of the various meteorological variables as well as ozone and $PM_{2.5}$ concentrations measured on August 11 1999. We see from Figure 4-27 that the ozone and particulate matter concentrations begin to dip as soon as solar heating stops after sunset, at around 2200 UTC. This is can be attributed mainly to the cessation of convective mixing as well as to the decrease in the level of vehicular and industrial activity. The optical extinction measurements also follow this trend and values begin to drop as soon as levels of pollutant concentrations drop. The optical extinction values drop from a value of 5 km^{-1} to a value of about 1.5 km^{-1} during

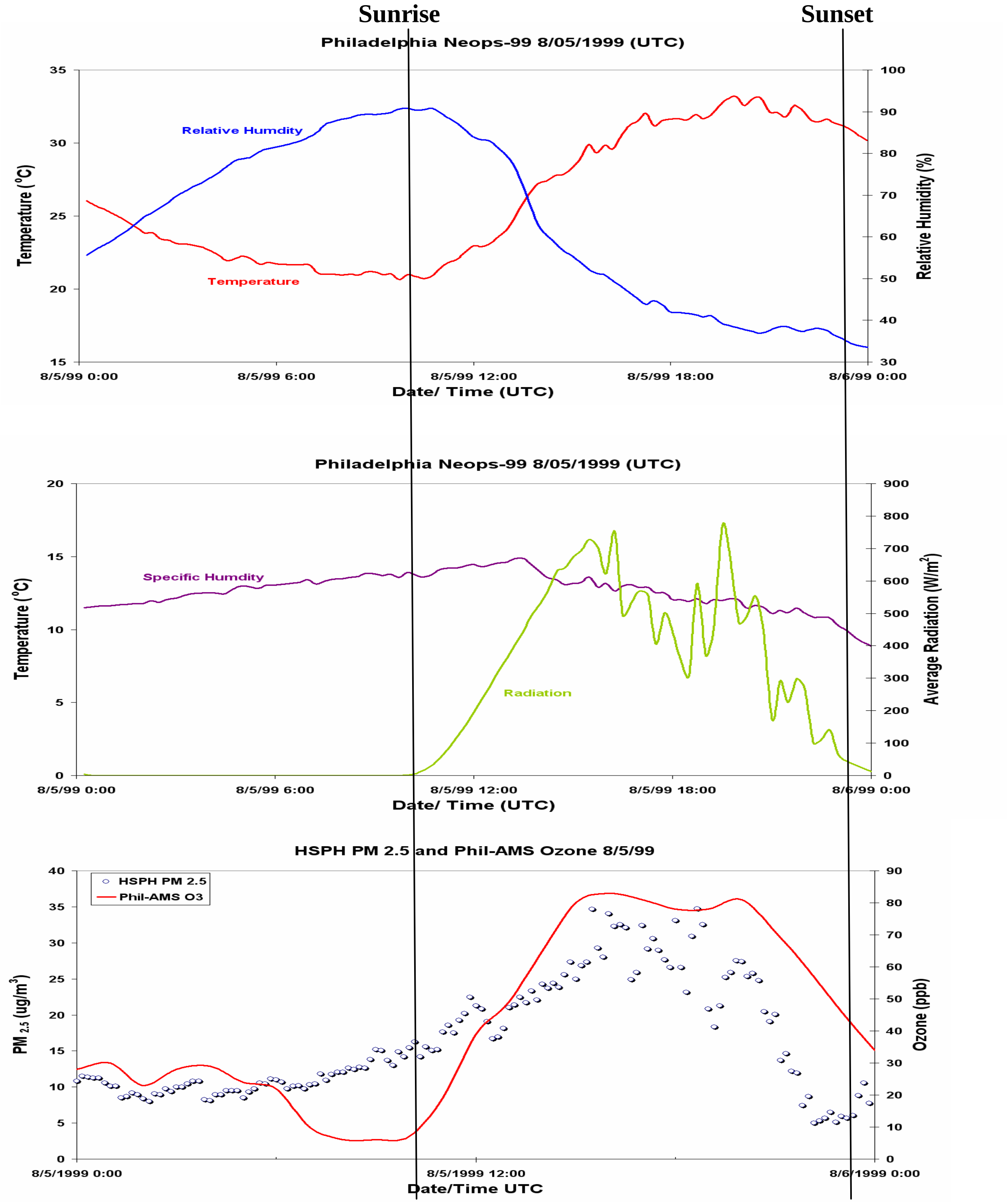

Figure 4-24: Relative humidity, temperature, specific humidity, solar radiation, ozone (Philadelphia AMS) and $PM_{2.5}$ (HSPH) on August 5 1999.

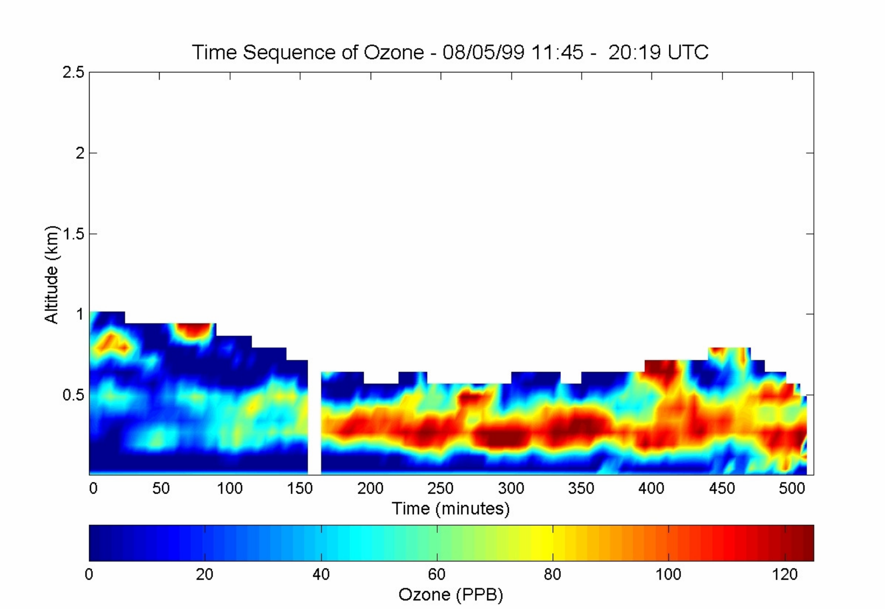

Figure 4-25: Ozone concentrations measured by the LAPS Raman lidar on August 5, 1999.

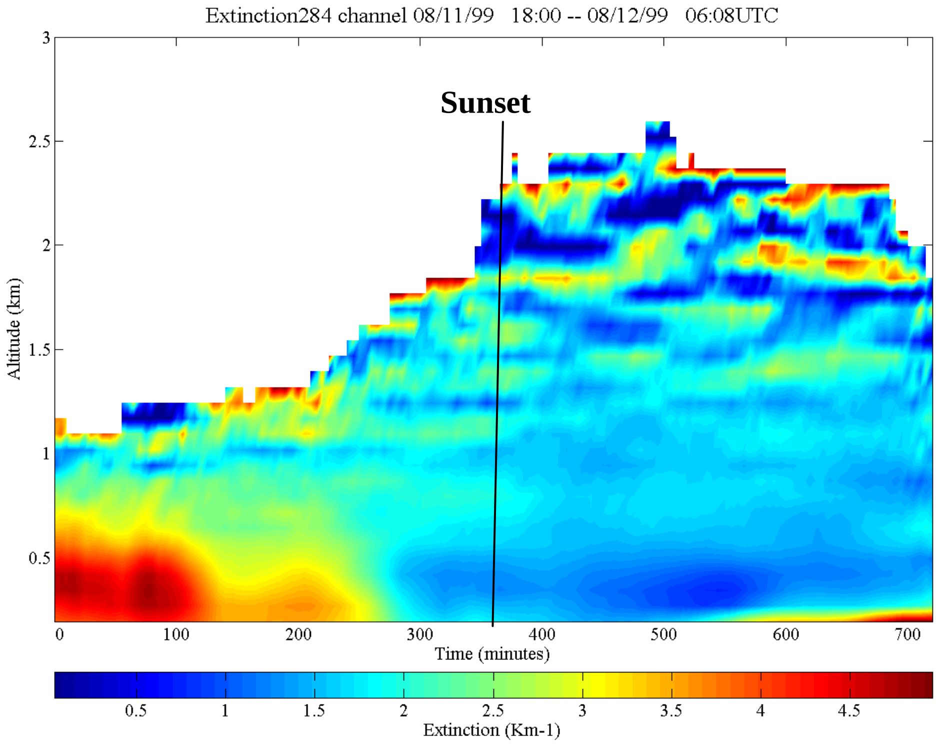

Figure 4-26 Time sequence of extinction at 284 nm obtained on August 11 1999.

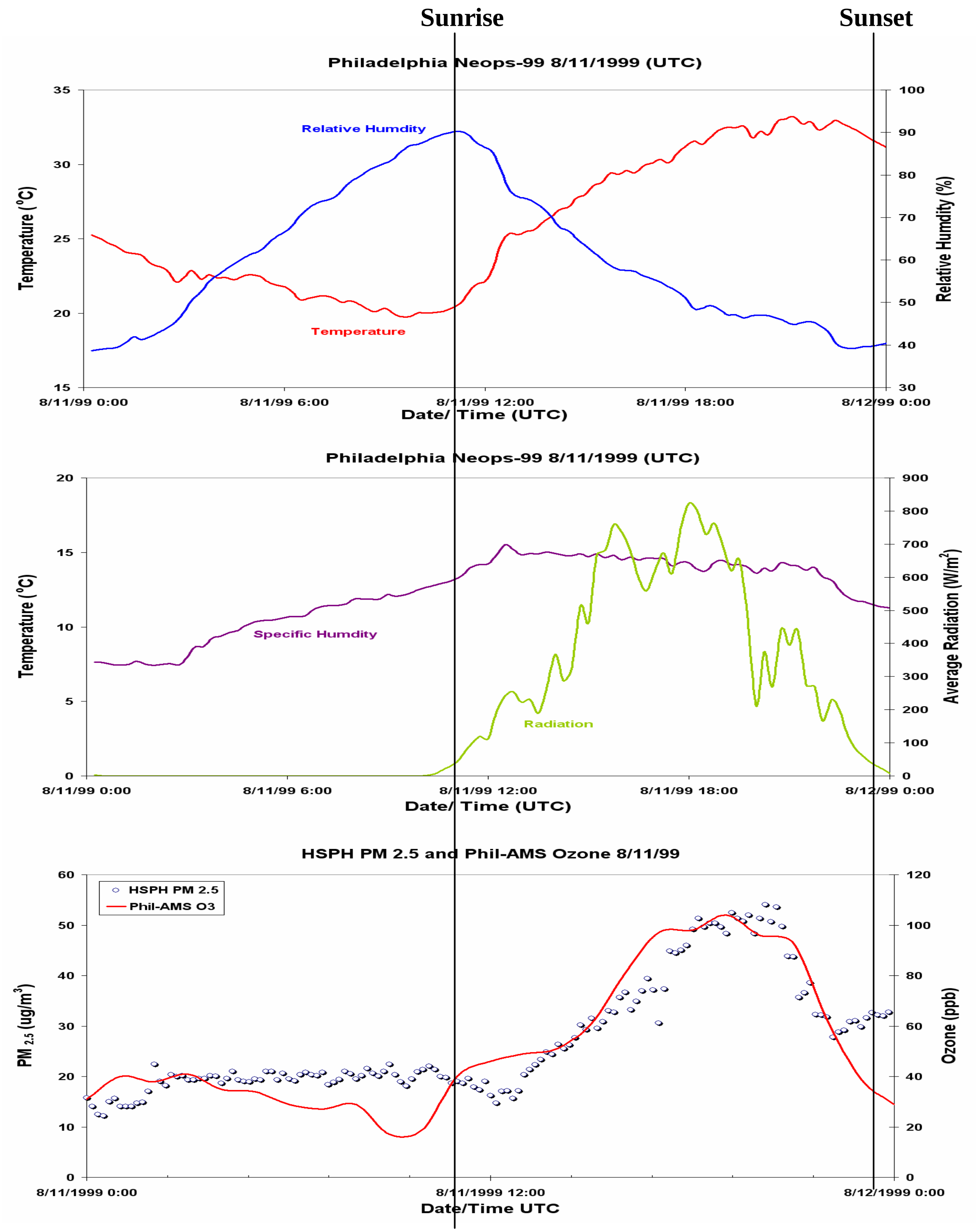

Figure 4-27: Relative humidity, temperature, specific humidity, solar radiation, ozone (Philadelphia AMS) and $PM_{2.5}$ (HSPH) on August 11 1999.

this time, and remain low till the next morning. This suggests that the pollutant concentrations, photochemical processes that generate smog, and the temperature increase controls the optical extinction variations that we observed in many cases during the NEOPS campaigns. An increase in the pollutant concentrations after sunrise results in a corresponding increase in the optical extinction. Similarly, after sunset, the optical extinction values drop following the decrease of pollutant concentrations as the convective turbulent mixing shrinks to a thin nocturnal boundary layer. It is interesting to compare the factors that control the optical extinction during the SCOS and the NEOPS campaigns. During the SCOS campaign an increase of optical extinction was observed after sunset in the nocturnal boundary layer due to the growth of particles by condensation of water and coalescence. It was also observed that the optical extinction values decreased after sunrise as the particles reduced in size due to increasing temperatures and mixing of the moisture into the growing boundary layer. On the other hand, the optical extinction during the NEOPS campaigns was controlled more by pollutant concentrations and showed an increase in values after sunrise and decreased values after sunset

4.3 Relative Humidity Control of Extinction and Visibility

Another interesting observation during the NEOPS campaigns was the effect of the deliquescence relative humidity (DRH) on optical extinction. Aerosols found in the atmosphere are typically composed of hygroscopic inorganic salts, such as sulfates, nitrates or chlorides in either pure or mixed form. These inorganic salts usually undergo a phase transformation from a solid particle to a saline droplet spontaneously when the relative humidity reaches a value called the deliquescence relative humidity. At the DRH, water vapor dissolves the solid particle in a process known as deliquescence to form a saturated aqueous droplet. As the relative humidity continues to increase, the water will continue to condense on to the droplet, causing the particle to grow further while maintaining equilibrium with the surrounding water vapor. When the relative humidity decreases to low values of relative humidity called the efflorescence relative humidity

(ERH), the saline droplet will evaporate, expelling all of its water content, and eventually crystallize. The DRH is dependent on the chemical composition of the particle as well as on the temperature [*Seinfeld and Pandis, 1998; Tang, 1980; Tang and Munkelwitz, 1993*]. Figure 4-28 shows the change in particle size based on changes of the relative humidity. The figure represents the change as a ratio of the particle size at a particular value of RH to its dry particle size. We see that at lower values of relative humidity the change in the particle size relative to its dry particle size is not large. However, as the relative humidity increases beyond the DRH of a particular salt, the ratio begins to increase drastically as water vapor begins to condense on to the particles causing them to grow in size. In the North-East United States the DRH value is about 75-80% for most of the salts present in the atmosphere.

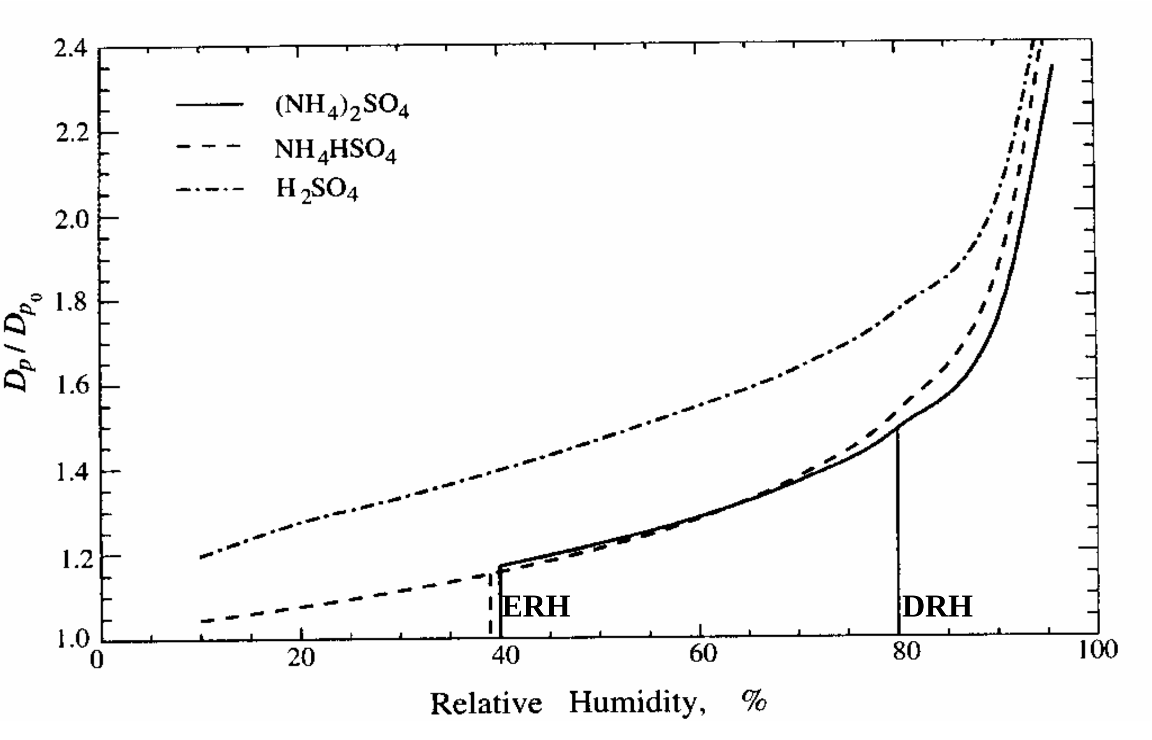

Figure 4-28: Particle growth based on relative humidity changes [Seinfeld and Pandis, 1998].

The increase in the particle size due to DRH is important in understanding the optical extinction measurements at the UV and visible wavelengths; particularly for particles in the accumulation mode that are most easily studied by the lidar. Hence, as the accumulation mode particles begin to grow because water vapor condenses onto them, the extinction coefficients show a rapid increase in values. This increase in optical extinction as the relative humidity exceeded the DRH was observed in many cases during the NEOPS campaigns. Figure 4-26 and Figure 4-29 show the optical extinction measurements obtained during the early morning hours of August 12 1999 at wavelengths of 284 nm and 530 nm respectively. We observe the presence of a fog layer forming close to the surface, within the first 100 m, at around 0300 UTC in the 284 nm extinction. This fog layer becomes visible in the 530 nm extinction plot at around 0500 UTC as the particles grow to a larger size. Figure 4-30 shows the surface measurements of the relative humidity as well as surface measurements of the UV and visible extinction during this time periods. We see that once the relative humidity crosses the DRH point the extinction values in the UV begin to jump from a value around 1.5 km^{-1} to a value around 5 km^{-1}. This jump in UV extinction values occurs because once the particle begins to grow larger and becomes a size that approaches the scale of the UV wavelength, the extinction efficiency increases to a maximum value and hence the extinction coefficient drastically increases in value.

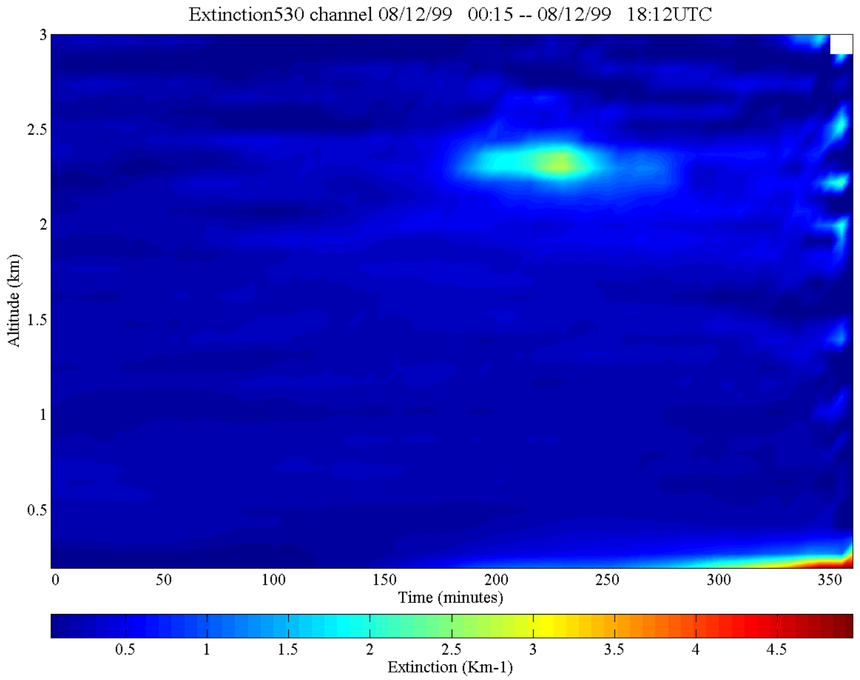

Figure 4-29: Time sequence of extinction at 530 nm obtained on August 12, 1999.

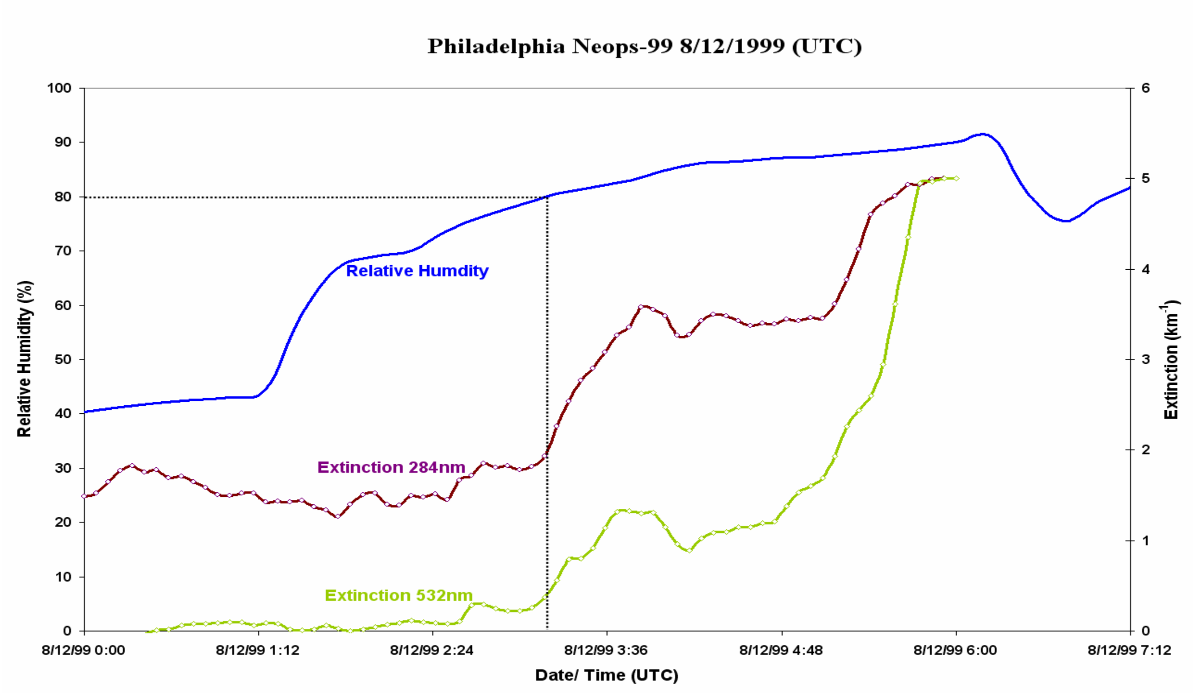

Figure 4-30: Surface measurements of relative humidity, UV and visible extinction on August 12 1999.

Similarly, the visible extinction also increases from a value of 1.5 km^{-1} to a value around 5 km^{-1}. We also observe from Figure 4-30 that during the early part of the fog formation, the UV extinction is greater than the visible extinction indicating that smaller particles dominate the size distribution. As the fog matures during the night the ultraviolet and the visible extinction both reach a value close to 5 km^{-1} (ratio equals 1 for the extinction at the two wavelengths) indicating that the particles have grown large enough that any further change in the particle size affects both wavelengths simultaneously (i.e. on the order of 5 μm). The data on the decrease in extinction once the relative humidity drops below the DRH were not available on this night and hence that analysis was not performed in this case. However, a similar analysis was done by Li (2004) for a case on July 4 1999 shown in Figure 4-31. Here we see the corresponding increase of the 284 nm extinction with the relative humidity as well as the decrease in extinction values once the relative humidity drops below the DRH. During both the time periods we see the strong control of relative humidity on optical extinction close to the surface.

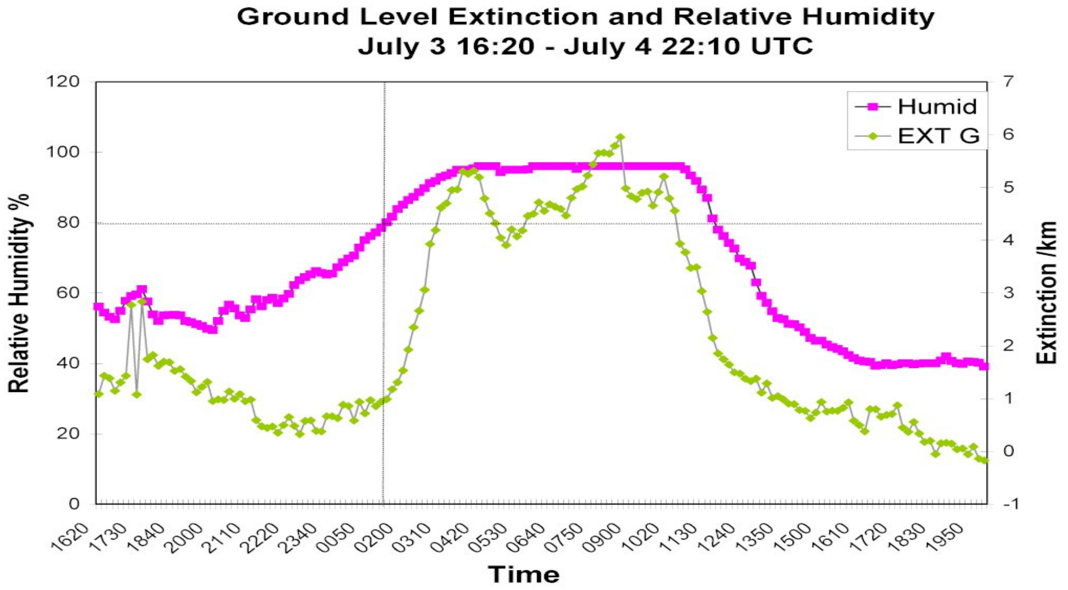

Figure 4-31: Ground level extinction and relative humidity for the time period 07/03/99 16:20 – 07/04/99 22:00 UTC [*Li, 2004*].

The control of the DRH on the optical extinction was also observed during the winter study of 2005. The main objective of this project was to investigate air quality issues during the winter season 2004-2005 at the Baxter Water Treatment Plant in northeast Philadelphia and to study the differences between summer and winter conditions. Data was collected using a Doppler wind profiling radar, Radio Acoustic Sounding System (RASS), a 10-meter instrumented meteorological tower, ozone analyzer, DustTrak aerosol monitor, and three-wavelength nephelometer; all of which were operated at the site of the Baxter Water Treatment Plant in northeast Philadelphia during the winter months from January to March. Airborne particulate matter measurements of $PM_{2.5}$ and PM_{10} were made using two DustTrak optical scatterometers and a nephelometer, together with a surface ozone analyzer.

During the 2004-2005 campaign the direct measurements of the optical extinction were not made. We use the visibility measurements and the data obtained from the nephelometer to show the DRH control on the optical extinction during this period. Reduced visibility, which occurs as a result of the scattering and absorption of light by particles and gases in the atmosphere, is used to further investigate the optical extinction.

A reduced visibility corresponds to a high optical extinction coefficient value and vice versa. While all small particles absorb and several gaseous pollutants impair visibility, sulfates are usually considered to cause the most light-scattering among pollutants in the northeast. Sulfates and nitrates, which are the dominant aerosols in the northeast U.S., have their threshold of deliquescence at relative humidity values of about 80%. Figure 4-32 shows an example of the rise and fall in visibility corresponding to the relative humidity transitions, through the threshold of deliquescence taken during the winter study. We can clearly see the strong correlation that exists between visibility and deliquescence relative humidity during this periods.

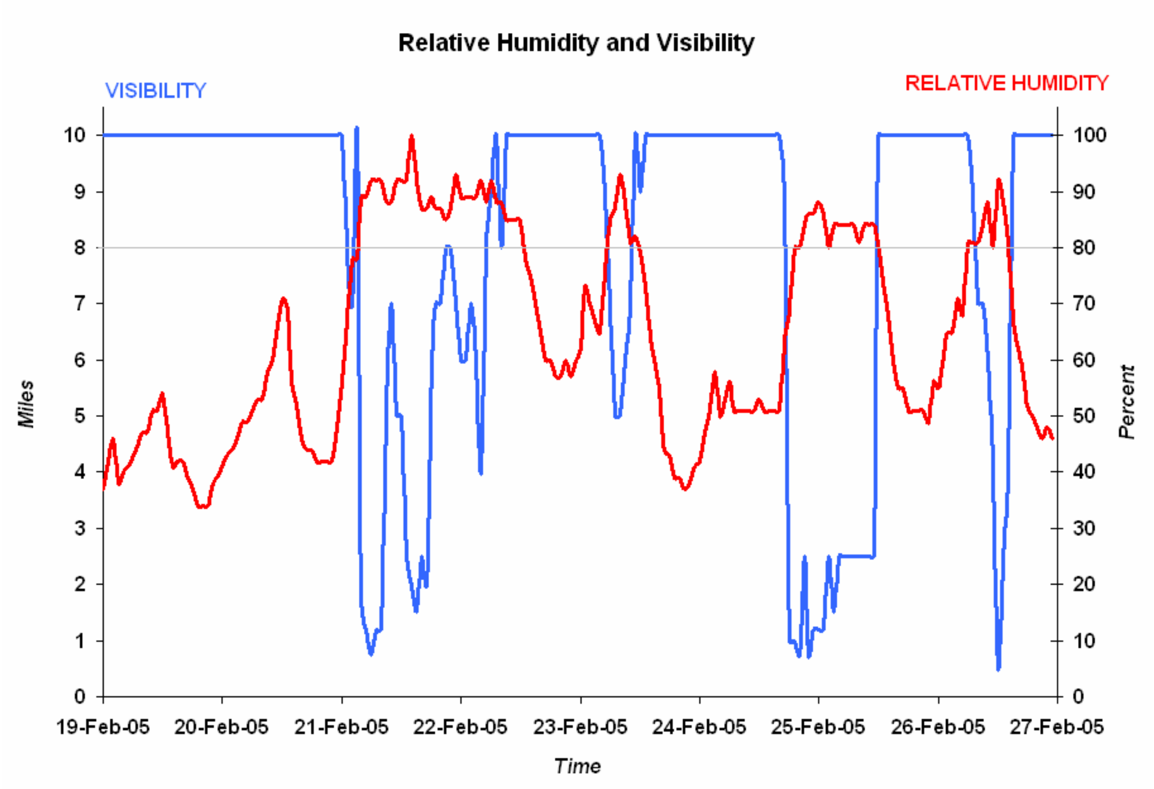

Figure 4-32: Relative humidity and visibility obtained during the time period 02/19/05 – 2/26/05 showing the dependence of the visibility on the DRH.

During the winter study we observed several cases where the visibility reduced drastically as the relative humidity increased past the deliquescence point, where the particles grew in size. The measurements show that during the winter period reduced visibility mostly occurred at those times when the relative humidity increased to values higher that the deliquescence point; showing a strong correlation of the particle to grow from absorption of water vapor once the RH passes the DRH value. Figure 4-33 (a) and (b) show the visibility, relative humidity, $PM_{2.5}$, and Angstrom exponent variations from January 11-15, 2005. We can see on January 11 2005 at about 0000 UTC that the visibility drops to about 5 miles as the RH increases beyond 85% (indicated by a blue line in Figure 4-33). The visibility increases for a short period after this as PM concentrations fall at the surface, but drops drastically as the PM concentrations climb at around 1100 UTC. The Angstrom exponent is calculated by using the total scattering coefficients from the nephelometer at the three wavelengths and provides information on particle size variation. An increase in the Angstrom exponent corresponds to a decrease in particle size while a decrease in the exponent corresponds to an increase in the particle size. We observe at around 1100 UTC that the exponent value drops from 2 to 1 as particles begin to increase in size due to the uptake of water. The visibility remains low until midday on January 13 2005 and rises again only when the RH goes below the deliquescence point. At this time the RH and temperature dropped as the winds changed to a northerly flow at the surface bringing in dryer and cooler air. The PM concentrations also fell drastically as the air-mass arrived, while the Angstrom exponent shows that larger size particles were brought in by the air-mass as the exponent values drop from 1.5 to 0.2. The relationship between increasing RH and reducing visibility is also seen on January 14 as the deliquescence threshold is reached. During the winter study there were 17 periods when the visibility dropped and all these cases were tied in with an increase in RH. Future analyses of this data with an in-depth look at PM concentrations, particle size and optical extinction variation with the deliquescence relative humidity will enable us to better understand this relationship.

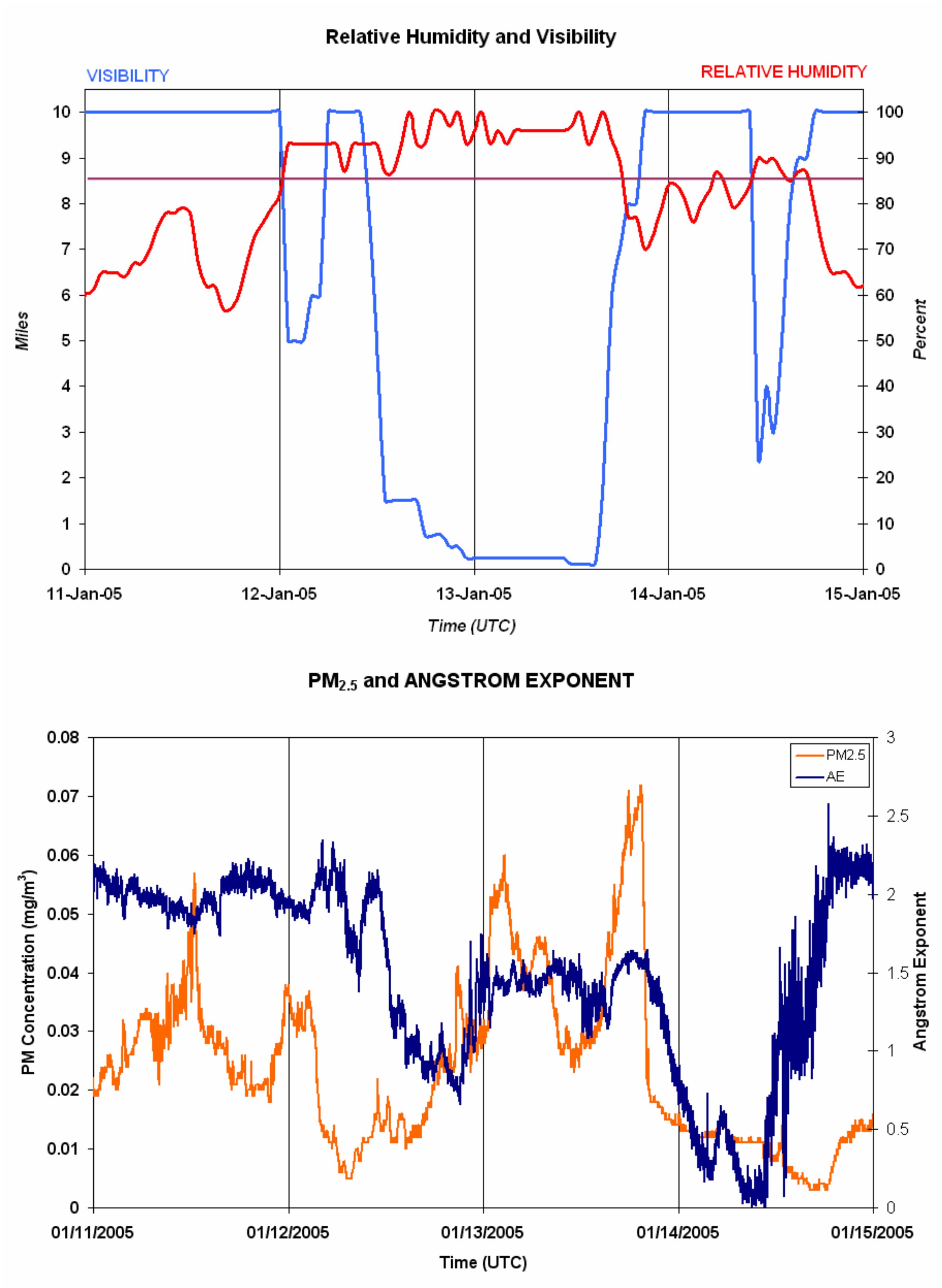

Figure 4-33: Relative humidity, visibility, $PM_{2.5}$ and angstrom exponent variations calculated using the 3-wavelength nephelometer total scattering coefficients for the time period 01/11/05 – 01/15/05.

4.4 Optical Extinction Analysis of Cloud Structures and Pollution Plumes

The LAPS optical extinction at different wavelengths is used in this section to examine the differences between the measurements of cloud structures and pollution plumes. We use the extinction ratio analysis technique along with theoretical simulations to understand the differences that particle growth and air pollutant concentration increases have on the extinction coefficient, as well as on the extinction coefficient ratios at different wavelengths.

Figure 4-34 shows the time sequence plots of the extinction coefficients obtained on July 11 1999 during the NEOPS campaign at Philadelphia. From the time sequence plots we see the optical extinction increasing at various times indicating clouds advecting past the lidar beam. We observe a peak in extinction at the altitude where the cloud is present (~2 km) between 0230 and 0300 UTC. We analyzed the extinction ratio during this time period and compared it to model simulations. Figure 4-35 shows a 30 minute integration profile of the extinction coefficients at the UV and the visible wavelengths as well as a profile of the ratio of the extinction coefficients at the two wavelengths. The extinction coefficients during this period follow a similar trend to that described in section 4.1. In the layer closest to the surface, relatively large particles dominate the extinction as indicated by higher ratio of the extinction coefficients. Smaller particles dominate the region between 500 m and 1.5 km, and then increase in size with increasing height. The higher layer near 2 km shows a cloud where the extinction coefficients lose their wavelength dependence and exhibit values associated with the presence of larger sized cloud particles. The ratio of the extinction coefficients reaches a value of about 0.7 inside the cloud. Comparing this value with the Mie theory simulation of section 4.1 we can conclude that the mean size of the particles in that region is greater than about 0.3 microns. This analysis inside a cloud region also agrees with the theoretical simulation of extinction coefficients calculated for some of the size distributions found in the atmosphere as given in Table 4-1.

Figure 4-36 shows a model simulation of the extinction coefficients for cumulus cloud and haze models calculated using the size distribution parameters shown in Table

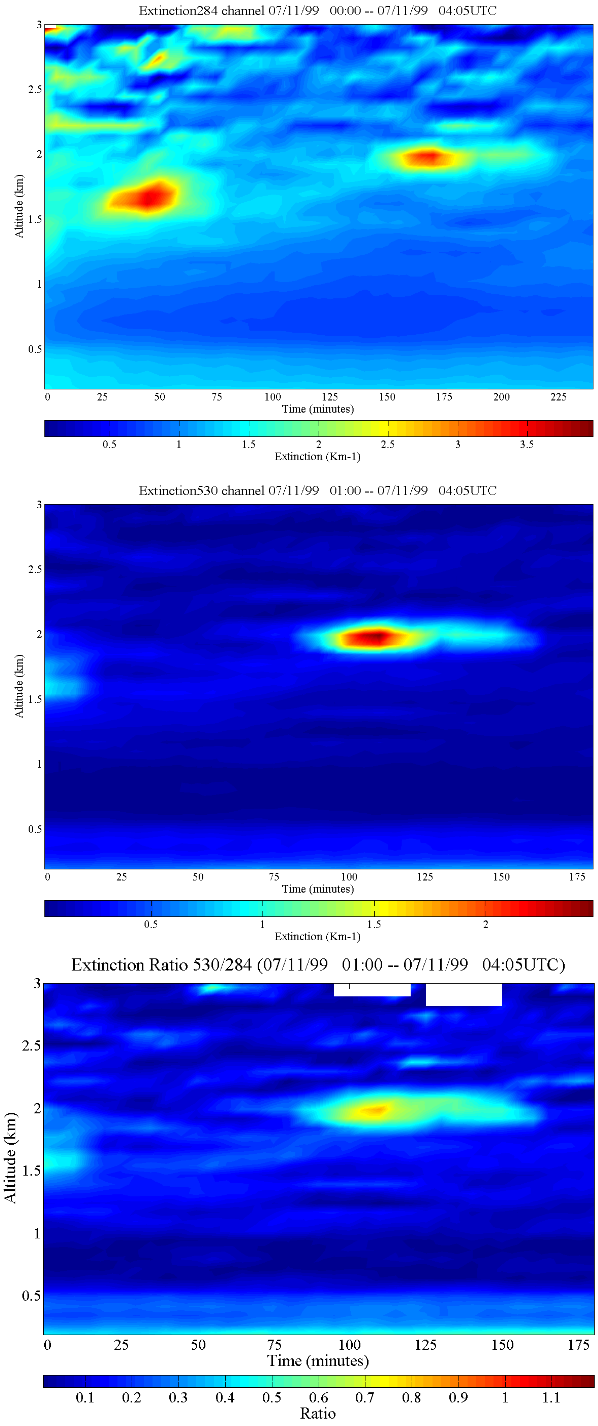
Extinction284 channel 07/11/99 00:00 -- 07/11/99 04:05UTC

Extinction530 channel 07/11/99 01:00 -- 07/11/99 04:05UTC

Extinction Ratio 530/284 (07/11/99 01:00 -- 07/11/99 04:05UTC)

Figure 4-34: Time sequence plots of extinction coefficients on July11 1999. (a) 284 nm (b) 530 nm (c) extinction ratio at the two wavelengths.

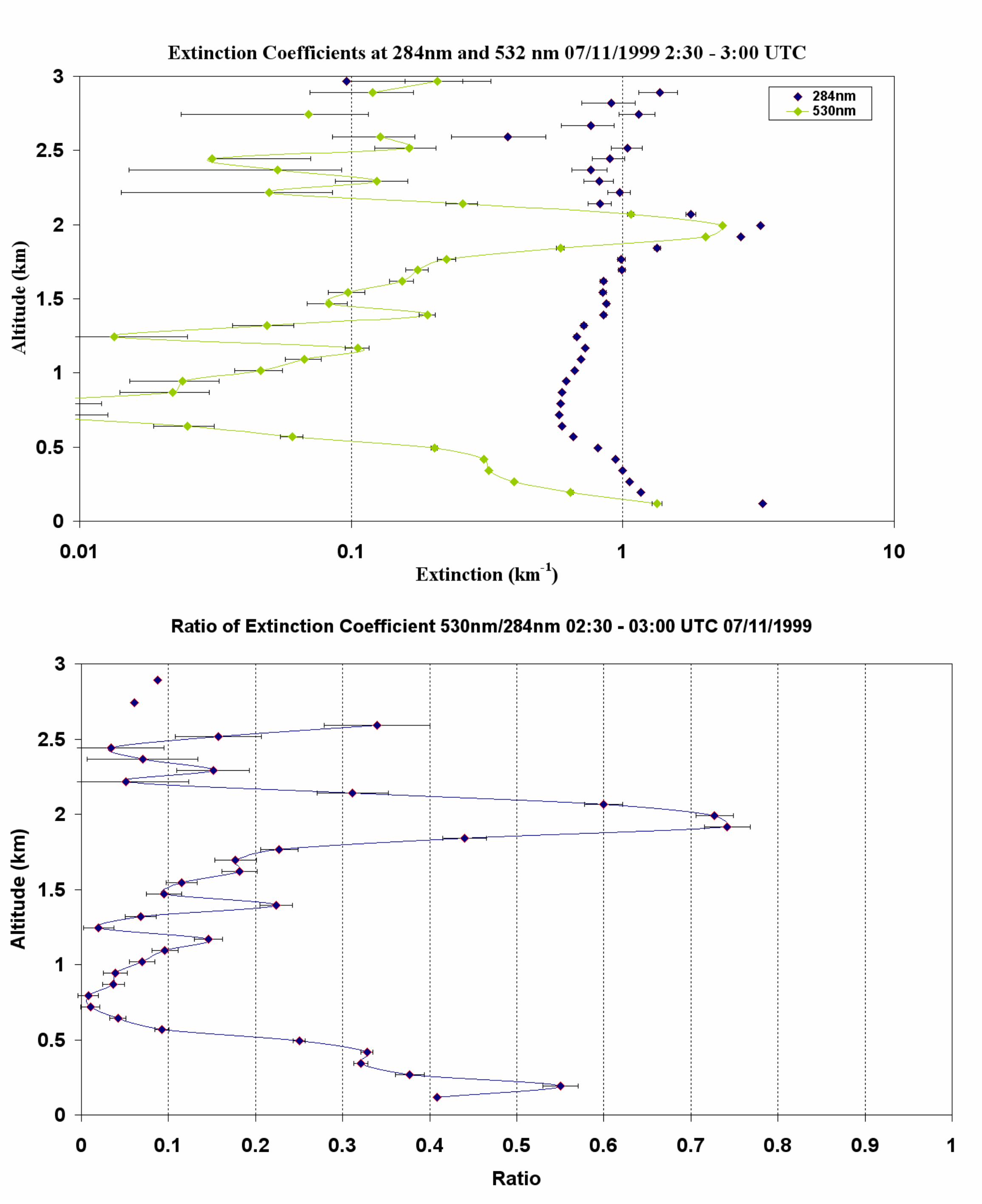

Figure 4-35: 30 minute integration profile of the extinction coefficients at 284 nm and 530 nm as well as a profile of the ratio of the extinction coefficients at the two wavelengths.

4-1. The size distribution was calculated using the modified gamma distribution and the extinction coefficients, based on Mie theory, were obtained for a number density of 100 particles per cm^{-3}. The cumulus cloud model can be used to generate various other cloud models found in the atmosphere by changing some of the parameters of the gamma distribution. Changing the number concentration of particles by some factor for any given model will cause the corresponding curve to be shifted vertically upward or downward without any change in shape. The simulation of the cloud and haze models shows the wavelength dependence of the extinction coefficient over the wavelengths from 0.1 to 17 µm. The wavelength dependence of the extinction coefficients of the model matches accurately with our observations of the UV and visible extinction coefficients obtained from the LAPS lidar on July 11 1999. The haze curves are similar to some of the fog conditions that we observe in the lower atmosphere and the wavelength dependence is

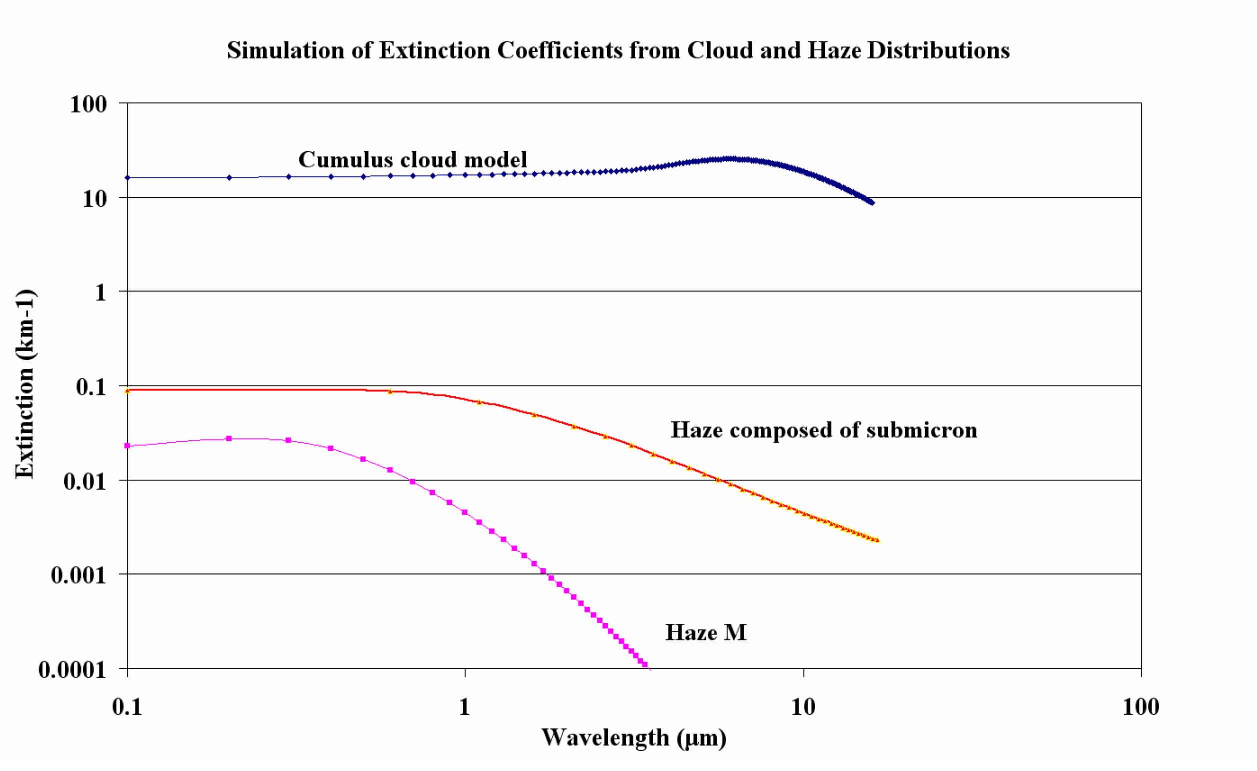

Figure 4-36: Simulation of extinction coefficients based on Mie theory for various size distribution types seen in the atmosphere

similar to observations during the early hours of August 12 1999 (see Figure 4-30).

To compare the preceding case on 11 July 1999, which showed the wavelength dependence of extinction coefficients observed in cloud structures, with measurements of a pollution plume we chose a time period when very high pollutant concentrations were observed. Figure 4-37 shows time sequence plots of optical extinction on July 22 1999 when a pollution plume was advecting through the lidar beam (at 0.5 km). Figure 4-38 shows the water vapor mixing ratio and the ozone concentrations measured simultaneously with the extinction using the Raman lidar. During this time ozone

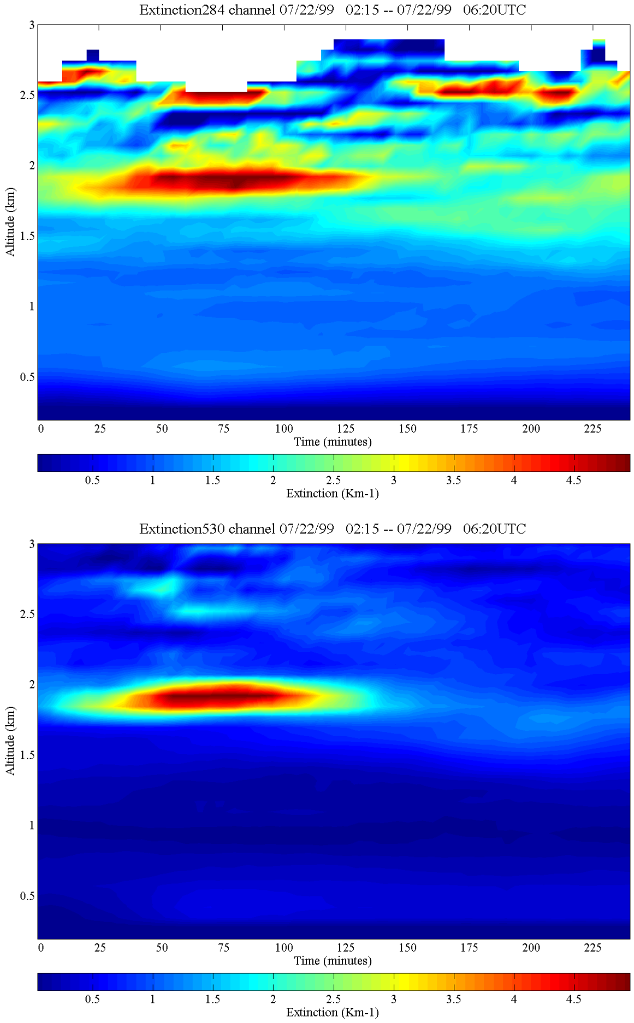

Figure 4-37**:** Time sequence plot of optical extinction on July 22 1999 when a pollution plume was observed over the nocturnal boundar layer.

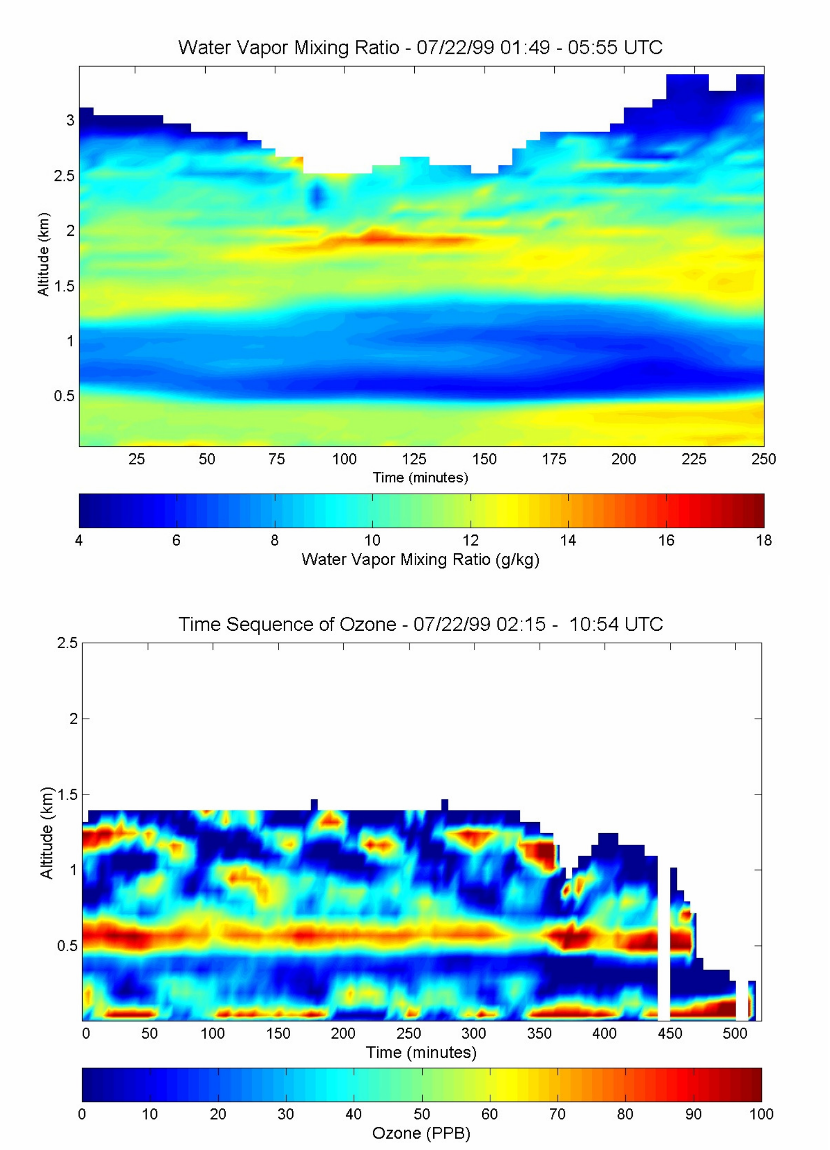

Figure 4-38: Time sequence plot of water vapor and ozone concentration on July 22 1999 when high ozone concentrations were observed in the dry layer above the nocturnal boundary layer.

concentrations of 100 ppb were observed in the region above the nocturnal boundary layer. We see from the water vapor plot that the boundary layer collapses to the lower 400 m once the convective activity and turbulent mixing ceases after sunset. The layer above the nocturnal boundary layer is filled with rich concentration of pollutants from the previous day, and allows us investigate the effects that these particles have on the extinction values. During the NEOPS campaigns, we observed on a number of occasions that plumes not only contained ozone but were also rich in other pollutants and precursor materials. The time sequence plots of the visible and UV extinction coefficients, in Figure 4-37, do not show much change in their values in the region of high pollutant concentrations. Figure 4-39 shows a 30 minute integrated profile of the ratio of the extinction coefficients obtained 0230 UTC - 0300 UTC. The ratio of the extinction coefficients indicates a distribution of smaller particles in the atmosphere below 1 km. The ratio also reduces with altitude between 0.5 km and 1.5 km indicating scattering dominated by many small scatterers. We see from the water vapor plot in Figure 4-38 that the layer between 0.5 km and 1.5 km appears to have low water vapor mixing ratio compared to the layers above and below it. We have observed in a number of occasions that such pollution plumes were characterized by a dry layer associated with them. Without high water vapor concentrations in the atmosphere particle growth is inhibited

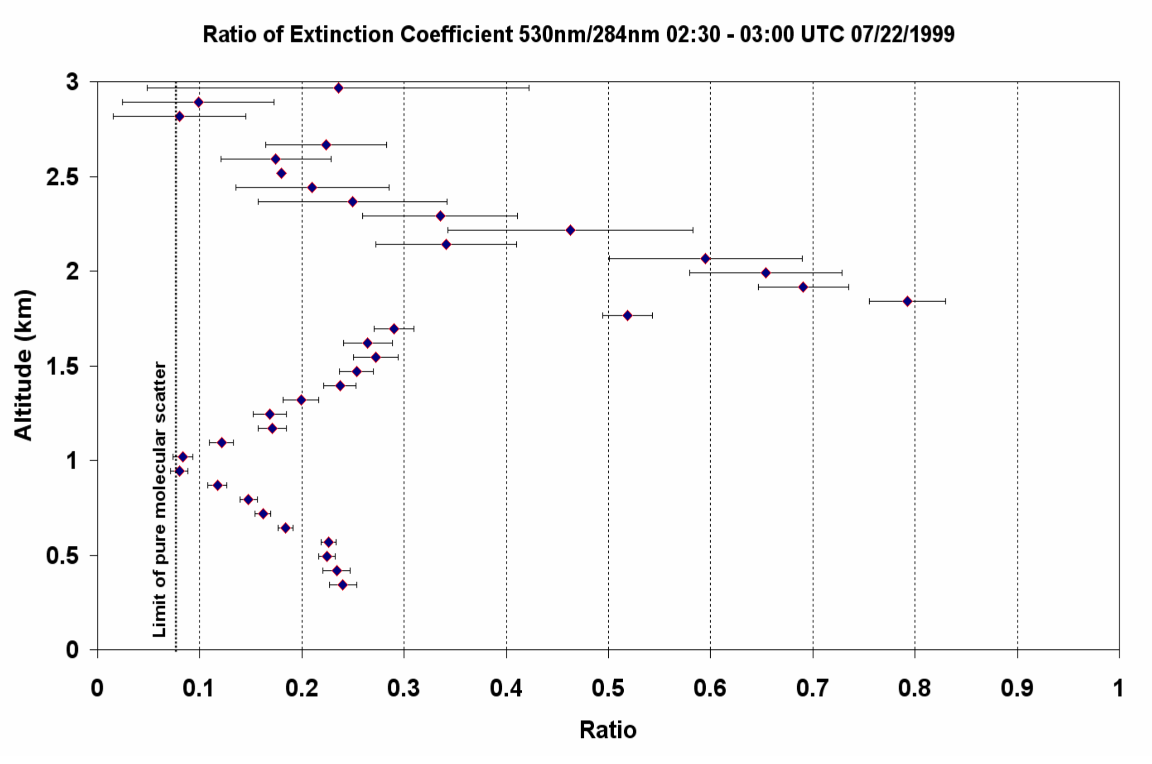

Figure 4-39: Ratio of extinction coefficient of 530 nm to 284 nm at 0300- 0330 UTC on July 22 1999.

even when the hygroscopic air pollution nuclei are present in large numbers. This may be the reason that the ratio of the extinction coefficients decrease in this region even though the particle concentration remains high. We also see an increasing ratio from above 1.5 km where we observe the presence of a cloud. As expected, the extinction coefficients lose their wavelength dependence once they enter the region of the cloud. We also observe the cloud in a layer associated with higher water vapor mixing ratio in Figure 4-38. We find that while the ratio of the of the extinction coefficients increases as we enter a cloud region, due to large cloud particles, pollution plumes are typically characterized by a constant or decreasing ratio profile in the region due to the smaller sized particles. In pollution plumes, the changes in the value of the extinction coefficient are governed by the number density of scatterers, and appear to be independent of wavelength. The change in the extinction coefficient in clouds, however, depends on the particle size of the scatterer, and is wavelength dependent for accumulation mode particles.

A simulation like that shown in Figure 4-36 has been examined for optical extinction coefficients from different concentrations of $PM_{2.5}$. The relationship that existed between the extinction coefficients at different wavelengths and PM concentrations was studied. The simulation results are also found to be in close agreement with observations in the pollution plume. Figure 4-40 shows the extinction coefficients calculated for different particle concentrations of $PM_{2.5}$ at 284 nm and 530 nm, and their corresponding ratios as a function of particle size. The model assumes only spherical non-absorbing particles and varies the input of the size and number density. The different curves in Figure 4-40 correspond to calculations with different particle concentrations between from 10 $\mu g/m^3$ to 100 $\mu g/m^3$ for each of the wavelengths. Both the UV and the visible wavelengths show the particle extinction increasing at higher concentrations, with the extinction maximum occurring when the particle size is closer to half the wavelength of the radiation. We also observe higher extinction coefficients for smaller particles than for the larger particles for the two wavelengths, as the particular mass is distributed in smaller particles which are more effective scatterers than the larger particles made up from the same mass of the particulate matter. The ratio of the

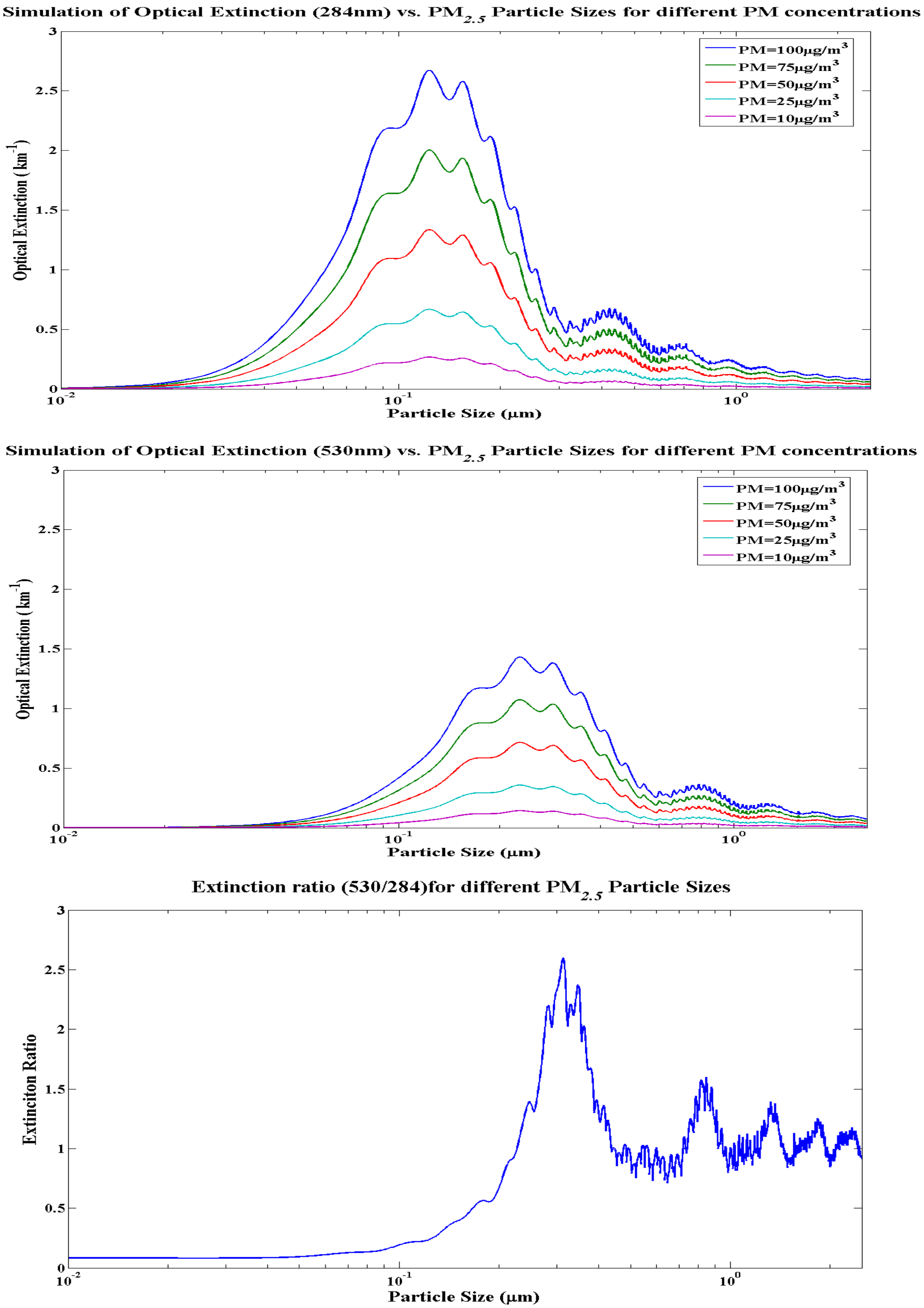

Figure 4-40: Simulation of optical extinction coefficients and their corresponding ratios for different concentrations of $PM_{2.5}$.

extinction coefficients is shown in the last plot of Figure 4-40 and a single line is shown as the ratio, which begins to flattens out to a value of 1 for particle sizes beyond $(\lambda_1 + \lambda_2)/2$, and results in the same curve independent of the amount of material suspended in the particles. The number density at both the wavelengths is the same and hence the ratio depends only on the efficiency of the scatterers at any particular size. The simulation results are also found to be in close agreement with observations of the extinction ratio in the pollution plume, where the extinction ratio remained small due to scattering from small particles in the atmosphere.

4.5 Visibility and Transmission calculated using Lidar Data

Visibility is broadly defined as the degree of transmission through the atmosphere or the distance from an object that allows a minimum or threshold contrast between the object and some appropriate background [*Malm, 1979*]. Independent of the amount of illumination (as long as it is not a dark environment) an object will become invisible if less than 2% of the light reaching the observer (or detector) is scattered from the object. Once the contrast value becomes lower than this threshold contrast the object becomes indistinguishable from the background. Low visibility values are caused by particle scattering in the atmosphere, which causes the decrease in contrast of distant objects. Visibility is typically described by visual range (the greatest distance that a large, dark object can be seen), or by the light extinction coefficient. The visual range is greatly influenced by the air quality and hence airborne particle distributions have a significant influence on the visibility. Visibility is reduced by the absorption and scattering of light as it propagates through both gases and particles. However, light scattering by particles is the most important processes responsible for visibility degradation. The typical visual range, compared to the clean molecular atmosphere, is around 50-67 % in the western United States and 20 % in eastern United States [*Albritton et al., 1998*]. Knowledge of visibility is important to quantify the cleanliness of the atmosphere in terms of the presence of airborne particulate matter. The visual range is also important to aviation as well as in many outdoor activities.

In order to calculate the visual range one must know or calculate the spatial variation of the path radiance, apparent target radiance, spatial variation of the attenuation coefficient etc. Since the lidar provides a measure of the spatial variation of the attenuation coefficient we can use this to obtain a better and continuous measurement through any atmospheric path, in contrast to point measurements. The visual range of a black object against the sky is calculated by using the following contrast equation [*Middleton, 1952*]

$$c = \frac{\left[\int_0^R \beta \exp\left(-\int_0^x \sigma dr \right) dx - \int_0^\infty \beta \exp\left(-\int_0^x \sigma dr \right) dx \right]}{\int_0^\infty \beta \exp\left(-\int_0^x \sigma dr \right) dx} \qquad [4.2]$$

where β is the scattering coefficient of the atmospheric volume seen by the eye at a distance *x* and σ is the extinction coefficient. In a simpler form, we can define the contrast in luminance as

$$c = \frac{B - B'}{B'} \qquad [4.3]$$

where the luminance of the object is B and that of its background is B'. Depending on the brightness of the object compared to its background the contrast can take values from -1 to very large positive values. To determine the reduction in contrast we also define the inherent contrast, having luminance's B_0 and B_0', and apparent contrast at a distance R, having luminance's B_R and B_R'. As we move further away from the object, which has an inherent contrast c_0, the apparent contrast c_R, decreases in an exponential manner given by

$$c_R = c_0 e^{-\sigma R} \qquad [4.4]$$

until at some value ε, the minimal contrast value, below which the object will be invisible at any range. The visibility distance R is the distance for which, the contrast difference in the intensity of the object scattered radiation is ~2% of the total radiation observed, ε = 0.02. The value of 2% was obtained from values determined from many tests by subjects viewing under a large range of illumination conditions. In order to include some order of safety, the values for aviation are increased to the range of 0.05 to 0.055 for determining visibility. Taking logarithms on both sides and expressing the distance R at which ε = 0.02 to be the visual range V, we obtain,

$$V = \frac{1}{\sigma} \ln \left| \frac{c_0}{0.02} \right| \qquad [4.5]$$

Considering the case of a simple black object, $c_0 = -1$, we obtain Koschmeider's equation for visual range,

$$V = \frac{3.912}{\sigma} \qquad [4.6]$$

This equation directly relates the extinction coefficient to the visual range. The intrinsic luminance of a colored object will depend on that of the surroundings and consequently its visual range will vary with its position relative to the sun. For a black object, on the other hand, the intrinsic luminance is always zero, no matter what the incident light, and its visual range is independent of the azimuth intensity of the sky. The use of a black object is a practical one, thus black objects are typically chosen as markers for the estimation of the visual range. In lidar measurements it becomes necessary to integrate the extinction over the vertical range to find the vertical value of the visual range. It should be noted that two major assumptions are made in the development of Koschmeider's equation: the extinction is constant along the path and that the Earth's curvature can be ignored.

Figure 4-41 shows a calculation of the visual range from the lidar measurements of extinction obtained during the NEOPS campaign on August 17 1999. Figure 4-41 (a) shows a time sequence of optical extinction at 530 nm measured by the LAPS Raman lidar. The optical extinction measured by the lidar is used to determine the visibility shown in Figure 4-41 (b). Low extinction values near the surface indicate regions of clear

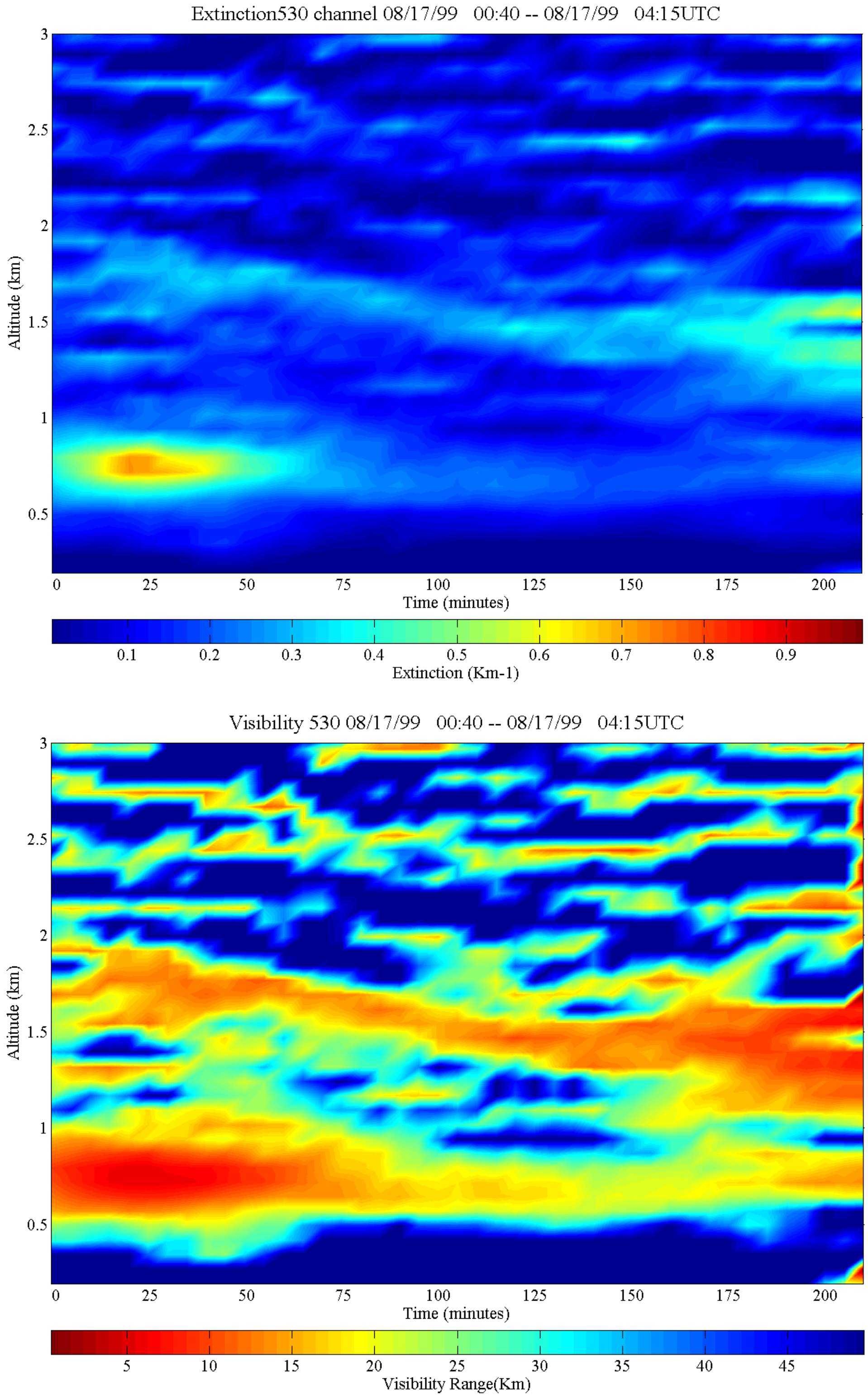

Figure 4-41: (a) Time sequence plot of extinction at 530 nm on August 17 1999. (b) Horizontal visual range calculated during the same period from 530 nm extinction on August 17 1999.

atmosphere with high visibility. Above the surface layer, beyond 0.5 km, we observe regions with higher extinction and corresponding lower visibility. Between 0.5 km and 1 km we observe the presence of a sub-visual cloud that is composed of larger particles than the surrounding layers, and results in lower visibility (< 5 km) in that region.

For cases were extinction measurements are made at wavelengths other than those close to the mid visible a considerable simplification was proposed [*Kruse et al., 1963*]. By taking into account the wavelength where the atmospheric extinction coefficient was calculated, an empirical formula was proposed,

$$V = \frac{3.912}{\sigma(\lambda)}\left[\frac{550}{\lambda}\right]^{q} \text{ km}^{-1} \qquad [4.7]$$

where

$$q = 0.585\, V^{1/3} \quad \text{for } V < 6 \text{ km}$$

$$= 1.3 \text{ otherwise}$$

In the case of measurements made using the LAPS Raman lidar, the extinction calculated at 530 nm can be used to determine the value of q based on the calculated visual range measurements, which then yield measurements of visibility at other wavelengths. Figure 4-42 shows an analysis of the calculation of the visual range from the lidar measurements of extinction from LAPS lidar data obtained during the USNS Sumner tests. Figure 4-42 (a) shows a time sequence of optical extinction measured by the LAPS Raman lidar at 284nm. The optical extinction measured by the lidar was used to determine the visibility shown in Figure 4-42 (b) using the modified equation of Kruse et al. We see the presence of a cloud forming between 1.5 km and 2 km in the extinction data, and this causes a drastic reduction in the horizontal visual range in that region due to the growth of larger particles. Figure 4-42 (c) and (d) show the transmission profiles calculated from the path integrated extinction measurements during the same time period, but along different path angles (pointing relative to the horizon). The white line on the time sequence plot shows the visibility limit or the range at which the path integrated intensity would be reduced to 2% of its initial value.

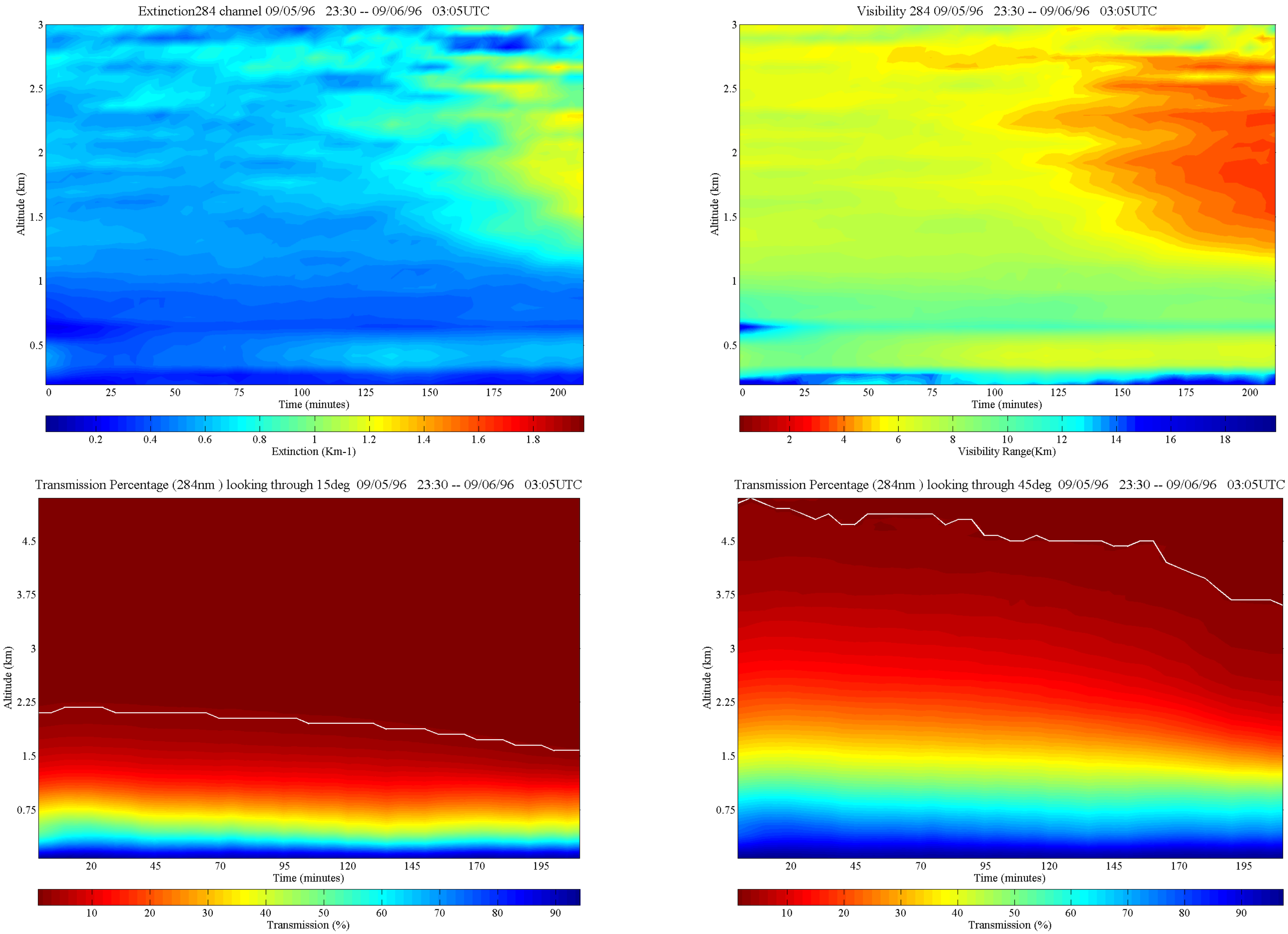

Figure 4-42: (a) Time sequence plot of extinction at 284 nm on Sep 05 1996. (b) Horizontal visual range on Sep 05 1996 (c) Transmission plot on Sep 05 1996 looking down at an angle of 15 degrees (d) Transmission plot on Sep 05 1996 looking down at an angle of 45 degrees.

Chapter 5

Summary and Conclusions

5.1 Summary and Accomplishments

The size-distribution and chemical composition of aerosol particles in the Earth's atmosphere continues to be substantially altered due to increasing anthropogenic emissions from industrial and urban development. This, in turn, has led to changing the properties of clouds such as albedo, number concentrations, and lifetimes, which together are thought to exert a negative radiative forcing on the atmosphere. Since the Earth's atmosphere is not static, but constantly changing, it is critical to work on understanding the various processes that control it. In order to accurately predict future regional and global changes, we must understand the operative physical and chemical processes. For example, to be able to precisely model the formation and dissipation of clouds and their interaction with incoming and outgoing radiation, we need to understand how the increasing concentrations of anthropogenic aerosols alter cloud properties.

Lidar techniques provide a powerful tool to investigate aerosols and clouds. Ground-based lidar techniques have been used to measure aerosol optical parameters for several decades, and these have added greatly to the knowledge of optical properties of clouds. The underlying purpose of this thesis is to examine and improve our knowledge of aerosol and cloud properties based on data obtained from the PSU Raman lidar, by making comparisons with model calculations. The measurements obtained by the PSU LAPS Raman lidar provided an extensive dataset on water vapor, aerosol optical extinction, ozone, and temperature profiles in the troposphere. Datasets obtained in field measurements conducted during several years, and over different regions, using the Raman lidar together with a suite of other instruments, provides the base for this investigation. A summary of our results, analysis, and interpretations are given below; detailed discussions are presented in Chapter 4.

Multi-wavelength Extinction Profiles Show Changing Aerosol Size

We demonstrated the capability of a new technique using the multi-wavelength extinction profiles obtained from the LAPS Raman lidar, along with theoretical simulations of extinction ratios calculated from Mie theory, to provide information on particle size variations along a vertical path. We find that the ratios of the extinction coefficients at the three different wavelengths contain important information on the size of particles in the range of the accumulation mode. The accumulation mode particles fall in the range where the transition occurs between haze and cloud formation; hence, the extinction ratio from different wavelengths reveals changes in CCN particle size in the range of 50 nm to 0.5 μm. Examples taken from three different field campaigns demonstrate that changes in the size of the cloud particles during the different stages of growth and dissipation are observed in the multi-wavelength aerosol extinction using this technique. We also show the relationship that exists between particle size increase/decrease in cloud regions. This analysis shows the relationship between extinction coefficients and the changes in relative humidity. Measurements show strong control of the relative humidity values near the deliquescence values point on the aerosol growth characteristics. As particles grow in size from water condensation, the extinction and the visible/ultraviolet extinction ratio measurements show simultaneous increases with increasing relative humidity. Similarly, we find that when the relative humidity in the region decreases, the resulting distribution of smaller particles leads to a drop in the magnitude of the extinction and in the extinction ratio.

However, in order to obtain quantitative measurements of any of the size parameters that describe the exact distribution of particles it is necessary to have additional information. If other parameters related to the size distribution are obtained as simultaneous measurements it is possible to construct models to accurately describe the change in cloud condensation nuclei particle size using multi-wavelength optical extinction measurements.

This study was restricted to examining particle size changes from 50 nm to 0.5 μm due to the range of the wavelengths used to obtain the optical extinction data. With the wider spectrum, using ultraviolet, visible, and infrared wavelength lidars available nowadays, we have the opportunity to investigate the full range of particle sizes by selecting appropriate wavelengths. Simultaneous optical extinction measurements in the ultraviolet, visible, mid-wave infrared, and long-wave infrared wavelengths would allow the extinction ratio technique to investigate changes during the various stages of particle size change in clouds and other plumes. For example, by simultaneously making optical extinction measurements from the ultraviolet (284 nm) to the infrared (10.6 μm), and by choosing appropriate wavelengths in the visible and mid-wave infrared we can use the extinction ratio technique to observe changes in particle sizes from 50 nm to 10 μm.

Markedly Different Processes Control Extinction in Different Regions

We compared the factors that controlled the optical extinction during the summer months, between the western US (SCOS campaign), and the northeast US (NEOPS campaigns), and found different processes to control the increases or decreases in the optical extinction values in the lower boundary layer. Our results show that during the SCOS campaign an increase of optical extinction was observed after sunset in the nocturnal boundary layer, which is due to the growth of particles by condensation of water and coalescence as the regions cools and is cut off from vertical mixing that normally stirs the daytime atmosphere. It was also observed that the optical extinction values decreased after sunrise as the particles reduced in size due to increasing temperatures and mixing transfer of heat from convective mixing of the growing boundary layer. On the other hand, the optical extinction during the NEOPS campaigns was controlled more by pollutant concentrations and smog photochemistry; also it showed an increase in values after sunrise associated with upward mixing of water evaporated from the dew at dawn, and decreased values after sunset.

Aerosol Growth Rate Dependence on Deliquescence Point

We found the deliquescence relative humidity (DRH) has a strong control on the optical extinction and visibility. The optical extinction values increased drastically once the relative humidity values increased to values above the DRH and showed decreases once the relative humidity dropped below the DRH. We also examined several sets of data during the winter study where the visibility reduced drastically as the relative humidity increased past the deliquescence point and the particles began to grow in size. Our results during the winter period show that reduced visibility occurred mostly at those times when the relative humidity increased to values higher that the deliquescence point. During the winter study there were 17 periods when the visibility dropped, and all these cases were associated with a corresponding increase in relative humidity values. Future investigations measuring simultaneous PM concentrations, particle size changes, optical extinction variations, and visibility along with the changes in humidity should enable us to better understand the details of this relationship.

Extinction Analysis in Cloud Structures and Pollution Plumes

We used theoretical simulations along with field measurements of extinction coefficients at the different wavelengths to study the relationships between particle growth, pollutant concentration, and extinction coefficient, as well as on the extinction coefficient ratios. We found that while the ratio of the extinction coefficients increases as we enter a cloud region, due to large cloud particles, pollution plumes are typically characterized by a constant or decreasing ratio profiles in the region due to the presence of larger number and smaller sizes of particles. The change in the values of the extinction coefficients in pollution plumes is governed by the number density of scatterers. Small particles found in these plumes exhibit extinction ratios that are relatively constant through the region because the change in the extinction coefficient due to changes in number density of same size particles is proportional for all wavelengths. The extinction coefficients in and around cloud regions depend on the particle size of the scatterers. Measurements of the extinction ratio are wavelength dependent for particles smaller than the wavelengths. As we enter a cloud region the extinction coefficient ratio increases as the scattering from larger particles is more. For particles sizes larger than the wavelength, the extinction coefficients become equal to each other, independent of wavelength, and the extinction coefficient ratio approaches unity. These results also closely agree with model simulation results of the optical extinction coefficients from different concentrations of $PM_{2.5}$. The use of two Raman lidars in the same region, or a single instrument scanning different locations would permit unambiguous determination of the growth and dissipation rates of clouds.

Raman Lidar Measurements Define Visibility

We also demonstrated the capability of the Raman lidar to make continuous measurements of the visibility and transmission on any atmospheric path based upon analysis from optical extinction measurements.

Although much progress has been made over the past few decades to understand and simulate features of the global atmosphere, mainly due to the advancement in active remote sensing instruments, there are still many questions that remain unanswered; these leave simulation models incomplete. By incorporating a global distribution of several lidar stations to correlate with satellite measurements, we can collect high resolution information of the vertical structure of the lower atmosphere and describe its various processes to improve models for a better understanding of the Earth's atmosphere. Lidar based techniques have been shown to offer several advantages over other techniques, and they have the ability to provide good spatial and temporal resolution at a specific location. Lidar measurements made at different global stations, together with satellite measurements of large scale features, will provide the key for answering significant questions, and lead to better understanding the Earth's climatic processes.

REFERENCES

Albrecht B. A. (1989). “Aerosols, cloud microphysics, and fractional cloudiness.” Science 245, 1227-1230.

Andrew T. Young (1982). “Rayleigh Scattering.” Physics Today 35, 42–48.

Ansmann, A., M. Riebesell and C. Weitkamp (1990). “Measurement of Atmospheric Aerosol Extinction Profiles with a Raman Lidar.” Opt. Lett., 15, 746-748.

Ansmann, A, I. Mattis, D. Müller, U. Wandinger, D. Althausen, and R. Damoah (2005), "Ice formation in Saharan dust over Europe observed with temperature/humidity/aerosol Raman lidar," J. Geophys. Res. Vol. 110, D18S12.

Arking, A. (1991). “The Radiative Effects of Clouds and their Impact on Climate.” Bull. Amer. Meteor. Soc., 72, 795-813.

Arya, S. P. (1999). “Air Pollution Meteorology and Dispersion.” Oxford University Press, Oxford.

Balsiger, F., Paul T. Haris, and C. Russell Philbrick (1996). “Lower Tropospheric Temperature Measurements Using a Rotational Raman Lidar.” Optical Instruments for Weather Forecasting, SPIE Vol. 2832, 53 – 60.

A. Berk, G. P. Anderson, P. K. Acharya, L. S. Bernstein, L. Muratov, J. Lee, M. Fox, S. M. Adler-Golden, J. H. Chetwynd, Jr., M. L. Hoke, R. B. Lockwood, J. A. Gardner, T. W. Cooley, C. C. Borel, P. E. Lewis, and E. P. Shettle (2006).” MODTRAN5: 2006 Update.” Proc. SPIE Vol. 6233, 62331F.

Bohren, C. F., and D. R. Huffman (1983). “Absorption and Scattering of Light by Small Particles.” Wiley-Interscience, New York.

Bohren, C. F. (1992). “On the Absurdity and Inadvisability of Calling Particles Mie Scatterers.” Optics and Photonics News, February, 1992, 18-19.

CCSP (2006). “Temperature Trends in the Lower Atmosphere: Steps for Understanding and Reconciling Differences.” Thomas R. Karl, Susan J. Hassol, Christopher D. Miller, and William L. Murray, editors. A Report by the Climate Change Science Program and the Subcommittee on Global Change Research, Washington, DC.

California Air Resources Board (CARB) (1999). “Southern California Ozone Study–NARSTO.” URL http://www.arb.ca.gov/research/scos/scos.htm

Chadha, Ginnipal S. (2001). “Optical Systems Design for ALAPS Lidar Instrument,” Master of Science Thesis for Penn State University, Department of Electrical Engineering.

Chahine, M. T. (1992). “The hydrological cycle and its influence on climate.” Nature, 359, 373-380.

Charlock, T. P. and V. Ramanathan (1985). “The Albedo Field and Cloud Radiative Forcing Produced by a General Circulation Model with Internally Generated Cloud Optics.” J. Atmos. Sci., 42, 1408-1429.

Charlson, R. J., J. E. Lovelock, M. O. Andrea, and S. G. Warren (1987). “Oceanic Phytoplankton, Atmospheric Sulphur, Cloud Albedo and Climate.” Nature, 326, 655-661.

Charlson, R. J., and J. Heintzenberg (1995).“Aerosols as a Cause of Uncertainty in Climate Forecasts.” Aerosol Forcing of Climate, R.J. Charlson and J. Heintzenberg (eds.), John Wiley & Sons, New York.

Committee of the Environmental and Occupational Health Assembly of the American Thoracic Society (1996a). “Health Effects of Outdoor Air Pollution.” American Journal of Respiratory and Critical Care Medicine 153, 3-50.

Committee of the Environmental and Occupational Health Assembly of the American Thoracic Society (1996b). “Health Effects of Outdoor Air Pollution. Part 2.” American Journal of Respiratory and Critical Care Medicine 153, 477-498.

Cooney, J. A. (1968). “Measurements on the Raman component of laser atmospheric backscatter.” Applied Physics Letters, 12, 40-42.

Cooney, J. A. (1970). “Comparisons of Water Vapor Profiles Obtained by Radiosonde and Laser Backscatter.” J. Appl. Meteor., 9, 182 – 184.

Cooney, J. A. (1986). “Lidar Method of Measurement of Atmospheric Extinction and Ozone Profiles.” Applied Optics, 25, 2035-2036.

Deirmendjian, D. (1969). “Electromagnetic Scattering on Spherical Polydispersions.” A report prepared for United States Air Force Project Rand. Rand Corporation, CA.

Dines, W. H. (1917). “The heat balance of the atmosphere.” Quart. J. Roy. Meteor. Soc., 43, 151–158.

Esposito, Steven T. (1999). “Applications and Analysis of Raman Lidar Techniques for Measurements of Ozone and Water Vapor in the Troposphere,” Master of Science Thesis for Penn State University, Department of Electrical Engineering, May.

Fitzgerald, J. W., and P. A. Spyers-Duran (1973). “Changes in Cloud Nucleus Concentration and Cloud Droplet Size Distribution Associated with Pollution from St. Loius.” Journal of Applied Meteorology, 12, 511-516.

Flossmann A. I. and P. Laj (1998). “Aerosols, Gases and Microphysics of Clouds.” Urban Air Pollution to Extra-Solar Planets (ERCA, Vol. 3), C.F. Boutron Ed. (EDP Sciences, Les Ulis) pp. 89-119.

Fouquart, Y., J. C. Buriez, M. Herman, and R. S. Kandel (1990). “The Influence of Clouds on Radiation. A Climate-Modeling Perspective.” Rev. Geophys., 145-166.

Gillespie, J. B., D. A. Ligon, P. M. Pellegrino, N. F. Fell Jr, and N. J. Wood (2002). “Development of a Broadband Lidar System for Remote Determination of Aerosol Size Distributions.” Meas. Sci. Technol., 13, 383-390.

Hansen, J., Mki. Sato, and R. Ruedy (1997). “Radiative Forcing and Climate Response.” J. Geophys. Res., 102, 6831-6864.

Haris, P. A. T. (1995) “Pure Rotational Raman Lidar for Temperature Measurements in the Lower Troposphere.” Ph.D. Dissertation, The Pennsylvania State University.

Hidy, G. M., P. M. Roth, J. M. Hales and R. Scheffe (1998). “Oxidant Pollution And Fine Particles: Issues And Needs.” NARSTO Critical Review Series.

Harrison, E. F., Minnis, P.,Barkstrom, B. R., Ramanathan, V., Cess, R. D., and Gibson, G.G (1990). “Seasonal Variation of Cloud Radiative Forcing Derived from the Earth Radiation Budget Experiment.” Journal of Geophysical Research, Vol. 95, No. D11, pp. 18,687 - 18,703.

Hartmann, D. (1993). “Radiative Effects of Cloud on Climate. Aerosol Cloud-Climate Interactions.” P. V. Hobbs Ed., Academic Press, 151-173.

Hobbs, P. V., H. Harrison and E. Robinson (1974). “Atmospheric effects of pollutants.” Science, 183, 909-915.

Hobbs, P. V. (1993). Aerosol Cloud Interactions, in Aerosol-Cloud-Climate Interactions.” edited by P. V. Hobbs, pp 33-37, Elsevier, New York.

Houghton T., Ding Y., Griggs D.J., Noguer M., van der Linden P.J. and Xiaosu D. Eds. (2001). “Climate Change 2001: The Scientific Basis.” Cambridge University Press, Cambridge.

Hobbs, P. V. and B. J. Huebert (1996). “Atmospheric Aerosols. A New Focus of the International Global Atmospheric Chemistry Project (IGAC).” IGAC Core Project Office, MIT, Cambridge, Mass.

Hudson, J. G., and S. S. Yum (2001). “Maritime-Continental Drizzle Contrasts in Small Cumuli.” J. Atmos. Sci., 58, 915–926.

Hunt, G. E., R. Kandel, and A. T. Mecherikunnel (1986). “A History of Presatellite Investigations of the Earth’s Radiation Budget.” Rev. Geophys., 24, 351–356.

IPCC (1995). Albritton, D. L., Derwent, R. G., Isaksen, I. S. A., Lal, M. & Wuebbles, D. J. “Climate Change 1994: Radiative Forcing of Climate Change and an Evaluation of the IPCC IS92 Emissions Scenarios.” (eds. Houghton, J. T. et al.) 205−231 (Cambridge Univ. Press).

IPCC. (1996). “Climate Change 1995 – The Science of Climate Change: Contributions of Working Group I to the Second Assessment Report of the Intergovernmental Panel on Climate Change.", J. J. Houghton, L. G. Meiro Filho, B. A. Callander, N. Harris, A. Kattenberg, and K. Maskell Eds., Cambridge University Press, Cambridge, U.K

IPCC. (2001). "Climate Change 2001: The Scientific Basis: Contribution of Working Group I to the Third Assessment Report of the Intergovernmental Panel on Climate Change (Climate Change 2001).", J. T. Houghton, Y. Ding, D. J. Griggs, M. Noguer, P. J. van der Linden, X. Dai, K. Maskell, C. A. Johnson Eds., Cambridge University Press, Cambridge, U.K.

IPCC. (2007). "Climate Change 2007: Working Group I. The Physical Basis of Climate Change.", Cambridge University Press, Cambridge, U.K.

IPCC. (2007). "Climate Change 2007: Working Group I. Impacts, Adaptation and Vulnerability.", Cambridge University Press, Cambridge, U.K.

IPCC. (2007). "Climate Change 2007: Working Group I. Mitigation of Climate Change.", Cambridge University Press, Cambridge, U.K.

Jenness, J.R., D.B. Lysak, Jr., and C.R. Philbrick (1997). "Design of a Lidar Receiver with Fiber-Optic Output." Applied Optics, 36, No. 18, 4278 – 4284.

Johnson, W. (1969). "Lidar Applications in Air-Pollution Research and Control." J. Air. Pollut. Control. Assoc., 19, 176-180.

Kaufman, Y. J., Koren, I., Remer, L. A., Rosenfeld, D., and Rudich, Y. (2005)." The effect of smoke, dust, and pollution aerosol on shallow cloud development over the Atlantic ocean." Proc. Natl. Acad. Sci. USA, 102, 11207-11212.

Kaufman, Y. J, and I. Koren, (2006)." Smoke and Pollution Aerosol Effect on Cloud Cover." Science 313 (5787), 655.

Kiehl, J. T. (1994). “Clouds and Their Effects on the Climate System.” Phys. Today, 47, 36-42.

Kiehl, J. T., and K. E. Trenberth, (1997). Earth's annual global mean energy budget. Bull. Am. Met. Soc., 78, 197-208.

Kirchner, I., G. Stenchikov, H.-F. Graf, A. Robock, and J. Antuna, (1999) “Climate model simulation of winter warming and summer cooling following the 1991 Mount Pinatubo volcanic eruption.” J. Geophys. Res., 104, 19,039-19,055.

Kobayashi, Takao (1987). “Techniques for Laser Remote Sensing of the Environment,” Remote Sensing Reviews, 3, 1 – 56.

Kyle, T. G. (1991). “Atmospheric Transmission, Emission, and Scattering. Oxford.” New York, Pergamon Press.

Lamb, D. (2003). “Cloud Microphysics.” Encyclopedia of Atmospheric Physics, 459-467, Academic Press.

Leonard, D. A. (1967). “Observation of Raman Scattering from the Atmosphere using a Pulsed Nitrogen Ultraviolet Laser.” Nature, Volume 216, Issue 5111, pp. 142-143.

Leonard, D. A., and B. Caputo (1974). “A Single-Ended Atmospheric Transmissometer.” Opt. Eng. 13, 10–14.

Li. G. (2004). “Atmospheric Aerosol and Particle Properties using Lidar.” Doctoral dissertation, Penn State University, Department of Electrical Engineering.

Lohmann, U., G. Tselioudis, and C. Tyler (2000). “Why is the cloud albedo-particle size relationship different in optically thick and optically thin clouds?.” Geophys. Res. Lett. 27, 1099-1102.

Lohmann, U. (2002). “Possible aerosol effects on ice clouds via contact nucleation.” J. Atmos. Sci. 59, 647-656.

Lohmann U. and Feichter J. (2005). “Global indirect aerosol effects: A Review.” Atmospheric Chemistry and Physics, 5, 715-737.

Mason, B. J. (1971). “The Physics of Clouds.” Oxford University Press.

Mattis, I, A. Ansmann, D. Muller, U. Wandinger, and D. Althausen (2004), "Multi-year aerosol observations with dual-wavelength Raman lidar in the framework of EARLINET," Geophys. Res. Letts., 109, D13203.

McCartney, E. J. (1976). “Optics of the Atmosphere Scattering by Molecules and Particles.” John Wiley & Sons, New York, 1976.

Measures, Raymond M. (1984). “Laser Remote Sensing.” Wiley-Interscience, NewYork.

Middleton, W. E. K. (1952). “Vision Throught the Atmosphere.” University of Toronto Press, Toronto.

Melfi, S. H., J. D. Lawrence Jr., and M. P. McCormick, (1969). “Observation of Raman Scattering by Water Vapor in the Atmosphere.” Appl. Phys. Lett., 15, 295 – 297.

Menon, S., V. K. Saxena, P. Durkee, B. N. Wenny and K. Nielsen, (2002). “Role of Sulfate Aerosols in Modifying the Cloud Albedo: A Closure Experiment.” Atmospheric Research, 61(3), 169-187.

Menon S (2004). “Current Uncertainties In Assessing Aerosol Effects On Climate.” Annual Review of Environment and Resources 29(1): 1.

Mie, G. (1908). “Beiträge zur Optik trüber Medien, speziell kolloidaler Metallösungen,” Leipzig, Ann. Phys. 330, 377–445.

Mulik, K. R., G. Li, G. S. Chadha, and C. R. Philbrick (2000). “Evolution of Air Pollution Events Determined from Raman Lidar.” Proceedings of the A&WMA SpecialtyConference and Exhibition, PM2000: Particulate Matter and Health, Charleston, South Carolina, 4ASP2: 11-13, January 24-28.

Mulik, Karoline R. (2000). “Evolution of Ozone and Particulate Matter During Pollution Events Using Raman Lidar.” Master of Science Thesis, Penn State University, Department of Electrical Engineering.

Murphy, J. M., Sexton, D. M. H., Barnett, D. N., Jones, G. S., Webb, M. J., Collins, M. and Stainforth, D. A. (2004). “Quantification of Modelling Uncertainties in a Large Ensemble of Climate Change Simulations.” Nature, 430, 768-772.

NASA Facts Online (1996). “Atmospheric Aerosols: What Are They, and Why Are They So Important.” FS-1996-08-11-LaRC. http://oea.larc.nasa.gov/PAIS/Aerosols.html.

NASA Facts (2005). “The Balance of Power in the Earth-Sun System.” FS-2005-9-074-GSFC.

NASA Goddard Datasets & Images (2005). “GISS Surface Temperature Analysis Global Temperature Trends: 2005 Summation.” http://data.giss.nasa.gov/gistemp/2005/.

National Research Council (NRC). (1996a). “National Science Education Standards.” Washington, DC: National Academy Press.

National Research Council (1998). “The Atmospheric Sciences: Entering the Twenty-First Century.” National Academy Press, Washington, D. C.

National Research Council (2000). “Reconciling Observations of Global Temperature Change.” National Academy Press, Washington, DC, 85 pp.

Novitsky, E. J. and C.R. Philbrick (2005). “Multistatic Lidar Profiling of Urban Atmospheric Aerosols.” JGR Atmospheres, Vol. 110, DO7S11, March 2005.

O’Brien, M. D., T. D. Stevens, and C. R. Philbrick (1996). “Optical Extinction from Raman Lidar Measurements.” Optical Instruments for Weather forecasting, SPIE Proceedings Vol. 2832, 45-52.

Philbrick, C. R. (1994). “Lidar Measurements of Atmospheric Properties.” Atmospheric Propagation and Remote Sensing III, SPIE Vol. 2222, 922-931.

C. R. Philbrick and D. B. Lysak, Jr. (1996). “Lidar Measurements of Meteorological Properties and Profiles of RF Refractivity.” Proceedings of the 1996 Battlespace Atmospherics Conference, Technical Document 2938 NCCOSC RDT&E, pg 595-609.

Philbrick, C. Russell (1998). “Raman Lidar Capability to Measure Tropospheric Properties.” Nineteenth International Laser Radar Conference, NASA Langley Research Center, Hampton, VA, NASA Conf. Publ. 207671, 289- 292.

Philbrick, C. R. (1998). “Investigations of Factors Determining the Occurrence of Ozone and Fine Particles in Northeastern USA.” Measurement of Toxic and Related Air Pollutants - Specialty Conference Cosponsored by the Air and Waste Management Association and the U.S. EPA’s National Exposure Research Lab, 1, 248-260.

Philbrick, C. R., K. R. Mulik, G. Li, G. Chadha, A. Achey, and G. O’Marr (2000). “Data Summary Report for Lidar Measurements of High Latitude Atmospheric Properties for the ARM Program.”

Philbrick, C. R. (2001). "Overview of Raman Lidar Techniques for Air Pollution Measurements.” Lidar Remote Sensing for Industry and Environment Monitoring II, SPIE Vol. 4484, 136 - 150.

Philbrick, C. R., R. D. Clark, P. Koutrakis, G. Allen, J. Lawrence, J. Wolfson, V. Hatch, M. Davey, J. W. Munger, R. Dickerson, B. Doddridge, C. Hogrefe, S. T. Rao, V. Mohnen, I. Zurbenko, S. Porter, P. Georgopoulos, M. Lazaridis, P. Daum, and L. Kleinman (2002). “Investigations of Factors Determining the Occurrence of Ozone and Fine Particles in Northeastern USA.” NEOPS Summary Report. (http://lidar1.ee.psu.edu/neopsWeb/publicSite/narsto-neops/neops.htm).

Philbrick, C. R., R. D. Clark, W. Ryan, P. Hopke, and S. Mcdow (2003). “Processes Controlling Urban Air Pollution in the Northeast: Summer 2002.” Final Report for Commonwealth of Pennsylvania Department of Environmental Protection. (http://lidar1.ee.psu.edu/neopsWeb/publicSite/neopsdep/neopsdep.htm).

Philbrick, C. R., and S. J. Verghese (2005). “Measurement of Boundary Layer Atmospheric Variables and Surface Aerosols over Philadelphia.” Summary report prepared for the Philadelphia Air Management Service.

Pruppacher, H. R., and J. D. Klett (1997). “Microphysics of Clouds and Precipitation.” Kluwer Academic Publishers, Boston.

Quante, M. (2004). “The Role of Clouds in the Climate System.” Journal de Physique, 121, 68 – 86.

Rajan S., S. L. Mathur and C. R. Philbrick (1995). “Analysis of Atmospheric Water Vapor Measurements Using a Raman Lidar.” Proceedings of the IEEE Topical Symposium on Combined Optical-Microwave Earth and Atmosphere Sensing, 109-111.

Ramanathan, V., R. D. Cess, E. F. Harrison, P. Minnis, B. R. Barkstrom, E. Ahmad, and D. Hartmann (1989). “Cloud Radiative Forcing and Climate: Results from the Earth Radiation Budget Experiment.” Science, 243, 57–63.

Ramanathan, V., P. J. Crutzen, J. T. Kiehl and D. Rosenfeld (2001). “Aerosols, Climate, and the Hydrological Cycle.” Science, 294, 2119-2124.

Renaut, D., J. C. Pourny, and R. Capitini (1980). "Daytime Raman-Lidar Measurements of Water Vapor," Opt. Lett. 5, 233.

Rossow, W. B., and Y. C. Zhang (1995). “Calculation of Surface and Top of Atmosphere Radiative Fluxes from Physical Quantities Based on ISCCP Data Sets 2. Validation and First Results.” J. Geophys. Res., 100, 1167–1197.

Rossow, W. B. and R. A. Schiffer (1999). “Advances in Understanding Clouds from ISCCP.” Bull Am. Meteor. Soc., 80, 2261-2287.

Rotstayn, L. D. and J. E. Penner (2001). “Indirect Aerosol Forcing, Quasi-Forcing, and Climate Response. J. Climate, 14, 2960-2975.

Salby, Murry L. (1996). “Fundamentals of Atmospheric Physics.” Academic Press.

Seinfeld J. H., and S. N. Pandis (1998). “Atmospheric Chemistry and Physics: From Air Pollution to Climate Change.” John Wiley & Sons, NewYork.

Seinfeld, J. H., and R. H. Flagan (1999). “Aerosol-cloud interactions and indirect forcing.” IGACtivites Newsletter, 17.

Sherwood, S. (2002). “A Microphysical Connection among Biomass Burning, Cumulus Clouds, and Stratospheric Moisture.” Science 295, 1272-1275.

Slick, C.T. (2002). “Lower Tropospheric Temperature Measurement Scheme for an Advanced Lidar Atmospheric Profiling System.” Master of Science Thesis for Penn State University, Department of Electrical Engineering.

Stenchikov, Georgiy L., Ingo Kirchner, Alan Robock, Hans-F. Graf, Juan Carlos Antuna, R. G. Grainger, Alyn Lambert, and Larry Thomason, (1998). “Radiative Forcing from the 1991 Mount Pinatubo volcanic eruption.” J. Geophys Res. 103(D12), 13837-13857.

Stephens G. L. (2005). “Cloud Feedbacks in the Climate System: A Critical Review.” Journal of Climate 18(2), 237.

Teller, A. and Z. Levin (2006).” The effects of aerosols on precipitation and dimensions of subtropical clouds: a sensitivity study using a numerical cloud model.” Atmos. Chem. Phys 6, 67-80.

Twomey, S. (1977). "The Influence of Pollution on the Shortwave Albedo of Clouds." Journal of the Atmospheric Sciences 34, 1149-1152.

Van de Hulst, H. C. (1981). “Light Scattering by Small Particles.” New York: Dover.

Vong, R. J. and D. S. Covert (1998). "Simultaneous observations of aerosol and cloud droplet size spectra in marine stratocumulus." Journal of the Atmospheric Sciences, 55(12), 2180-2192.

Young K.C. (1993). “Microphysical Processes in Clouds.” Oxford University Press, NewYork, 1993.

Yu, S. (1996). “CCN-Cloud-Climate Hypothesis: Chemical Role, in Nucleation and Atmospheric Aerosols.” Ed. by M. Kulmala and P. E. Wagner, Elsevier, New York.

Yum, S. S., and J. G. Hudson (2002). “Maritime/Continental Microphysical Contrasts in Startus.” Tellus, Ser. B., 54, 61-73.

Wielicki, B. A., R. D. Cess, M. D. King, D. A. Randall, and E.F. Harrison (1995). “Mission to Planet Earth: Role of Clouds and Radiation in Climate.” Bull. Amer. Meteorol. Soc., 76, 2125-2153.

Whitby, K.T. (1975). “Modeling of Atmospheric Aerosol Particle Size Distributions.” Particle Technology Lab. Publ. 253, University of Minnesota, Minneapolis.

WMO (1995). International Cloud Atlas. Volume I. World Meteorological Organization, Geneva.

WMO (1995). Climate Information and Prediction Services (CLIPS). WMO - No. 832. World Meteorological Organization, Geneva.

Appendix A

Programs to Calculate Extinction Efficiencies from Spherical Particles and Cloud Distributions

****

Plots extinction efficiency and the ratio of the extinction efficiencies as a function of particle radius. Shows regions where extinction is most sensitive.

****

```
clear all;
close all;
j=1
for i = 0.001:.01:100
   [qext284(j), qback284(j)]=scattering(i,.284); % 284 nm
   [qext530(j), qback530(j)]=scattering530(i,.530); % 530 nm
   [qext607(j), qback607(j)]=scattering607(i,.607); % 607 nm
   rad(j)=i;
   j = j + 1;
end
loglog(rad,qext284,rad,qext530,rad,qext607);
xlabel('Radius (\mum)')
ylabel('Extinction Efficiency')
Ratio530_284= qext530./qext284;
Ratio607_284= qext607./qext284;
Ratio607_530= qext607./qext530;
figure;
loglog(rad,Ratio530_284,rad,Ratio607_284,rad,Ratio607_530);
xlabel('Radius (\mum)')
ylabel('Ratio')
```

****

These routines are based upon the program BHMIE found in C. F. Bohren and D. R. Huffman, *Absorption and Scattering of Light by Small Particles*, (Wiley, New York, 1983). Returns the scattering, extinction and backscattering efficiencies for a particular radius and wavelength.

****

```
function [qext, qback]=scattering(rad,wavel);
refmed=1.0; % Refractive index of medium
refre=1.36480866; % Real part of refractive index of sphere
refim=0; % Imaginary part of refractive index of sphere
refrel=refre+refim*i;
x=2*pi*rad*refmed/wavel;
nang=3;
dang=pi/(2*(nang-1));
```

```
[s1,s2,qext,qsca,qback]=bhmie(x,refrel,nang);
s11nor=0.5*(abs(s2(1))^2+abs(s1(1))^2);
nan=nang*2-1;
for j=1:nan
   aj=j;
   s11=0.5*abs(s2(j))*abs(s2(j));
   s11=s11+0.5*abs(s1(j))*abs(s1(j));
   s12=0.5*abs(s2(j))*abs(s2(j));
   s12=s12-0.5*abs(s1(j))*abs(s1(j));;
   pol=-s12/s11;
   s33=real(s2(j)*conj(s1(j)));
   s33=s33/s11;
   s34=imag(s2(j)*conj(s1(j)));
   s34=s34/s11;
   s11=s11/s11nor;
   ang=dang*(aj-1)*57.2928;
end;

function [s1,s2,qext,qsca,qback]=bhmie(x,refrel,nang,s1,s2,qext,qsca,qback)
dx=x;
y=x*refrel;
xstop=x+4*(x^.3333)+2.0;
nstop=xstop;
ymod=abs(y);
nmx=round(max(abs(xstop),abs(ymod))+15);
dang=pi/(2*(nang-1));
%nang
for j=1:nang
   theta(j)=(j-1)*dang;
   amu(j)=cos(theta(j));
end;
d(nmx)=0+0*i;
nn=nmx-1;
for n=1:nn
   rn=nmx-n+1;
   d(nmx-n)=(rn/y)-(1/(d(nmx-n+1)+rn/y));
end;
for j=1:nang
   pi0(j)=0.0;
   pi1(j)=1.0;
end;
nn=2*nang-1;
for j=1:nn
   s1(j)=0.0+0.0*i;
   s2(j)=0.0+0.0*i;
```

```
end;
psi0=cos(dx);
psi1=sin(dx);
chi0=-sin(x);
chi1=cos(x);
apsi0=psi0;
apsi1=psi1;
xi0=apsi0-i*chi0;
xi1=apsi1-i*chi1;
qsca=0.0;
n=1;
while ((n)<nstop)
  dn=n;
  rn=n;
  fn=(2*rn+1)/(rn*(rn+1));
  psi=(2*dn-1)*psi1/dx-psi0;
  apsi=psi;
  chi=(2*dn-1)*chi1/x-chi0;
  xi=apsi-i*chi;
  an=(d(n)/refrel+rn/x)*apsi-apsi1;
  an=an/((d(n)/refrel+rn/x)*xi-xi1); %134
  bn=(refrel*d(n)+rn/x)*apsi-apsi1;
  bn=bn/((refrel*d(n)+rn/x)*xi-xi1);
  qsca=qsca+(2*rn+1)*(abs(an)*abs(an)+abs(bn)*abs(bn));
  for j=1:nang
    jj=2*nang-j;
    PI(j)=pi1(j);
    tau(j)=rn*amu(j)*PI(j)-(rn+1)*pi0(j);
    p=(-1)^(n-1);%142
    s1(j)=s1(j)+fn*(an*PI(j)+bn*tau(j));
    t=(-1)^n;
    s2(j)=s2(j)+fn*(an*tau(j)+bn*PI(j));
    if j==jj
    else
      s1(jj)=s1(jj)+fn*(an*PI(j)*p+bn*tau(j)*t);
      s2(jj)=s2(jj)+fn*(an*tau(j)*t+bn*PI(j)*p);
    end;%149
  end;
  psi0=psi1;
  psi1=psi;
  apsi1=psi1;
  chi0=chi1;
  chi1=chi;
  xi1=apsi1-i*chi1;
  n=n+1;
```

```
    rn=n;
    for j=1:nang
        pi1(j)=((2*rn-1)/(rn-1))*amu(j)*PI(j);
        pi1(j)=pi1(j)-rn*pi0(j)/(rn-1);
        pi0(j)=PI(j);
    end;
end;
qsca=(2/(x*x))*qsca; % Scattering efficiency
qext=(4/(x*x))*real(s1(1)); % Extinction efficiency
qback=(4/(x*x))*abs(s1(2*nang-1))*abs(s1(2*nang-1)); % Backscattering efficiency
```

****

Appendix B

Program to Calculate Extinction Ratio using LAPS data

****

This program calculates the extinction ratio for data obtained by the LAPS Raman lidar at two wavelengths. The raw data is passed into the function. Program originally created by Homer Li. Correction and changes made to the algorithm by Sachin Verghese. This program can also be used to plot a time sequence of the extinction ratio plots using the pcolor command in MATLAB.

****

```
function extRatioPlot(data)
% Rayleigh correction
To = data(1,10);
Po = data(1,12);
data = rayleigh(data, To, Po, -7);
month = data(1,1);
day = data(1,2);
year = data(1,3)
hour = data(1,4);
minutes = data(1,5);
intime = data(1,6);
data = data(2:length(data(:,1)),:);
alt=data(:,1);
% 3: 607nm; 5: 530 nm;  7: 284 nm;
Sig530=data(:,5);
Sig607=data(:,3);
Sig284=data(:,7);
Std530=sqrt(Sig530);
Std607=sqrt(Sig607);
Std284=sqrt(Sig284);
%Range Correct signal
for i=1:70
   SigCor530(i)=Sig530(i)*alt(i)*alt(i);
   SigCor607(i)=Sig607(i)*alt(i)*alt(i);
   SigCor284(i)=Sig284(i)*alt(i)*alt(i);
   StdCor530(i)=Std530(i)*alt(i)*alt(i);
   StdCor607(i)=Std607(i)*alt(i)*alt(i);
   StdCor284(i)=Std284(i)*alt(i)*alt(i);
end;


%-------- Using Calculated Form Factor Values --------------------------
for i=1:70
```

```
   MFA(i)=1;
end;
%sumner form factor
if (year==96)
   MFA(1:10)=[600 180 23 7.2 3.35 1.95 1.4 1.14 1.06 1.02];
end;
%scos form factor
if (year==97)
   MFA(1:7)=[25 5. 2.1 1.45 1.14 1.05 1.02];
end
%Alaska Form factor
if ((year==98) & (month < 6))
   MFA(1:12)=[22000 988.5 78.3 12.97 4.54 2.365 1.644 1.332 1.186 1.099 1.047 1.021];
end;

%Philly 98 form factor
if ((year==98) & (month > 6))
   MFA(1)=2200;
   MFA(2)=83;
   MFA(3)=15.5;
   MFA(4)=5.47;
   MFA(5)=2.76;
   MFA(6)=1.885;
   MFA(7)=1.462;
   MFA(8)=1.263;
   MFA(9)=1.127;
   MFA(10)=1.072;
   MFA(11)=1.026;
   MFA(12)=1.012;
end;

%Philly 99 form factor
if (year ==99)
   if (((month == 7)& (day<18)) | (month==6))
      MFA(1)=80000;
      MFA(2)=475;
      MFA(3)=30;
      MFA(4)=7.7;
      MFA(5)=3.48;
      MFA(6)=2.06;
      MFA(7)=1.49;
      MFA(8)=1.24;
      MFA(9)=1.12;
      MFA(10)=1.05;
      MFA(11)=1.02;
```

```
        MFA(12)=1.005;
    else
        MFA(1)=48000;
        MFA(2)=305;
        MFA(3)=20.8;
        MFA(4)=5.7;
        MFA(5)=2.71;
        MFA(6)=1.75;
        MFA(7)=1.39;
        MFA(8)=1.192;
        MFA(9)=1.102;
        MFA(10)=1.046;
        MFA(11)=1.02;
        MFA(12)=1.0;
    end;
end;

% Phil 2001 form factor
if (year ==2001)
    if ((day < 20) & (month==7))
        MFA(1)=10;
        MFA(2)=4000;
        MFA(3)=262;
        MFA(4)=27.5;
        MFA(5)=7.25;
        MFA(6)=3.;
        MFA(7)=1.7;
        MFA(8)=1.14;
        MFA(9)=1.03;
        MFA(10)=1.0;

    else
        MFA(1)=10;
        MFA(2)=2000;
        MFA(3)=340;
        MFA(4)=31;
        MFA(5)=7.0;
        MFA(6)=2.85;
        MFA(7)=1.6;
        MFA(8)=1.14;
        MFA(9)=1.03;
        MFA(10)=1.0;
    end;
end;
%Phil 2002 form factor
```

```
if (year == 2002)
   MFA(1)=10;
   MFA(2)=15;
   MFA(3)=4;
   MFA(4)=2;
   MFA(5)=1.32;
   MFA(6)=1.15;
   MFA(7)=1.02;
   MFA(8)=1.;
   MFA(9)=1.00;
   MFA(10)=1.0;
end;

for i=1:70
   SigCor530(i)=SigCor530(i)*MFA(i);
   SigCor607(i)=SigCor607(i)*MFA(i);
   SigCor284(i)=SigCor284(i)*MFA(i);
   StdCor530(i)=StdCor530(i)*MFA(i);
   StdCor607(i)=StdCor607(i)*MFA(i);
   StdCor284(i)=StdCor284(i)*MFA(i);
end;

for j=1:70
   T(j)=To+273-6.85*alt(j);
   Ho(j)=((1.38e-23)*T(j))/(9.81*(4.75e-26));
   P(j)=Po*exp(-alt(j)*1000/Ho(j));
   n(j)=P(j)/((1.38e-23)*T(j))*1e2;  %Number density /m3
end;


ScaleH=n*(SigCor607(4)/n(1));
fid=fopen('9908160045extratioprofile.txt','w');
fprintf(fid,'Alt    Ratio   StdRatio\n');

for i=2:1:69
   ext607(i)=log((SigCor607(i+1)*n(i-1))/(SigCor607(i-1)*n(i+1)))/(-.075*4);
   StdExt607(i)=sqrt(StdCor607(i+1)^2/SigCor607(i+1)^2+StdCor607(i-1)^2/SigCor607(i-
1)^2)/(.075*4);
   ext530(i)=log((SigCor530(i+1))/(SigCor530(i-1)))/(-.075*4);
   ext284(i)=log((SigCor284(i+1)*n(i-1))/(SigCor284(i-1)*n(i+1)))/(-.075*4);
   StdExt284(i)=sqrt(StdCor284(i+1)^2/SigCor284(i+1)^2+StdCor284(i-1)^2/SigCor284(i-
1)^2)/(.075*4);

   if (ext530(i)<0.0 |ext284(i)<0.0)
      ext530(i)= NaN;
```

```
        ext284(i)= NaN;
        StdExt530(i)= NaN;
        StdExt284(i)= NaN;
    else
        StdExt530(i)=sqrt(StdCor530(i+1)^2/SigCor530(i+1)^2+StdCor530(i-
1)^2/SigCor530(i-1)^2)/(.075*4);
    end;
    ratio(i)=1./(ext284(i)./ext530(i));
    stdRatio(i)=ratio(i).*(StdExt530(i)./ext530(i)+StdExt284(i)./ext284(i));
    fprintf(fid,'%14f%14f%14f\n',alt(i),ratio(i),stdRatio(i));
end;
figure
ERRPLOT(alt(2:38),ratio(2:38),stdRatio(2:38));
hold on
axis([0 1 0 3])
fclose(fid)
```

****

Appendix C

Programs to Calculate Visibility and Transmission using LAPS data

```
*************************************************************************
This programs plots the Visibility and Transmission calculated from the LAPS raw data.
*************************************************************************

function tsvis(wav,year,month,day,hour,min,input_num)
max_alt=5; % Maximum altitude to plot
maxval=2; % Maximum value of extinction to plot
smonth=month;
sday=day;
shour=hour;
smin=min;
for i=1:15
   [smonth,sday,shour,smin]=nexttime(smonth,sday,shour,smin);
end;

start=dttitle(smonth,sday,year,shour,smin);
temp_month=month;
temp_day=day;
temp_hour=hour;
temp_min=min;
for i=1:input_num
   c=0;
   for j=1:5
      filename = num2name(temp_month,temp_day,temp_hour,temp_min,1,year)
      [tmonth,tday,thour,tmin] = nexttime(month,day,hour,min);
      filename1 = num2name(tmonth,tday,thour,tmin,1,year)
      if (~exist([filename '.dat'])| ~exist([filename1 '.dat']))
         c=c+1;
      end;
      [temp_month, temp_day, temp_hour, temp_min] = nexttime(temp_month, temp_day,
      temp_hour, temp_min);
   end;

   if c==5
      check_point(i)=0;
   else
      check_point(i)=1;
   end;
end;
clear temp_month;
```

```
clear temp_day;
clear temp_hour;
clear temp_min;


for i=1:input_num
   if check_point(i)==1
      filename = num2name(month,day,hour,min,1,year);
      while ~exist([filename '.dat'])
         [month, day, hour, min] = nexttime(month, day, hour, min);
         filename = num2name(month,day,hour,min,1,year);
      end;
      data=getdata(year,month,day,hour,min,30);
      if data ~= -99;
         [a,b,c]=extfactor_final(data,maxval,wav);

         Alt_vect(:,i)=a(2:69);
         ext_vect(:,i)=b(2:69)';
         dext_vect(:,i)=c(2:69)';
      else
         Alt_vect(:,i)=Alt_vect(:,i-1);
         for j=1:68
            ext_vect(j,i)=0;
            dext_vect(j,i)=0;
         end;

      end;

      for i=1:5
         [month,day,hour,min]=nexttime(month,day,hour,min);
      end
   elseif check_point(i)==0
      Alt_vect(:,i)=Alt_vect(:,i-1);
      for j=1:68
         ext_vect(j,i)=0;
         dext_vect(j,i)=0;
      end;
   end;
end
ext_vect
smonth=month;
sday=day;
shour=hour;
smin=min;
for i=1:15
```

```
   [smonth,sday,shour,smin]=nexttime(smonth,sday,shour,smin);
end;

endt=dttitle(smonth,sday,year,shour,smin);

Alt=Alt_vect;
ext=ext_vect;
stdext=dext_vect;
clear a b c aa bb cc;
a=size(ext);
ext(1:a(1)-1,:)=ext(2:a(1),:);
Alt(1:a(1)-1,:)=Alt(2:a(1),:);

a=size(Alt);
sig_clip=5;
start_alt=1;
if year == 97
   Time_zone = 'PDT';
else
   Time_zone = 'UTC';
end;

if wav == 530
   wavelength = '530';
elseif wav == 284
   wavelength = '284';
else
   wavelength = '607';
end;

%Apply for 284nm
% Vis = 4.87369343./ext;
%Apply fpr 530 nm
Vis = 3.958577./ext;
[rows columns] = size(ext);

newExt(1,:) = ext(1,:);
for (i=1:columns)
   for (j = 2:rows)
      newExt(j,i) = ext(j,i) + newExt(j-1,i);
   end
end
newExt
figure
pcolor(newExt.*0.075);
```

```
shading interp;
figure

for j=1:a(2)-1;
    for i=5:a(1)
        if (ext(i,j)<0)
            ext(i,j)=0.015;
        end;
        if (ext(i,j)>0)
            if ((stdext(i,j) > 5) | (stdext(i,j+1) > 5) | i==a(1) )
                pcolor([j-1 j],[Alt(start_alt:(i-1),j) Alt(start_alt:(i-1),j)],...
                    [Vis(start_alt:(i-1),j) Vis(start_alt:(i-1),j+1)]);
                hold on;
                break; end;
        end
    end;
    for k=i:a(1) ext(k,j)=0; end;
    max_bin=max_alt*900/75;
    max_ext(j)=max(ext(2:max_bin,j));
end
step=5;
%  Plot scos
axis([0 a(2)-1 Alt(1,1) max_alt]);

shading interp;
h1=get(gca,'clim');
set(gca,'clim',[0 20]);
barhan=colorbar('horiz');
axhan=gca;

h=title(['Visibility ', wavelength ,' ', start,' -- ',endt,Time_zone ]);
set(h,'fontname','timesnewroman','fontsize',14)
h=xlabel('Time (minutes)');
set(h,'fontname','timesnewroman','fontsize',12)
h=ylabel('Altitude (km)');
set(h,'fontname','timesnewroman','fontsize',12)
axes(barhan);
h=xlabel('Visibility Range(Km)');
set(h,'fontname','timesnewroman','fontsize',12)
axes(axhan);

%       Set the x axis label to the correct step size
if step ~=1
    h=get(gca,'xticklabel');
    set(gca,'xticklabel',num2str(step.*str2num(h)));
```

```
end

f =[     0         0    0.5625
    0         0    0.6250
    0         0    0.6875
    0         0    0.7500
    0         0    0.8125
    0         0    0.8750
    0         0    0.9375
    0         0    1.0000
    0    0.0625    1.0000
    0    0.1250    1.0000
    0    0.1875    1.0000
    0    0.2500    1.0000
    0    0.3125    1.0000
    0    0.3750    1.0000
    0    0.4375    1.0000
    0    0.5000    1.0000
    0    0.5625    1.0000
    0    0.6250    1.0000
    0    0.6875    1.0000
    0    0.7500    1.0000
    0    0.8125    1.0000
    0    0.8750    1.0000
    0    0.9375    1.0000
    0    1.0000    1.0000
    0.0625    1.0000    0.9375
    0.1250    1.0000    0.8750
    0.1875    1.0000    0.8125
    0.2500    1.0000    0.7500
    0.3125    1.0000    0.6875
    0.3750    1.0000    0.6250
    0.4375    1.0000    0.5625
    0.5000    1.0000    0.5000
    0.5625    1.0000    0.4375
    0.6250    1.0000    0.3750
    0.6875    1.0000    0.3125
    0.7500    1.0000    0.2500
    0.8125    1.0000    0.1875
    0.8750    1.0000    0.1250
    0.9375    1.0000    0.0625
    1.0000    1.0000         0
    1.0000    0.9375         0
    1.0000    0.8750         0
    1.0000    0.8125         0
```

```
    1.0000    0.7500         0
    1.0000    0.6875         0
    1.0000    0.6250         0
    1.0000    0.5625         0
    1.0000    0.5000         0
    1.0000    0.4375         0
    1.0000    0.3750         0
    1.0000    0.3125         0
    1.0000    0.2500         0
    1.0000    0.1875         0
    1.0000    0.1250         0
    1.0000    0.0625         0
    1.0000         0         0
    0.9375         0         0
    0.8750         0         0
    0.8125         0         0
    0.7500         0         0
    0.6875         0         0
    0.6250         0         0
    0.5625         0         0
    0.5000         0         0];

for i = 1:64;
    for j = 1:3;
        invjet((65-i),j)=f(i,j);
    end
end
colormap(invjet);
```

****

Appendix D

List of Participants and Measurements obtained during the NARSTO-NEOPS and NEOPS-DEP Campaigns

August 1998 NARSTO-NE-OPS Campaign

Penn State University - Russell Philbrick
Raman Lidar - Profiles of Specific Humidity, Temperature, Ozone, Optical Extinction (285, 530 and 607 nm)
Millersville University - Richard Clark
Tethered Balloon - 100 m^3 - 10 hr aloft with sensors at surface, 100 m, 200 m, and 300 m AGL
1) Personal Environmental Monitors (PEMS) 4 each - 4 L/min dry PM 10 hr sample
2) Diode laser scatterometer (Dust Traks) 1.7 L/min continuous data
Tethered Balloon - 7 m^3 - up/down scan to 300 m each hour
Meteorological properties: T, D, RH, wind speed and direction 1 m vertical resolution and O$_3$
Surface Measurements - O$_3$ and meteorological data
Meteorological Data Archive - Radar, Satellite Images, Surface Observations, Upper air data, ETA/RUC model output
Harvard School of Public Health - Petros Koutrakis and George Allen
Mass density of particulates: PM1, PM2.5, PM10, aerosol-size, EC/OC, sulfate, nitrate, toxics
Harvard University - Bill Munger
NOy concentrations and fluxes are used to infer the rates for NOx oxidation and deposition.
University of Maryland - Bruce Doddridge and Bill Ryan
Instrumented Aircraft Cessna 170: GPS, Ozone, Carbon Monoxide, temperature, humidity probe
Ozone and PM event forecasting, description of interesting episodes and meteorological modeling
Drexel University - Steve McDow
Organics in PM2.5 with GCMS analysis: non-polar components (alkanes, PAH), acids and diacids.
Polar Organics for GCMS with derivatization using PM10 with composite samples

June-August 1999 NARSTO-NE-OPS Campaign

Penn State University - Russell Philbrick
1) Raman Lidar - Profiles of Specific Humidity, Temperature, Ozone, Optical Extinction (285, 530 and 607 nm)
2) Radar-RASS - Wind velocity, Virtual Temperature
3) 10 m Tower - Temperature, dew point, relative humidity, wind velocity, wind gust, solar flux, atmospheric pressure, precipitation
Millersville University - Richard Clark
Tethered Balloon - 100 m^3 - 10 hr aloft with sensors at surface, 100 m, 200 m, and 300 m AGL

1) Personal Environmental Monitors (PEMS) 4 each - 4 L/min dry PM 10 hr integrated sample
2) Diode laser scatterometer (DustTraks) 1.7 L/min continuous data
3) VOC - Micro-orifice vacuum canister at surface and at 300 meters, 10 hour sample with GC/MS lab analysis

Tethered Balloon - 7 m^3 - up/down scan to 300 m each hour
1) Meteorological properties: T, D, RH, wind speed and direction 1 m vertical resolution
2) O_3 by KI oxidation method, 2-3 second time resolution (1 meter altitude)

Surface Measurements - O_3 and meteorological data

Meteorological Data Archive - Radar, Satellite Images, Surface Observations, Upper air data, ETA/RUC model output

Harvard School of Public Health - Petros Koutrakis and George Allen

Mass density of particulates: PM_1, $PM_{2.5}$, PM_{10}, aerosol-size, EC/OC, sulfate, nitrate, toxics

Harvard University - Bill Munger

NOy concentrations and fluxes are used to infer the rates for NOx oxidation and deposition.

University of Maryland - Bruce Doddridge and Bill Ryan

Instrumented Aircraft Cessna 170 and Aztec: GPS, Ozone, Carbon Monoxide, temperature, humidity probe

Ozone and PM event forecasting, description of interesting episodes and meteorological modeling

Drexel University - Steve McDow

Organics in $PM_{2.5}$ with GCMS analysis: non-polar components (alkanes, PAH), acids and diacids using Hi-Vol 24 hour sample

Polar Organics for GCMS with derivatization using PM_{10} with composite samples

Brookhaven National Laboratory - Peter Daum, Larry Kleinman, Yin-Nan Lee, Stephen Springston

DOE G-1 Instrumented Aircraft - particulate and gas-phase chemistry

Brigham Young University - D. Eatough

Measurement of particle volatile mass component and identification of volatile species with RAMS and PCBOSS

Pacific Northwest National Laboratory - C. Doren, J. Allwine, J. Fast, C. Berkowitz

Radiosondes - Pressure, temperature, humidity 0-15 km at Philadelphia, Radar-RASS instrument at West Chester, 12 ozonesondes at Philadelphia

Argonne National Laboratory - R. Coulter, J. Gaffney, N.A. Marley

Radiosondes, SODAR and Chemistry Laboratory at Centerton NJ

N. Carolina A&T State University - D. Dunn

Remote sensing with lidar and SODAR

N. C. State University - H. Hallen

Laser remote sensing, particle optical scattering properties

July 2001 NARSTO-NE-OPS Campaign

Penn State University - Electrical Engineering - Russell Philbrick

1) Raman Lidar - Profiles of Specific Humidity, Temperature, Ozone, Optical Extinction (285, 530 and 607 nm)
2) Radar-RASS - Wind velocity, Virtual Temperature
3) 10 m Tower - Temperature, dew point, relative humidity, wind velocity, wind gust, solar

flux, atmospheric pressure, precipitation
4) Radiosondes - Pressure, temperature, humidity 0-15 km

Penn State University - Meteorology - Bill Ryan and Nelson Seaman
Ozone and PM event forecasting (with Univ. Maryland) and modeling, description of episodes

Millersville University - Richard Clark
Tethered Balloon - 100 m^3 - 10 hr aloft with sensors at surface, 100 m, 200 m, and 300 m AGL
1) Personal Environmental Monitors (PEMS) 4 each - 4 L/min dry PM 10 hr integrated sample
2) Diode laser scatterometer (DustTraks) 1.7 L/min continuous data
3) VOC - Micro-orifice vacuum canister - surface and 300 meters, 10 hour sample GC/MS analysis
Tethered Balloon - 7 m^3 - up/down scan to 300 m each hour
1) Meteorological properties: T, D, RH, wind speed and direction 1 m vertical resolution
2) O_3 by KI oxidation method, 2-3 second time resolution (1 meter altitude)
Surface Gas and Particles - O_3, $NO/NO_2/NO_X$, SO_2, CO, 3λNephelometer
Meteorological Data Archive - Radar, Satellite Images, Observations, Upper air data, ETA/RUC model output

Harvard School of Public Health - Petros Koutrakis, George Allen and Mark Davey
Particle Size and Count: 0.02 to 0.6 :m electrostatic classification, 0.7 to 15 :m time of flight, $PM_{2.5}$ CAMM, Black carbon soot aethalometer, sulfate from HSPH thermal conversion method, EC/OC analyzer
Particulate10-hour Day/Night Samples: HEADS for acid gases [HNO_3, HONO, SO_2], NH_3, and sulfate/nitrate/strong aerosol acidity EC/OC on quartz filters with DRI's TOR analysis, $PM_{2.5}$ and PM_{10} from Harvard impactors with Teflon filters and gravimetric analysis daily, Hivolume OC speciation sampler, HSPH PUF substrate collection; Drexel University filter analysis

Harvard University - College of Engineering - Bill Munger
NOy concentrations and fluxes are used to infer the rates for NOx oxidation and deposition.

University of Maryland - Bruce Doddridge, Russ Dickerson, Lung-Wen (Antony) Chen, Emily Tenenbaum, Aztec aircraft on board instrument rack:
1) Modified Radiance Research Particle_Soot Absorption Photometer
2) Garmin recording GPS_90 Global Positioning System
3) Thermo Environmental Instruments (TEI) Model 49 Ozone
4) Modified TEI Model 43CTL Sulfur Dioxide
5) Modified TEI Model 48 Carbon Monoxide instrument
6) TSI Model 5363 3-wavelength integrating nephelometer

Univ Maryland & NASA Goddard
AERONET (Aerosol Robotic Network) data available include AOT at 1020, 870, 670, 500, 440, 380, and 340 nm plus precipitable Water (cm). Column averaged SS albedo and size number distributions will be calculated from the data.

Drexel University - Prof. Steve McDow, Min Li
1) Organics in $PM_{2.5}$ - GCMS analysis; non-polar components (alkanes, PAH) acids and diacids; Using sample from Tuch TE-1202 Hi-Vol Sampler - 24 hour integration
2) Polar Organics for GCMS with derivatization - Using Anderson PM_{10} with composite weekly samples
3) Metals in Inductively Coupled Plasma Mass Spectrometer (ICPMS); Low volume teflon

membrane filter; Using daily 24 hour sample

Clarkson University - Phil Hopke and Alex Polissar
1) $PM_{2.5}$ with 0.5 hr resolution using RAMS, TEOM and 3OC
2) $PM_{2.5}$ with 1hr resolution using CAMM's instrument
3) Nephelometers- one with and one without dryer

EPA - RTP & **Texas Tech University** - Bill McClenny (EPA), Sandy Dasgupta, Jianzhong Li, Rida Al-Horr (Texas Tech)
1) Fluorescence Detector H2O2 HCHO MHP NH3 with 10 min resolution
2) Ion Chromatography (15 min time resolution) Sulfur Dioxide, Nitric Acid, Nitrous Acid, HCl, Oxalic Acid, Oxalate, Nitrate, Nitrite, Sulfate, Chloride, Ammonium

Brookhaven National Lab
Investigators: Larry Klineman, Linda Nunnemacker, Xiao-Ying Yu,
Yin-Nan Lee, Stephen Springston
1) IC measurements of cations: Na+, K+, NH4+, Ca2+
2) IC measurements of anions:SO42-, NO3-, Cl-, NO2-, oxalate
IC measurements of TOC in solutions with time resolution of 6 min
3) 3-channel Nox (1 min average)
NO continuous 10 ppt DL
NOx continuous 20-30 ppt DL
NOy/NOy* (switching each minute) ~75 PPT DL
4) Carbon Monoxide - non dispersive infra-red (30 sec response) ~50 ppb DL (1-5 min avg)
5) Ozone - ultraviolet absorption (10 sec response)~ 5 ppb DL (1-5 min avg)
6) Sulfur Dioxide - Pulsed fluorescence (30 to 60 sec response time) ~ 30-50 ppt (1-5 min avg)

Carnegie Mellon University - Spyros Pandis
TSI-SMPS 0.02 to 0.6 um, electrostatic classification, run dry

Philadelphia Air Management Services - Fred Hauptman, Lori Condon (AMS)
Speciation Air Sampling System - $PM_{2.5}$ mass, trace metals, organic and elemental carbon, sulfate, nitrate, and other ions/elements

EPA-RTP (NERL-Atmospheric Chemistry and Physics Branch)
Investigators: Edward Edney, Ron Speer, Walt Weathers (EPA); Tad Kleindienst,
Shawn Conver, Eric Corse (ManTech Environmental Technology, Inc.)
1) Integrated EC/OC sample: Triple quartz filters, Thermo-Optical Technique.
2) Liquid Water Content of $PM_{2.5}$, Inorganic Anions, Diacids: Teflon filter collection; liquid water analyzer, IC analysis.
3) IR analysis of $PM_{2.5}$: Low pressure impactor-Reflectance FTIR (size cut points 4, 2, 1, 0.5, 0.25, 0.13, 0.063 :m)
4) Detailed Organic Analysis (1): Extractable organic denuder (Aromatic and natural hydrocarbon oxidation products and other polar compounds)
5) Detailed Organic Analysis (2): Carbon-based organic denuder

June-August 2002 NE-OPS-DEP Campaign

Penn State University - Electrical Engineering - Russell Philbrick
Penn State University - Meteorology - Bill Ryan
Millersville University - Richard Clark
Drexel University - Steve McDow
Clarkson University - Phil Hopke

Trace Gases:

1. Vertical profiles of ozone and water vapor using PSU Raman Lidar
2. Suite of API analyzers and on-site calibrators to measure CO, O_3, SO_2, and $NO/NO_2/NO_X$ by Millersville University
3. Aloft ozone concentration profiles using Millersville University's tethered atmospheric sounding system (TASS) between surface and 300 m
4. Air toxics and minor species composition of particulate matter using GC/MS laboratory analysis of filters gathered at the site and measured at laboratories of Drexel University

Particulates:

1. PSU Raman Lidar vertical profiles of optical extinction at visible and ultraviolet wavelengths
2. Millersville University tethered balloon profiles of the PM using laser diode particle nephelometers and impaction sampling on Personal Environmental Monitors (PEMs, SKC Inc.)
3. Clarkson University particulate properties using CAMMS, RAMS, Sunset Labs OC/EC, HSPH SO_4, aethalometer, and nephalometer
4. Millersville University nephelometer (TSI model 3563) total scatter and backscatter at three wavelengths
5. Particle filter samples analyzed at Drexel University using laboratory techniques for toxics and minor constituents

Meteorological Variables:

1. PSU Radar/RASS vertical profiles of wind velocity (surface to 4.5 km) and virtual temperature (surface to 2.5 km)
2. PSU Raman Lidar vertical profiles of water vapor and temperature
3. Meteorological variables (T, p, mixing ratio, wind speed and direction) as a function of height between the surface and 300 m using Millersville University's tethered sonde
4. Continuous measurements of meteorological variables recored from 10-meter tower

Real-time Regional and Synoptic Data Archive:

U.S. upper air data; U.S. surface data; Meso-eta and RUC model data; Visible and IR satellite imagery; Base reflectivity and velocity radar imagery.

Vita

Sachin Verghese was born on January 18, 1980 in Kottayam, India. He received his B.S. degree in Electronics and Communication from the Madras University (Sathyabama Engineering College) in 2001. He obtained his M.S. degree in Electrical Engineering from the Pennsylvania State University in 2003, and immediately enrolled in the Ph.D. program in Electrical Engineering at the Pennsylvania State University under Dr. C.R. Philbrick. He is currently located in Canonsburg, PA and woks for Ansys, Inc.